Signal Processing Techniques for Spaceflight Magnetometry: Advanced Algorithms for Boomless Magnetic Field Measurements

by

Alex Paul Hoffmann

A dissertation submitted in partial fulfillment
of the requirements for the degree of
Doctor of Philosophy
(Climate and Space Sciences and Engineering)
in the University of Michigan
2024

Doctoral Committee:

Professor Mark B. Moldwin, Chair
Associate Professor Laura Balzano
Professor Michael Liemohn
Dr. Eftyhia Zesta, NASA Goddard Space Flight Center

Alex Paul Hoffmann
aphoff@umich.edu
ORCID iD: 0000-0003-2477-2761

© Alex Paul Hoffmann 2024

DEDICATION

To my grandfather, Maynard “Rocky” Hoffmann, who bravely served at Pearl Harbor and across the Pacific. Your selfless sacrifice and courage, risking everything in the face of harrowing adversity, laid the foundation for your family to live peaceful and prosperous lives. This work is a tribute to your enduring spirit and the legacy of resilience you have instilled in us.

ACKNOWLEDGMENTS

First and foremost, I extend my gratitude to my advisor, Mark Moldwin, for his guidance, incredibly prompt feedback, and encouragement throughout this journey. His expertise and mentorship have been pivotal in shaping this work, my academic development, and my scientific outlook. Thank you as well to my former advisor, David Miles, for introducing me to magnetometers, mentoring me, and encouraging me to do a Ph.D. at the University of Michigan with Mark.

My gratitude also extends to Erik Steinmetz and Mark Engebretson for their support and the unique opportunity they provided me to travel to the Arctic and work on the MACCS ground magnetometers. This experience has been invaluable in broadening my practical understanding and application of our research. Thank you to Brett McCuen for guiding me on my first trip to Baffin Island and training me for future expeditions. Also, thank you to Mike Thode for travelling to Naujaat, Nunavut with me and braving the rain, cold, and 80 kph winds as we trenched outside.

I am thankful to Mark Kushner and Julia Falkovitch-Khain for their support through the Michigan Institute for Plasma Science and Engineering (MIPSE) fellowship, which provided essential funding for my computing resources. The opportunity to interview visiting scientists for the *Plasma in Our Lives* video series under MIPSE was also a valuable experience for me to learn about the diversity of plasma physics research.

I owe a debt of gratitude to Lauro Ojeda for providing the PNI RM3100 error estimates and to Yining Shi for the Swarm perturbation data for my research. Brady Strabel's contribution in developing the software for the PNI RM3100s and his work on the Quad-Mag were critical to the success of this work. Additionally, thank you to Srinagesh Sharma for creating the mock CubeSat used in Chapters 2 and 3 of this work.

I am profoundly grateful to my collaborators on the MAGPRIME project: Imajo Shun, Arie Sheinker, and Matt Finley. Their exceptional contributions have been a cornerstone of this work. The depth of their insights and the spirit of collaboration they brought to our endeavors have been absolutely indispensable.

I would also like to acknowledge the unique contribution of my cousin, Alaina Hoffmann. Her pledge of $200 in support, conditional on the inclusion of the word "Sasquatch" in my dissertation, provided a lighthearted motivation for me to complete this work.

This work was generously supported by a range of NASA projects, including grants 80NSSC18K1240, 80NSSC19K0608, and 80NSSC22M0104. Additional funding was provided

through the NASA HERMES/NEMISIS grant (80GSFC20C0075), the NASA GDC/NEMISIS grant (80GSFC23CA042), and a NASA FINESST Fellowship (80NSSC23K1619). The resources and services offered by the University of Michigan's Advanced Research Computing were invaluable for the computational aspects of this research, playing a crucial role in Chapter 5.

Lastly, I would like to acknowledge the role of my family, friends, and peers for their support, patience, and enthusiasm as I ventured on this challenging journey. Most of all, I am deeply indebted and profoundly grateful to my wife, Arisa Hoffmann, for her unwavering support. Her decision to move across the globe and embark on this journey with me has been a testament to her incredible love and strength. This dissertation is not only a reflection of my efforts but a mosaic of the contributions, support, and belief of all the aforementioned individuals and institutions.

TABLE OF CONTENTS

LIST OF FIGURES

FIGURE

LIST OF TABLES

TABLE

ABSTRACT

This dissertation details advancements in spaceborne magnetometry through the introduction of computational algorithms that effectively mitigate spacecraft-generated magnetic interference in magnetometer data. The first contribution of this work is the Underdetermined Blind Source Separation (UBSS) algorithm. This method uses density-based cluster analysis and compressive sensing to identify and separate stray magnetic noise from ambient magnetic field measurements. Traditionally, long mechanical booms are used to distance the magnetometers away from the spacecraft and perform gradiometry. UBSS marks a significant shift from this methodology by enabling the use of lower quality magnetometers with significantly shorter booms, or no boom at all, to achieve high fidelity magnetic field measurements and thereby reduce mission cost and complexity. Notably, UBSS has been selected to be used with the magnetometer payloads of the NASA Lunar Gateway and the Geospace Dynamics Constellation. Building upon the foundation laid by UBSS, the dissertation introduces an integrated noise removal suite that combines the UBSS algorithm with the Quad-Mag CubeSat magnetometer. This integration enables high-fidelity magnetic field measurements on CubeSats without the need for deployable booms. The Quad-Mag with UBSS system broadens the possibilities for magnetometer inclusion in various space missions by reducing size, weight, power, and cost constraints. Another major contribution of this work is the Wavelet-Adaptive Interference Cancellation for Underdetermined Platforms (WAIC-UP) algorithm. Tailored for compact and resource-constrained spacecraft like CubeSats, WAIC-UP employs wavelet analysis to offer a highly efficient solution for magnetic interference removal. This algorithm enables robust magnetic field measurements in space with minimal computational resources, making it an ideal choice for small, resource-limited spacecraft. The low-computational complexity enables potential onboard interference removal for applications such as spacecraft attitude determination. The dissertation culminates in the introduction of the MAGnetic signal PRocessing, Interference Mitigation, and Enhancement (MAGPRIME) library. As an open-source Python library, MAGPRIME integrates a comprehensive suite of advanced noise removal algorithms. It aims to standardize methodologies in magnetic noise removal and stimulate further research. This contribution significantly impacts the space science community by offering novel, efficient, and practical solutions to overcome challenges in spaceborne magnetometry. Collectively, these advancements enable high-fidelity magnetic field measurements on small, low-cost spacecraft, thereby revolu-

tionizing design paradigms and facilitating large constellations for space physics research.

CHAPTER 1

Introduction

1.1 Motivation and Overview

Magnetometers are instruments used to measure the strength and direction of magnetic fields. Magnetometers play a large role in exploration of the geospace environment and the greater heliosphere, however, their operation is not without challenges. A significant hurdle to spacecraft magnetometry is stray magnetic fields generated by spacecraft subsystems, which interfere with the natural magnetic field signals of interest. The central focus of this dissertation is to develop innovative noise removal algorithms to isolate and eliminate spacecraft-generated noise from the magnetic field measurements germane to space science and spacecraft operations. By addressing this issue, we aim to significantly reduce the design complexity of spacecraft and relax the stringent requirements on magnetometers, thereby enabling the deployment of larger constellations of spacecraft. This work seeks to bolster the capabilities of spacecraft magnetometry, improve the accuracy of their measurements, foster a greater capacity for scientific discovery, and remove the barriers to their operation.

In this chapter, we examine the operational principles of magnetometers, their evolution, and applications in space missions. This detailed discussion lays the groundwork for addressing the challenge posed by magnetic field interference, a significant obstacle in accurate space magnetometry. Additionally, we present the fundamental principles of Compressive Sensing, a key methodology for separating stray magnetic fields. Subsequently, we conduct a critical evaluation of the various sources of uncertainty in magnetometer measurements, thereby underlining the importance

of precision in space-based data collection. This background, which combines technological and methodological details, provides the basis and motivation for the description of the complexities of spaceborne magnetometry investigated in this thesis.

1.2 Introduction to Magnetometers

The magnetometer is a device for measuring electromagnetism, one of the four known fundamental forces pervading the universe. With roots tracing back to the 11th century or earlier, the simplest form of a magnetometer—known as a compass—has been an essential tool for global navigation (Holzman, 1958). The magnetometer took a significant leap in 1833 when the German physicist Johann Carl Friedrich Gauss invented the first absolute magnetometer. His work, titled "*Intensitas Vis Magneticae Terrestris ad Mensuram Absolutam Revocata*," introduced a method that precisely isolated magnetic field magnitude by timing the rotation of a suspended magnetic needle with a known moment of inertia (Gauss, 1833). Innovation in magnetometry continued into the 20th century with the eventual invention of the fluxgate magnetometer by Aschenbrenner and Goubau (1936). This particular device proved ideal for navigation and reconnaissance, leading to substantial development during World War II and the Cold War (Ripka, 1992). As a result of the ubiquity of electromagnetism across different scales and domains, there are many ways to measure magnetic fields. This has resulted in a large variety of magnetometers that have qualities uniquely suited to different use-cases. Some common modern implementations include the search coil, flux-gate, hall effect, and magneto-inductive magnetometers.

1.2.1 The Search Coil Magnetometer

The search coil magnetometer is composed of a tightly wound coil of conductive wire. The search coil measures the AC magnetic field up to very high frequencies, so it is often included as a component of instrument payloads that measure higher frequency electromagnetic waves in space. The search coil measures changing magnetic fields through Faraday's law.

$$\nabla \times \mathbf{E} = -\frac{\partial \mathbf{B}}{\partial t} \tag{1.1}$$

Due to the coil-structure of the search coil, any changes in the magnetic field induce a current that can be measured and integrated to retrieve the magnetic field. The passive sensing mechanism of the search coil magnetometer allows it to sense very high frequency signals in the kHz Range. It is important to note that the gain of a search coil is frequency-dependent, making it unsuitable for measuring constant or slowly varying fields. Typically, search coils are paired with electric field antennae to measure high frequency electromagnetic waves. They have become standard tools on several spacecraft such as the Parker Solar Probe (PSP), Magnetospheric Multiscale (MMS) mission, and Time History of Events and Macroscale Interactions during Substorms (THEMIS) mission (Bowen et al., 2020; Le Contel et al., 2016; Roux et al., 2008). Figure 1.1 shows an example schematic of a single-axis search coil magnetometer.

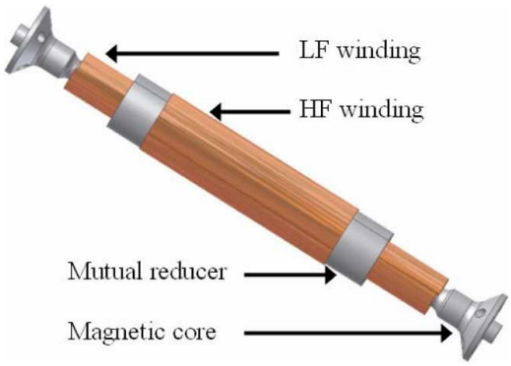

Figure 1.1: A schematic of a dual-band search coil magnetometer, designed and illustrated by Coillot et al. (2010). The instrument has two coils that target different frequency bands. This search coil was designed for the Plasma Wave Instrument on the BepiColombo mission to Mercury.

1.2.2 The Fluxgate Magnetometer

The fluxgate magnetometer outperforms the search coil magnetometer in accurately measuring DC magnetic fields. It is composed of a driving coil, a magnetically permeable core, and a sensing coil. The driving coil carries an alternating current that makes the core switch between two states:

saturated and unsaturated. Saturation indicates the alignment of all magnetic domains within the material of the core. When the core is near zero magnetization, a voltage is induced in the sensing coil with a frequency that is twice as high as the driving current frequency, or the second harmonic. This voltage driven at the second harmonic signal is proportional to the external field magnitude. Figure 1.2 shows a schematic diagram of the fluxgate magnetometer with its main components.

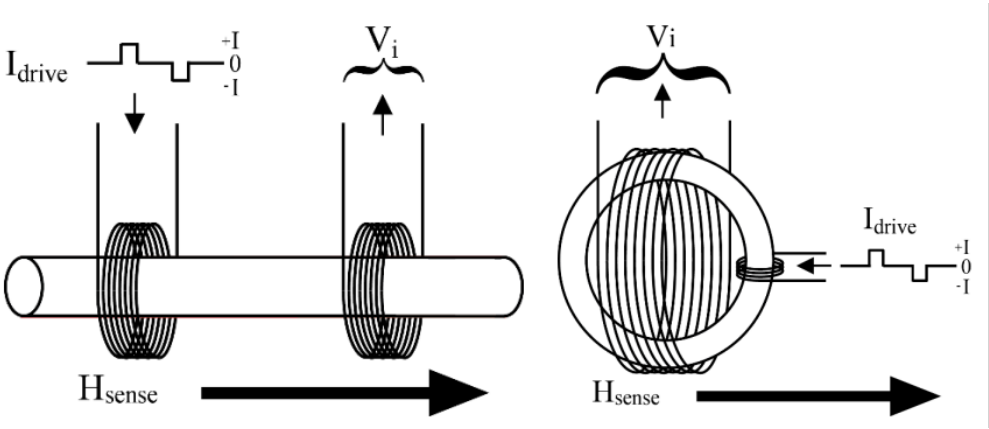

Figure 1.2: A schematic of the drive coil, permeable core, and sense coil of a fluxgate magnetometer, as presented by Miles (2017). The schematic on the left shows a design using a rod-core while the schematic on the right uses a ring-core.

Fluxgate magnetometers have been chosen for most spacecraft missions due to their fine resolution and reliability (Smith et al., 1998; Auster et al., 2008; Wallis et al., 2015; Du et al., 2020). However, these magnetometers rely on a highly permeable core material to achieve low noise levels. The commercial production of low-noise cores ceased in the early 2000s, resulting in high-quality fluxgate cores becoming a rapidly dwindling commodity. However, new research and production capabilities have been revived in the US recently (Miles et al., 2022). Almost all spacecraft that have been launched with magnetometer payloads for scientific exploration use a fluxgate magnetometer. Figure 1.3 shows an example of a fluxgate magnetometer in its fully assembled form.

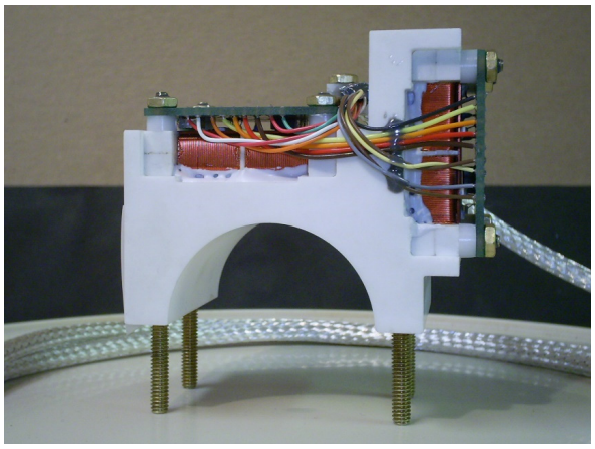

Figure 1.3: A dual-axis fluxgate magnetometer constructed of two pairs of orthogonal ring cores, sense windings, and drive windings, as detailed by Miles (2017).

1.2.3 The Hall-effect Magnetometer

The Hall effect magnetometer, like the search coil and fluxgate counterparts, measures both the magnitude and direction of a magnetic field. It employs the Hall effect, a phenomenon where a voltage difference materializes across an electrical conductor subjected to both an electric current and a magnetic field at right angles. The voltage difference, known as the Hall voltage, directly relates to the product of the current, magnetic field, and a property-dependent constant in the system called the Hall coefficient (Crescentini et al., 2022).

Hall effect magnetometers function by channeling a steady current through a thin, flat semiconductor, often referred to as the Hall sensor or Hall probe. When exposed to a magnetic field, a Hall voltage develops across this sensor and can subsequently be measured. This measurement of voltage fundamentally allows us to compute both the strength and direction of the magnetic field based on the formula:

$$V_H = R_H \frac{IB \sin\theta}{t} \tag{1.2}$$

In the equation above, V_H represents the Hall voltage, R_H symbolizes the Hall coefficient, I is the electric current, B outlines the magnetic field, θ is the angle separating the magnetic field and the current, and t is the Hall sensor's thickness.

Hall effect sensors are tiny and inexpensive devices that can detect magnetic fields in compact, embedded systems like smartphones due to their straightforward operation (Cai et al., 2012). However, they typically lack the high-resolution measurements characteristic of magnetometers such as fluxgate magnetometers.

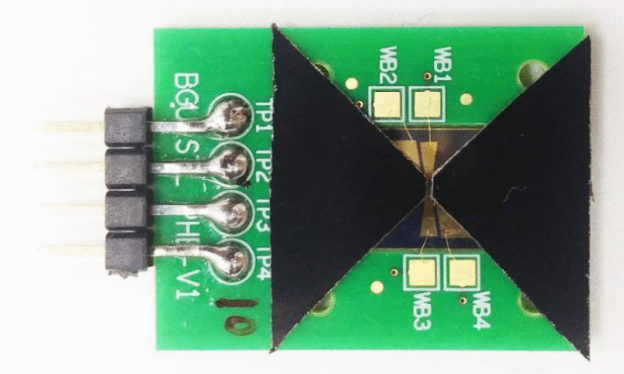

Figure 1.4: A low-noise Hall-effect magnetometer, as designed and illustrated by Nhalil et al. (2019).

1.2.4 The Magneto-Inductive Magnetometer

The Magneto-inductive magnetometer, an inherently digital instrument, measures the vector magnetic field by employing a relaxation circuit. This sensor design consists of a Schmitt trigger, and a resistor-inductor pair that repeatedly drives the Schmitt trigger into saturation. Figure 1.5 shows a schematic of the digital relaxation oscillator.

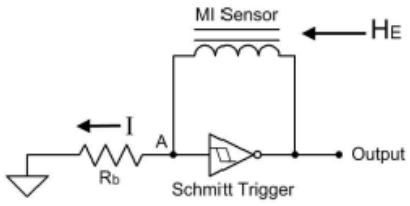

Figure 1.5: A Schmitt trigger-based RL oscillator (Figure from Leuzinger and Taylor (2010)).

The sensing capability of the magnetometer lies in the characteristic time-constant of the resistor-inductor (RL) pair, which establishes the time-to-saturation for the circuit. An external

magnetic field's presence can bias the inductor and consequently modify the time-to-saturation constant. By repeatedly driving the circuit into saturation in one direction, a clock signal is generated. When the polarity is reversed, a clock signal with a different frequency is generated due to the change in time-constant of the RL circuit. The difference of these frequencies can be used to derive the magnetic field strength (Regoli et al., 2018b).

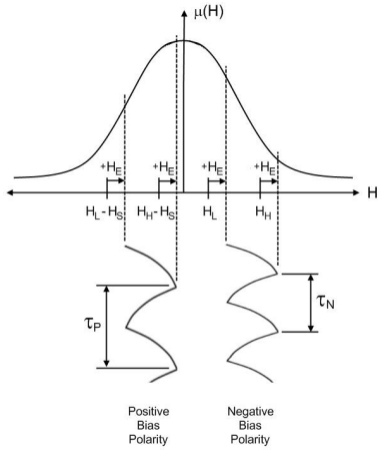

Figure 1.6: The oscillations of the current in the solenoid and the period for positive and negative bias polarity (bottom), while the coils' induction is presented based on the applied magnetic field (top) (Figure from Leuzinger and Taylor (2010)).

In comparison to other vector magnetometers like fluxgate and search coil types, magneto-inductive magnetometers confer several advantages. With their small size, straightforward implementation, and digital nature, they are particularly suited to compact satellite platforms like CubeSats, where size, weight, and power stand as constraints (Strabel et al., 2022). Figure 1.7 shows a depiction of a magneto-inductive magnetometer

Search coils, fluxgates, Hall effect, and magneto-inductive sensors are common magnetometers in spacecraft applications. Each type has unique advantages and disadvantages, which may make them more or less suitable for certain uses. However, many other magnetometers may not be compatible with spacecraft designs due to their size, weight, and power requirements. Nevertheless, the magnetometers discussed earlier are crucial for space exploration and research. In Table 1.1, different types of magnetometers including search coils, fluxgates, Hall effect, and magneto-inductive

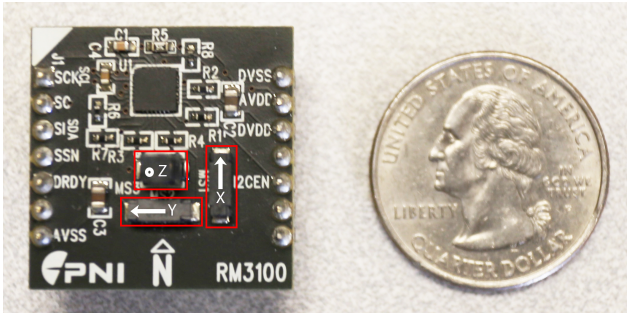

Figure 1.7: A PNI RM3100 magneto-inductive magnetometer shown next to a coin for scale comparison. The inductive coils are outlined in red (Figure from Regoli et al. (2018b)).

magnetometers are compared based on sensitivity, mass, power, and notable characteristics.

Sensor type	Sensitivity (pT / $\sqrt{(Hz)}$)	Mass (kg)	Power (mW)	Notes
Search coil	10^{-1}	10^{-1}	10^{2}	High bandwidth and low sensitivity, suitable for measuring AC fields (Le Contel et al., 2016).
Fluxgate	10^{1}	10^{-1}	10^{2}	Measures DC fields with high accuracy. Widely used in space missions due to reliability (Bowen et al., 2020).
Hall effect	10^{0}	10^{-3}	10^{0}	Very small size and weight, easy to integrate with other circuits (Nhalil et al., 2019).
Magneto-inductive	10^{0}	10^{-3}	10^{0}	Digital output, robust to temperature variations (Regoli et al., 2018b).
Overhauser	10^{-2}	10^{0}	10^{3}	High absolute accuracy with good thermal stability (Acuña, 2002).
Optically Pumped	10^{-3}	10^{0}	10^{3}	High absolute accuracy, suitable for long-duration missions (Merayo et al., 2008; Kominis et al., 2003).

Table 1.1: Comparison of Magnetometer Types Based on Key Performance Metrics. Each row gives an order of magnitude estimation of the sensors characteristics based on the instruments referenced in the notes column and a review paper by Lenz (1990).

1.3 Magnetism in Space

The Sun, the central entity in our solar system, constantly emits a stream of solar wind that stretches its dynamo-generated magnetic field well beyond the planetary orbits. This magnetic field is dragged out by the solar wind and forms the interplanetary magnetic field (IMF), which has a spiral shape, called the Parker Spiral (Parker, 1958). When this solar wind interacts with interstellar plasma, it forms a vast region called the heliosphere where solar wind properties predominantly dictate the flow of mass, energy, and momentum in space. Similarly, the dynamo-generated magnetic field of Earth interacts with the solar wind and forms the Earth's magnetosphere (Eastwood et al., 2015). The solar wind compresses the magnetosphere on the dayside and elongates it into a structure known as the magnetotail on the nightside through magnetic reconnection. Figure 1.8 provides an illustrative diagram of this solar wind-magnetosphere interaction.

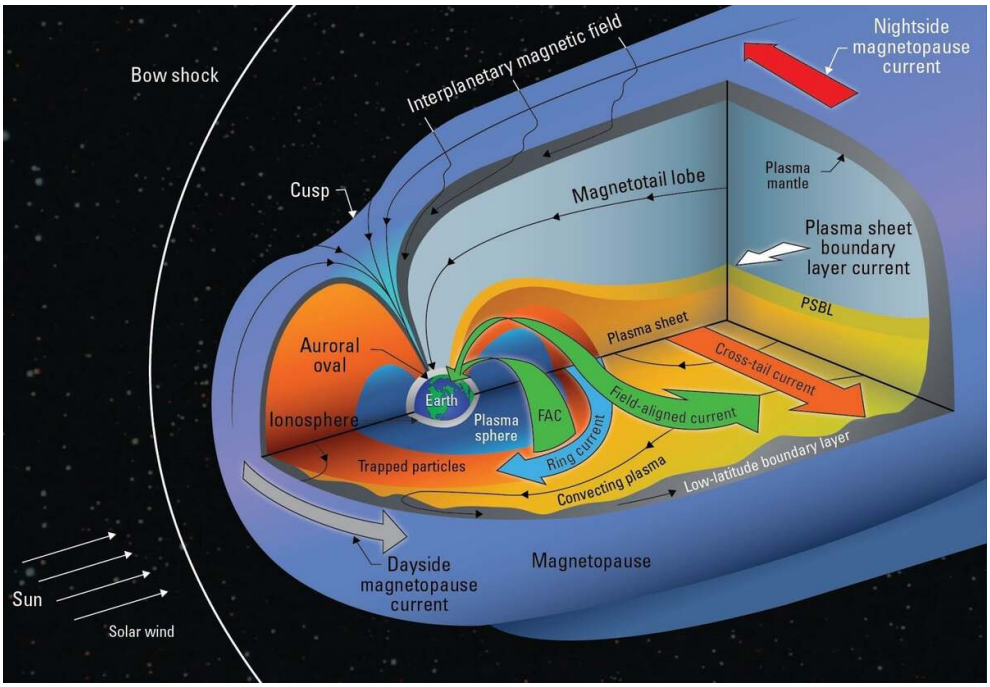

Figure 1.8: Diagram of Earth's magnetosphere influenced by solar wind (Figure by Kivelson and Russell (1995)).

Figure 1.8 shows the various current systems of the magnetosphere that are driven by the solar wind-magnetosphere interaction. The magnetopause current is a thin sheet of electric current that

flows along the boundary between the magnetosphere and the magnetosheath-shocked solar wind, separating the two magnetic domains (Ganushkina et al., 2018). The field-aligned currents are currents that flow along the magnetic field lines connecting the magnetosphere and the ionosphere, carrying energy and momentum between them. The ring current is a toroidal current that encircles Earth in the equatorial plane, consisting of energetic charged particles trapped by Earth's magnetic field. The cross-tail current is a current that flows across the magnetotail, from dawn to dusk, and is associated with magnetic reconnection in the tail. The plasma sheet boundary layer currents are currents that flow along the edges of the plasma sheet, which is a region of hot and dense plasma in the magnetotail. These currents are important for shaping the structure and dynamics of the magnetosphere and influencing the space weather effects on Earth.

The Sun is a highly dynamic system with a significant influence on Earth's near-space environment, also known as the "geospace" environment. Solar phenomena, including Coronal Mass Ejections (CMEs) and Stream Interaction Regions (SIRs), alter the solar wind's properties. As a result, they cause substantial perturbations in the geospace environment from the bowshock to the magnetotail and contribute to the complex phenomena of space weather (Guarnieri et al., 2006; Pulkkinen, 2007; Richardson, 2018; Burlaga et al., 1982).

The orientation of the IMF embedded in the solar wind with respect to Earth's magnetic field plays a key role in determining the degree of coupling between the solar wind and the magnetosphere. A southward IMF Bz component enables more efficient magnetic reconnection at the dayside magnetopause (Anderson et al., 2014; Milan et al., 2007; Gosling et al., 2005). This increases the rate at which solar wind energy is transferred into the magnetosphere. The resulting disturbances propagate to the high latitude ionosphere, enhancing auroral electrojets and Joule heating of the upper atmosphere (Wang et al., 2008; Gonzalez et al., 1989). This leads to the creation of ionospheric density structures that can disrupt radio propagation and global communications (Zou et al., 2021; Lanzerotti, 2001; Moldwin, 2022).

Space weather events can profoundly impact human civilization by disrupting electrical and communication systems. The Earth's geomagnetic field is in a constant state of flux due to dynamic

interactions with the solar wind and IMF. Rapid variations in the geomagnetic field induce voltages along extended conductive structures such as power lines and pipelines (Parry, 2022). This can generate large geomagnetically-induced currents (GICs) that overload and damage transformers and other components of the power grid, resulting in widespread blackouts (Pulkkinen et al., 2012).

Continuous monitoring of conditions in space and their impacts on Earth's geomagnetic field is critical for space weather awareness and national security. Figure 1.9 illustrates how dynamics in the Sun-Earth system can affect geospace and terrestrial infrastructure. Solar flares, coronal mass ejections, solar energetic particles, and fluctuations in the solar wind and IMF can all trigger geomagnetic storms, radiation belt enhancements, ionospheric disturbances, and other space weather effects that disrupt radio communications, degrade satellite operations, induce currents in power grids, and endanger astronauts (Moldwin, 2022).

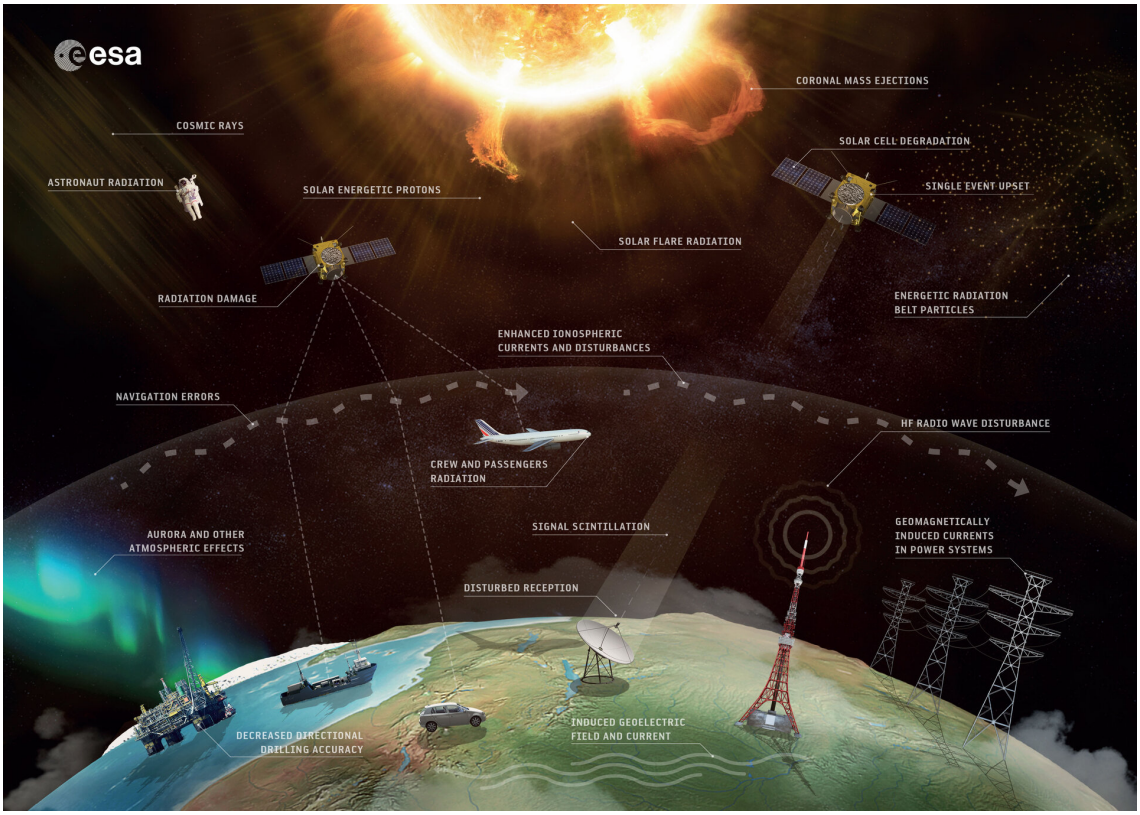

Figure 1.9: Overview of space weather effects spanning from the Sun to human society by the European Space Agency - CC BY-SA 3.0 IGO.

A constellation of spacecraft comprising the Heliophysics System Observatory (HSO) make

measurements throughout the heliosphere, magnetosphere and ionosphere. One recent spacecraft in the observatory, the Parker Solar Probe, launched in 2018, is designed to probe the mechanisms behind the heating of solar wind within the solar corona (Kasper et al., 2021). The solar corona is the Sun's outermost layer, which has a temperature of a million degrees Kelvin, much higher than the surface of the Sun. The reason for this high temperature is still not completely resolved, and the Parker Solar Probe aims to definitively solve it by getting closer to the Sun than any other spacecraft before (Chandran et al., 2010). Remarkably, this probe is humanity's fastest-created object, traveling at speeds of approximately 400,000 mph—around 3.5 times faster than the previous record holder, a manhole cover used in a subterranean nuclear test (Nuclear Weapon Archive, 2003). Figure 1.10 displays the spacecraft within the Heliophysics System Observatory.

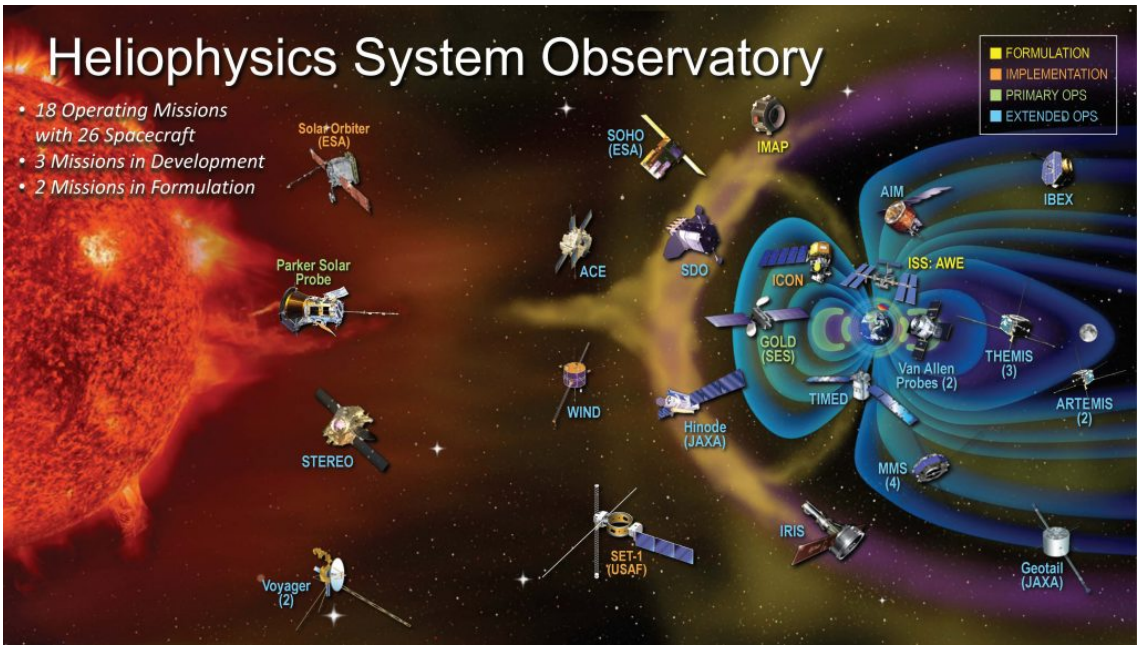

Figure 1.10: The Heliophysics System Observatory (HSO) is an international fleet of spacecraft that observe the Sun, solar wind, and their effects on Earth's magnetosphere and ionosphere. The observatory, depicted by NASA, aims to understand fundamental solar and space physics processes from the Sun to Earth.

Several spacecraft within the Heliophysics System Observatory are strategically positioned to monitor the solar wind and its evolution through the heliosphere. The Advanced Composition Explorer (ACE) and Wind spacecraft, for example, orbit the Sun-Earth L1 Lagrange point directly

upstream from Earth (Smith et al., 1998). Measurements from these L1 monitors are critical for constraining solar wind conditions before they impact our planet.

Other missions explore distinct regions of the geospace environment. The THEMIS mission, composed of five spacecraft, investigates the causes and effects of geomagnetic substorms (Angelopoulos, 2009). Two of the THEMIS spacecraft were split off from the constellation to form the ARTEMIS mission. The two ARTEMIS spacecraft orbit the moon to study its environment and interaction with the magnetotail (Angelopoulos, 2014). Meanwhile, in the magnetotail, the GEOTAIL spacecraft was a joint collaboration between the U.S. and Japan to study the structure and dynamics of the turbulent magnetotail that ended in 2022 (Nishida, 1994). These multi-point observations enable a more complete understanding of energy transfer and plasma transport throughout the interconnected Sun-Earth system.

Out of the nineteen active or extended missions within the HSO, only nine carry magnetometers. Although magnetometers are straightforward and precise instruments, integrating magnetometers on spacecraft can be challenging (Acuña, 2002). Stray magnetic fields from electrical subsystems like reaction wheels and solar panels can easily contaminate ambient field measurements (Hoffmann and Moldwin, 2022). To mitigate this, magnetometers are often placed on long booms extending far from the spacecraft body (Ness et al., 1971). This effective but complex and costly solution limits the number of missions that ultimately host magnetometers. As a result, many space missions do not include magnetometers due to their specific science objectives, budget, or design constraints. Developing techniques to operate these sensitive instruments within the spacecraft body could enable more widespread adoption. Moreover, the application of algorithms to remove spacecraft noise allows the dual use of magnetometers designed for attitude determination systems to provide valuable in situ magnetic field measurements for heliophysics research.

1.4 Spaceborne Magnetometry

1.4.1 Magnetometer Evolution: From Sputnik 3 to the Europa Clipper

The first spacecraft magnetometer was launched on the Sputnik 3 spacecraft by the Soviet Union in 1958. Sputnik 3 was significantly larger than its predecessors and carried a suite of scientific instruments including a mass spectrometer, manometer (to measure pressure), Geiger counter, piezoelectric meteorite counter, field mill electrometer, and fluxgate magnetometer (Dolginov et al., 1961). The fluxgate magnetometer was mounted on a servo on the main body of the spacecraft, away from other power systems in an attempt to isolate it from interference. However, testing on the ground revealed significant magnetic interference from other onboard systems, with deviations up to 3500 nT observed (Dolginov et al., 1961). This level of noise highlighted the need to mount magnetometers on booms to minimize the impact of spacecraft-generated magnetic fields. The Sputnik 3 magnetometer was used to study magnetosphere-ionosphere interactions, investigate the structure of the Earth's magnetic field, and for attitude control.

The challenge of obtaining accurate magnetometer measurements in space missions persisted through several historical missions, including Pioneer 1, Explorer VI, and Pioneer 5. Each of these missions utilized spin-stabilized spacecraft and employed a bus-mounted search coil magnetometer. The magnetic field measurements were derived by utilizing the spacecraft's spin and the rate of change of the magnetic field (dB/dt) detected by the search coil. These magnetometers were enclosed in aluminum shells to shield them from radio frequency (RF) interference, with a noise threshold of 0.1 nT (Judge et al., 1960). Pioneer 5, in particular, played a pivotal role in verifying the collisionless nature of magnetoacoustic waves within the interplanetary magnetic field (Coleman Jr. et al., 1960). Meanwhile, both the Explorer VI and Pioneer 5 missions contributed to the understanding of the ring current (Smith et al., 1960). Later, in 1962, the Mariner 2 spacecraft took a significant step forward by incorporating a three-axis magnetometer (Coleman Jr., 1966). However, this magnetometer was mounted on a tower extending from the spacecraft, which posed challenges in maintaining a magnetically clean environment. Mariner 2 embarked on a mission

to Venus, where it collected crucial data on Venus' induced magnetosphere and contributed to characterizing the behavior of the ambient solar wind and IMF (Smith et al., 1965).

A noteworthy milestone in the development of magnetometers in space exploration occurred with the launch of the Explorer X spacecraft in 1961. This spacecraft featured a magnetometer mounted on the end of a mechanical boom, marking a departure from previous bus-mounted designs. The Explorer X was equipped with two monoaxial fluxgates on 31-inch-long booms (Heppner et al., 1963). This innovation allowed for the measurement of the ring current and sudden storm commencements with greater precision. By 1961, it had become evident that magnetometers needed to be positioned on mechanical booms to prevent interference from stray magnetic fields (Dolginov et al., 1961).

As space exploration advanced, booms grew both in size and complexity. In 1977, the Voyager spacecraft were launched, featuring two fluxgate magnetometers on 13-meter-long booms (Behannon et al., 1977). Additionally, magnetic gradiometry was introduced to calculate and subtract stray magnetic fields generated by the spacecraft. The fundamental concept of magnetic gradiometry involves modeling the spacecraft's magnetic field as a dipole, a method that works effectively with a sufficiently long boom due to the rapid decrease in higher-order magnetic field components with distance (Ness et al., 1971).

Fast forward to 2024, and the mechanical boom and magnetic gradiometry remain the standard in space magnetometry. Notable missions like the Europa Clipper are slated to carry three magnetometers placed on an 8.5-meter boom to enable precise gradiometry (Kivelson et al., 2023). This mission aims to investigate the properties of Europa's subsurface oceans by studying the inductive response of the ocean to external magnetic fields. Similarly, the Parker Solar Probe boasts two fluxgate magnetometers and one search coil, strategically placed on a 3.5 m boom behind the spacecraft's heat shield to withstand the extreme conditions of the solar corona (Bowen et al., 2020).

However, a paradigm shift is occurring with the advent of CubeSats. CubeSats are compact, cost-effective spacecraft that consist of 1U, or 1000 cm^3, cubes that can be stacked together into

larger configurations, such as 3U or 6U. Long mechanical booms are impractical for CubeSats due to size and cost constraints, prompting innovative solutions. Miles et al. (2016) introduced a compact fluxgate magnetometer designed to attach to the end of a deployable 60 cm boom, catering to larger CubeSat platforms. While promising, this design has encountered deployment challenges (Miles et al., 2016). Using a different approach, Regoli et al. (2018a) and Strabel et al. (2022) developed a magnetometer that fits inside the CubeSat bus called the Quad-mag. The Quad-mag takes distributed measurements of the spacecraft's magnetic field to facilitate interference removal. While it has not yet been deployed on a spacecraft, this method shows significant potential as a groundbreaking innovation in spaceborne magnetometry, serving as the first interference-removing magnetometer without a boom.

The significant role of CubeSats in spaceborne magnetometers is underscored by several recent prominent CubeSat missions. Investigations by the Scintillation Prediction Observations Research Task (SPORT) CubeSat into equatorial ionosphere scintillations, and the focus of the CubeSat for Ions, Neutrals, Electrons, and Magnetic Fields (CINEMA) on the dynamics of space weather, exemplify the transformative impact of these miniature satellites on our understanding of complex space phenomena (Spann et al., 2017; Archer et al., 2015). Despite facing initial operational challenges, missions like NASA's Dellingr have showcased the resilience and scientific potential of CubeSats, affirming their value for future explorations (Clagett et al., 2017). Additionally, the Electron Losses and Fields Investigation (ELFIN) mission's study on electron loss in the Earth's radiation belts further highlights CubeSats' contribution to advancing space weather prediction and modeling (Angelopoulos et al., 2020). Together, these missions illustrate the pivotal role of CubeSats in the ongoing evolution of spaceborne magnetometry, marking a significant shift in how space research is conducted.

1.4.2 Stray Magnetic Fields and Magnetic Cleanliness

The presence of stray magnetic fields poses a considerable challenge in spacecraft design and operation. These artificial fields are generated by permanent magnets, magnetically permeable ma-

terials, and electrical currents onboard the spacecraft. The characteristics of stray magnetic field noise are highly variable, producing signals ranging from low frequency offsets to time-variable high-frequency interference. Removal of DC magnetic field noise is traditionally done through gradiometry techniques or thorough characterization of the spacecraft's magnetic structure. With spacecraft characterization, the ambient magnetic field can be retrieved through the following relationship:

$$B_{true} = C^{-1}B_m + O \tag{1.3}$$

In this equation, B_m is the raw magnetometer data, C is the orthogonality matrix that corrects for mechanical misalignments and normalizes the gain between magnetometers, and O is a vector that accounts for DC offsets (Russell et al., 2016). However, in cases with AC magnetic field interference, the system is more accurately described in the following system.

$$B_m(t) = B_{true}(t) + Ks(t) \tag{1.4}$$

In this model, the vector $s(t)$ represents all the stray magnetic field signals generated by the spacecraft's electrical systems. These could include interference signals from solar panel currents, reaction wheels, and other science instruments and subsystems. The matrix K describes how each stray field source couples into each magnetometer's measurements (Sheinker and Moldwin, 2016). The elements of K give the gain of each stray field signal observed at each magnetometer. The contents of $s(t)$ and shape of K depend on the specifics of the spacecraft's configuration, and operational modes. With complex, time-varying stray fields and couplings, accurately separating the true ambient field from the interference in the magnetometer data is non-trivial.

All electrical currents onboard a spacecraft produce stray magnetic fields that can interfere with sensitive magnetometers. For example, the GOES-16 weather satellite's arcjet thrusters generate 20 nT of noise with a square wave signature (Califf et al., 2020). Attitude control components also contribute significant magnetic interference. Reaction wheels, used for precise attitude control,

emit high frequency noise that shifts based on wheel speed (Finley et al., 2023). Figure 1.11 shows a spectrogram of reaction wheel noise measured on GOES-16. Additionally, magnetorquers interact with Earth's geomagnetic field to generate torque for attitude control, but ripple currents in their supplies contaminate magnetometer data (Jovanovic et al., 2021). Any large power-drawing science instruments can also create magnetic noise.

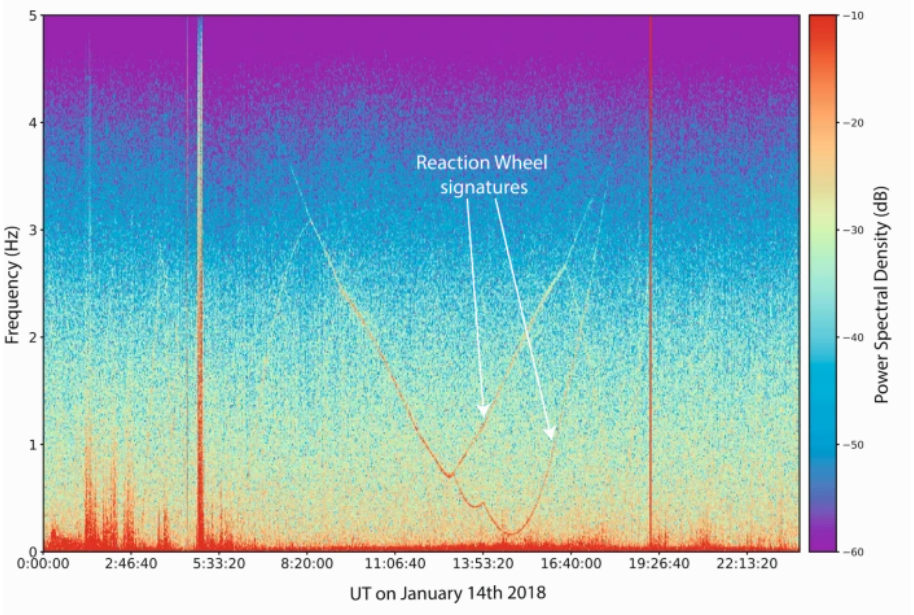

Figure 1.11: Reaction wheel noise measured by the magnetometer on the GOES-16 spacecraft on January 14th, 2018 (Figure by Loto'aniu et al. (2019)).

Interference from low-frequency stray magnetic fields can hinder scientific missions aiming to measure absolute magnetic fields, which are extremely valuable for missions such as the Europa Clipper (Kivelson et al., 2023). Concurrently, high-frequency interference obstructs space science investigations that are focused on variable magnetic field phenomena like magnetoacoustic waves and geomagnetic disturbances (Hartinger et al., 2013). As a result, high-profile space exploration missions place an emphasis on rigid spacecraft magnetic cleanliness standards to mitigate these effects (Russell et al., 2016; Ludlam et al., 2009).

Magnetic cleanliness refers to an exhaustive set of requirements and procedures aimed at diminishing the magnetic footprint of a spacecraft and all of its sub-systems and instruments. An effective magnetic cleanliness program should ensure that the design of the power distribution sys-

tems circumvents the creation of current loops, utilizes shielded-twisted pair wiring, accurately locates and characterizes magnetic sources, and exclusively uses non-ferromagnetic materials. For many missions, the Magnetic cleanliness program also includes a "swing" test after integration that measures the magnetic moment of the fully assembled spacecraft in a ground test environment. The swing test involves hanging the spacecraft from a crane and letting it swing freely while recording the magnetic field data from sensors attached to it. The data can then be used to estimate the direction, location, and magnitude of the spacecraft's magnetic moment (Russell et al., 2016).

The usage of magnetic shielding is a method that is generally not advocated due to its potential drawbacks. Shielding techniques involves enveloping sources of magnetic noise with a highly permeable magnetic material, such as Metglas, which allows magnetic field lines to close through a path of least reluctance instead of through free space (Shepherd and Kress, 2007). This approach can inadvertently introduce additional interference to the spacecraft due to the incorporation of ferromagnetic materials.

Given the complexities and challenges associated with stray magnetic fields and realizing the criteria for magnetic cleanliness, an alternative approach that shows promise is the use of noise removal algorithms. These algorithms establish a systematic approach to identifying and neutralizing the interference effects in the collected magnetometer data, thereby reducing the need for stringent magnetic cleanliness requirements (Sheinker and Moldwin, 2016; Finley et al., 2023; Imajo et al., 2021; Constantinescu et al., 2020; Ness et al., 1971). The adoption of noise removal algorithms potentially mitigates the need for spacecraft booms, which are often used to distance magnetometers from magnetic interference sources. By integrating such algorithms, we can better distinguish between the true environmental magnetic field and interference produced by the spacecraft itself, delivering high-quality space science data. While prevention and mitigation techniques are vital, the mainstay of any successful magnetic cleanliness program is the combination of these with intelligent noise removal algorithms. These algorithms provide additional flexibility in spacecraft design and can help ensure the scientific integrity of space missions, making them an invaluable tool in the process of stray magnetic field mitigation.

1.4.3 Uncertainty Analysis for Spacecraft Magnetic Field Measurements

Achieving high-fidelity magnetic field measurements from a spacecraft requires accounting for various sources of uncertainty and error. The total error budget comprises both random and systematic errors originating from the magnetometer instrument, spacecraft systems, and the measurement process. Quantifying these errors is crucial for assessing data quality and placing bounds on the accuracy of scientific interpretations. For example, the Europa Clipper magnetometer investigation uses fluxgate sensors with a resolution of 8 pT, but has a total error budget of up to 1.5 nT to measure the inductive response of Europa's magnetic shell (Kivelson et al., 2023).

The magnetometer instrument contributes errors from its inherent noise floor and calibration uncertainties. Fluxgate magnetometers typically have a resolution on the order of 1-100 pT, while search coils can measure down to 1 pT (Tumanski, 2007). However, the resolution is also limited by the Least Significant Bit (LSB) of the Analog-to-Digital Converter (ADC) used to digitize the analog signal, which depends on the voltage reference, the number of bits of the ADC, and dynamic range of the local magnetic field (Cerman et al., 2005). Temperature variations and aging of the sensors leads to drifts in gain and offsets over time (Greene et al., 2023). Together, these instrument errors make up a baseline noise level.

Magnetic interference from spacecraft systems also degrades measurement accuracy. As discussed previously, currents in electrical components produce time-varying stray fields that couple into the magnetometer measurements. Thermal cycling of the spacecraft over its orbit leads to temperature-dependent variability in these magnetic noise sources. Pointing jitter and flexibility of booms further modulates the coupling of noise into the sensors. In total, spacecraft-generated interference can reach levels up to thousands of nT without mitigation efforts (Miles et al., 2016).

Additional errors arise from the measurement process itself. Temporal lag between measurements produces phase-delays that effects noise removal algorithms such as gradiometry (Sonett, 1968). Aliasing from undersampling high frequency signals corrupts measurements. Taken together, these measurement errors can accumulate to significant levels.

By budgeting these identified error sources, the total expected accuracy can be quantified. This

facilitates the determination of whether the science requirements will be met. It also helps prioritize the mitigation of major error contributors. Realistic error budgets are critical to the success of magnetic field experiments in space. Thorough pre-flight analysis, in-flight calibration, and post-processing techniques help minimize errors and maximize data quality. With concerted effort across instrumentation, spacecraft systems, and data analysis, sub-nT accuracy can be achieved for space-based magnetometry.

1.5 Compressive Sensing in Space Physics

Compressive Sensing (CS) is a signal processing method that enables the reconstruction of sparse signals sampled below the Nyquist Frequency (Candès et al., 2008; Baraniuk, 2007). The key underlying principle of CS is sparsity, which means that most of the signal components in some domain are zero, and therefore the signal is highly compressible. If the signal is compressible in some domain, then the uncompressed signal can be extracted by solving the following optimization problem:

$$\begin{aligned} &\text{Minimize} \quad ||s||_1 \\ &\text{Subject to} \quad Ks = b \end{aligned} \tag{1.5}$$

In this problem, b is the compressed signal, K is the sensing matrix, and s is the uncompressed signal. This is an underdetermined system because K has more columns than rows, and the minimization of the l1-norm induces sparsity. This problem can be formulated as a second-order cone programming problem and solved with well-known interior-point method algorithms (Alizadeh and Goldfarb, 2003).

CS has diverse applications across various fields like geophysics, astronomy, and medicine, showcasing its adaptability and efficiency in different domains. For instance, in astronomy, Korde-Patel et al. (2022) employed CS in space-based observatories for detecting gravitational microlensing events, significantly reducing data storage and transmission requirements. Similarly, in geo-

physics, Yao et al. (2013) utilized CS to analyze seismic wave radiation from earthquakes, shedding light on the mechanics of subducting plate interfaces. In the medical field, CS has revolutionized diagnostic techniques. Studies by Sandilya and Nirmala (2017) and Zonoobi and Kassim (2014) demonstrate its effectiveness in enhancing magnetic resonance imaging and reconstructing electrocardiogram signals. These examples underscore the versatility of CS in processing complex signals across a spectrum of scientific domains, from deep space to the human body.

Interestingly, the system in equation 1.5 is analogous to the mixing system of stray magnetic field noise that occurs on a spacecraft. In this case, b represents the magnetometer signals, s is the vector of source signals, and K defines the magnitude and polarity of each stray magnetic field signal at each magnetometer. By assuming that the natural magnetic field is equally present at each magnetometer, CS can be used to separate stray magnetic field noise from natural magnetic field signals (Hoffmann and Moldwin, 2022).

Another important condition for the successful application of CS is that the mixing matrix K satisfies the Restricted Isometry Property (RIP). The RIP measures how close a subset of the columns of K are to being orthogonal (Candès, 2008). The RIP parameter, δ, is calculated by the following equation:

$$(1-\delta)||s||_2^2 \leq ||Ks||_2^2 \leq (1+\delta)||s||_2^2 \tag{1.6}$$

The RIP parameter δ ranges from 0 to 1. If δ is near 0, then the columns of K are nearly orthogonal. This orthogonality enables CS to successfully discriminate signal components. In a spacecraft, this is similar to measuring how far apart each noise-maker is from each other. The proximity of these noise sources significantly impacts the measured signal amplitude at each magnetometer. For example, if two noise sources are very close to each other, then the CS algorithm will struggle to distinguish them. CS is a powerful signal processing technique with promising applications in space physics. In this dissertation, it is applied to remove stray magnetic field interference from in situ magnetic field measurements. CS is a versatile tool for separating signals in a wide range of contexts.

1.6 Thesis Scope and Overview

The aim of this thesis is to resolve the intricate challenges associated with the precise measurement of magnetic fields in space plasmas. Magnetic fields play a crucial role in our understanding of the flow of mass, energy, and momentum in space plasmas. However, stray magnetic fields generated by the spacecraft's own electrical systems interfere with the data collected by onboard magnetometers. This thesis has two goals: first, it seeks to develop computational algorithms capable of mitigating the effects of these stray magnetic field interference on magnetometer data. Second, it contributes to the research community by developing an open-source tool that aims to standardize methodologies and encourage future research in the area of magnetic noise removal. Through the use of advanced signal processing techniques, the overarching objective is to pave the way for the adoption of boomless magnetometers, and revolutionize current design paradigms that rely on mechanical booms to distance the sensors from the sources of interference on the spacecraft. This breakthrough would allow low cost platforms such as CubeSats to take high fidelity magnetic field measurements and participate in the era of heliophysics. The following sections of this dissertation will detail the steps taken to achieve these objectives, systematically outlining the content and focus of each chapter.

1.6.1 Separation of Spacecraft Noise From Geomagnetic Field Observations Through Density-Based Cluster Analysis and Compressive Sensing

The second chapter of this thesis offers an alternative to the traditional solutions currently used to mitigate magnetic noise. Conventionally, long mechanical booms are deployed to distance magnetometers from the noise-generating components of the spacecraft. However, this method presents challenges such as increased complexity and cost. This chapter introduces a novel, two-step computational algorithm designed to bypass these challenges. The two-step algorithm is called Underdetermined Blind Source Separation (UBSS) because it can separate unknown noise sources when there are more noise sources present than magnetometers. The first step of UBSS involves the use

of density-based cluster analysis, a technique that identifies stray magnetic noise sources. This is achieved without any prior knowledge of the number, location, or amplitude of these interference signals. Following this identification phase, the algorithm employs compressive sensing to separate these noise signals from the ambient magnetic field signal. The chapter validates the proposed algorithm through simulations and laboratory experiments, using data from the low-Earth orbiting satellite Swarm to simulate the ambient magnetic field. Ultimately, this chapter aims to simplify the magnetometer design by negating the need for mechanical booms, and presents the first application of UBSS to remove stray magnetic field noise. The contents of this chapter have been published in Hoffmann and Moldwin (2022).

1.6.2 Enabling Boomless CubeSat Magnetic Field Measurements with the Quad-Mag Magnetometer and an Improved Underdetermined Blind Source Separation Algorithm

The third chapter of this dissertation builds upon the foundational work of Chapter 2 and introduces a noise removal suite composed of the Quad-Mag CubeSat magnetometer and an improved version of the UBSS algorithm for noise removal. The Quad-Mag sensor comprises four magnetometers housed in a single CubeSat form-factor card, designed to facilitate distributed measurements of stray magnetic fields. The accompanying UBSS algorithm is capable of eliminating these stray fields without requiring prior information about the magnitude, orientation, or number of noise sources. The algorithm uses the same two-stage approach involving cluster analysis for signal identification and compressive sensing for noise separation. Additionally, we incorporate single-source point detection and iteratively-weighted compressed sensing to further refine the noise identification and separation processes.

Through lab experiments using a mock CubeSat, we show that the UBSS algorithm reduces noise levels from over 100 nT at each magnetometer to below the expected instrument resolution of 5 nT at 65 Hz. Simulations further confirm the efficacy of the combined Quad-Mag and enhanced

UBSS system across various CubeSat sizes, including 1U, 2U, 3U, and 6U configurations. The findings indicate that this integrated system offers a viable pathway for achieving high-fidelity magnetic field measurements on CubeSats without the need for a deployable boom. The results from this chapter have been published in Hoffmann et al. (2023).

1.6.3 Wavelet-Adaptive Interference Cancellation for Underdetermined Platforms: Enhancing Boomless Magnetic Field Measurements on Compact Spacecraft

The fourth chapter introduces another novel technique for magnetic interference cancellation, specifically designed for compact, resource-constrained spacecraft like CubeSats. The algorithm, titled Wavelet-Adaptive Interference Cancellation for Underdetermined Platforms (WAIC-UP), utilizes wavelet analysis to separate stray magnetic field signals from the ambient magnetic field signal. It capitalizes on the unique spectral properties of different sources of magnetic interference and employs an analytical methodology to separate them from the ambient magnetic field in the wavelet domain. The chapter provides robust validation for WAIC-UP through a series of Monte Carlo simulations, designed to mimic a variety of interference conditions one could encounter on a 1U CubeSat, and real-world tests on a mock 3U CubeSat using stray magnetic fields generated by copper coils. This chapter demonstrates that WAIC-UP can perform these tasks with a fraction of the computational time required by other contemporary noise removal algorithms. This efficiency makes it an especially attractive option for small, resource-constrained spacecraft, thus opening up new possibilities for small-satellite-based scientific missions in space. Additinally, the low-computational complexity of the WAIC-UP algorithm may enable real time noise removal using low-power processors onboard the spacecraft. This would reduce the need for ground-processing and remove some of the delay for near-real time space weather products. This chapter has been published in Hoffmann and Moldwin (2023).

1.6.4 MAGPRIME

In the fifth chapter, a comprehensive tool for mitigating stray magnetic field interference in magnetometer data is introduced. This tool, dubbed MAGPRIME (MAGnetic signal PRocessing, Interference Mitigation, and Enhancement), serves as an open-source Python library that includes a suite of noise removal algorithms developed by the community. MAGPRIME leverages the sophisticated techniques developed in the realm of magnetometer signal processing and brings them together into an intuitive, user-friendly platform. The chapter presents an in-depth review of MAGPRIME, describing its design, structure, and unique functionalities. Furthermore, the functionality of MAGPRIME extends to the facilitation of future research, enabling researchers the ability to test and customize noise removal methods. A series of benchmark results are demonstrated using MAGPRIME, highlighting the performance of various modern noise removal algorithms. MAGPRIME opens the gateway to an efficient and effective handling of magnetometer data for compact, resource-limited spacecraft, enabling a new wave of scientific missions in space and research in interference removal.

1.7 Open Science Statement

This thesis work embraces the principles of open science by making the data and code openly available to the research community. Following NASA and AGU's open data policies, all simulation data, software implementations, and experimental measurements used in this dissertation have been archived and published in public repositories (Hoffmann, 2023, 2022). This allows other researchers full access to replicate, reproduce, and build upon the findings reported here. By contributing to open science, this work aims to increase transparency, foster collaboration, and uphold the integrity of the scientific process. The availability of the data and code developed in this thesis is critical to ensuring the results are verifiable, reproducible, and can provide maximum benefit to the space science community.

CHAPTER 2

Separation of Spacecraft Noise from Geomagnetic Field Observations through Density-Based Cluster Analysis and Compressive Sensing

This chapter focuses on the development and validation of the Underdetermined Blind Source Separation (UBSS) algorithm to remove stray magnetic noise in spaceborne magnetometer measurements. Traditional methods that use mechanical booms to distance magnetometers from spacecraft noise sources are effective but have limitations, particularly for small spacecraft such as CubeSats. UBSS leverages density-based cluster analysis and compressive sensing to identify and separate spacecraft-generated magnetic noise from geomagnetic field data. This method does not require prior knowledge of the number, location, or amplitude of the noise sources, but assumes they have minimal overlapping spectral content. We validate this algorithm through a series of tests designed to separate high latitude geomagnetic perturbations recorded by the Swarm satellite from artificial CubeSat noise in both simulations and laboratory experiments. This chapter highlights how the UBSS algorithm effectively resolves situations where the number of noise sources exceeds the number of available magnetometers and circumvents the need for long mechanical booms.

The contents of this chapter have been published in the American Geophysical Union's Journal of Geophysical Research: Space Physics and can be accessed at https://agupubs.onlinelibrary.wiley.com/doi/full/10.1029/2022JA030757. For further insight into the noise signals generated during our simulations and laboratory experiments, these are available on the University of Michigan Deep Blue data repository at https://doi.org/10.7302/bz6v-6q52.

2.1 Introduction

Spacecraft equipped with magnetometers can be used to capture in situ measurements of magnetic phenomena in the geospace environment. These measurements are necessary to answer key questions about the nature of the Earth's magnetosphere and its interaction with interplanetary magnetic fields. Understanding how the heliosphere directs the flow of energy, mass, and momentum between the Sun and Earth is critical for applications such as space weather modeling, space exploration, and climate science. A number of missions use spacecraft equipped with magnetometers to measure magnetic fields. For example, The European Space Agency's Swarm mission uses a constellation of three satellites to provide high fidelity magnetic field measurements used to model the Earth's magnetic field and study the Earth's dynamo (Fratter et al., 2016). Magnetometers provide invaluable data for space science research, however, the quality of the data are often limited by magnetic noise generated by the spacecraft. Electrical systems onboard a spacecraft generate stray magnetic fields that interfere with magnetic field measurements. The strength of magnetic fields in the geospace environment ranges several orders of magnitude with natural phenomena such as the interplanetary magnetic field occurring on the order of 6 nT to the Earth's magnetosphere in low Earth orbit measuring on the order of 60,000 nT. Spacecraft sub-system magnetic fields may completely eclipse the natural magnetic fields which are of interest to understanding waves and currents in the solar wind and magnetosphere. The presence of these stray magnetic fields is a significant obstacle for missions that utilize magnetic field data (Russell, 2004; Ludlam et al., 2009).

On satellites, stray magnetic fields can be generated by subsystems such as solar panels, reaction wheels, battery currents, and magnetorquers. The magnetometer on the CubeSat, Ex-Alta 1, recorded magnetic field noise generated by a magnetorquer which exceeded 7500 nT peak-to-peak (Miles et al., 2016). Satellite magnetometers are typically fixed at the end of a mechanical boom to reduce the magnitude of noise generated by the spacecraft. For example, the mission Swarm uses two magnetometers mounted on a 4.3 meter boom (McMahon et al., 2013). However, the use of a boom is not always possible in designs such as rovers and CubeSats where gravity and cost are

limiting factors. Additionally, the implementation of a boom does not always guarantee the elimination of spacecraft noise from magnetic field measurements. The spacecraft, DMSP, employs a single magnetometer on the end of a 5 meter boom, but still faces issues with spacecraft noise (Kilcommons et al., 2017).

The use of a single magnetometer on a spacecraft requires a careful magnetic cleanliness design and characterization of the spacecraft's magnetic signature in order to minimize or remove stray magnetic fields. In the case of the spacecraft Cassiope, a software update changed the behavior of the spacecraft's fluxgate magnetometer (MGF). Special spacecraft maneuvers to decrease the spacecraft's noise signature were required in order to recalibrate the MGF (Miles et al., 2019). Algorithms to autonomously identify spacecraft noise would allow Cassiope to do in situ interference mitigation without special spacecraft maneuvers.

In spacecraft with multiple magnetometers, the traditional way to cancel stray magnetic field noise is to perform gradiometry. Gradiometry is a technique which compares magnetometer signals from two spatially separated sensors and calculates the gradient of between them. Ness et al. (1971) uses the gradient to fit a dipole to the spacecraft noise and formulate a coupling matrix. The coupling matrix is then used to subtract the spacecraft noise from the magnetometer measurements. This method can also be applied to higher order magnetic fields but requires arduous pre-flight characterization of the spacecraft's magnetic signature. Ream et al. (2021) uses gradients in the frequency domain to identify and suppress spacecraft noise. However, this method assumes that the spectra of the ambient magnetic field and the spacecraft noise do not overlap. Pope et al. (2011) uses the axial gradients and fuzzy logic to identify spacecraft noise according to the subsystem that generates it. The identified noise segments are then corrected in the time domain using information about the noise generated by the subsystem. This method is successful at identifying and removing many different individual noise sources, however, it is not designed to correct multiple concurrent noise sources.

Other noise cancellation methods employ state estimation of the magnetic fields generated by spacecraft subsystems by examining spacecraft housekeeping data. Deshmukh et al. (2020) uses a

supervised machine learning algorithm in order to estimate the transfer function of housekeeping currents to stray magnetic fields. Total knowledge of a spacecraft's magnetic signature would allow for perfect interference cancellation, however, housekeeping telemetry provides an incomplete mapping of a spacecraft's current distribution. Additionally, housekeeping data are often sampled at a low cadence and may not have the appropriate bandwidth to identify higher frequency noise. For low cost applications with a large number of spacecraft, such as CubeSat constellations, it is advantageous to use an algorithm that does not require a boom, rely on prior knowledge of the spacecraft's magnetic signature, or requires human analysis.

Recent progress has been made in magnetometer noise cancellation through the application of blind source separation (BSS) algorithms. BSS is the separation of a mixture of source signals without prior knowledge of the signal type or magnetometer location. Constantinescu et al. (2020) use Maximum Variance Analysis (MVA) to clean spacecraft magnetometer data. The MVA algorithm finds an orthogonal set of axes to maximize the variance of the measured signals. These axes represent the principle components which are used to identify and remove noise sources. This application of MVA requires that the variance in the noise sources is larger than the variance in the background magnetic field, and can only identify a limited number of noise signals. Imajo et al. (2021) proposed the use of Independent Component Analysis (ICA) to separate geomagnetic field data, captured by the satellite Michibiki-1, from stray magnetic field noise. This algorithm separates signals based on statistical independence, and works well when the number of noise sources are not more than the number of magnetometers (Naik and Kumar, 2009). The MVA and ICA algorithms both separate signals through optimizing statistical quantities, however, they are limited by the number of noise signals they can identify. Sheinker and Moldwin (2016) proposed a novel BSS algorithm that uses an analytical formulation to estimate the gain of a single noise source between magnetometers. This method is designed for the case in which a single noise source is present, and does not account for the presence of multiple noise sources. Although, the method may be adapted to remove multiple noise sources by adding more magnetometers.

In this work, we present the application of a UBSS algorithm based on the unsupervised

machine learning algorithm, Density Based Spatial Clustering of Applications with Noise (DBSCAN), and compressive sensing to separate the ambient magnetic field from spacecraft noise. UBSS is a class of problems in which there are M sensors and N unknown source signals such that $M < N$. The M sensors, defined by the complex signals $\boldsymbol{B}(t,k) \in \mathbb{C}^M$, contain a mixture of the N source signals, defined by $\boldsymbol{S}(t,k) \in \mathbb{C}^N$. At the time-frequency bin, (t,k), the source signals combine in an unknown mixing matrix $\boldsymbol{K} \in \mathbb{C}^{M\times N}$. In UBSS, no prior knowledge of the source signals is assumed and the number of source signals that can be separated is not limited by the number of sensors. The system used to model UBSS is defined by the following relationship.

$$\mathbf{B}(t,k) = \mathbf{KS}(t,k) \tag{2.1}$$

UBSS is a topic that has been thoroughly researched in other fields such as acoustics and radar signal processing. In the field of acoustics, this problem is famously referred to as the cocktail party problem. In the cocktail party problem, there is a room full of people each having conversations. An array of microphones is placed in the room to record the concurrent conversations. The microphone recordings are then used to separate each individual voice. Guo et al. (2017) demonstrate the separation of four human voices using three microphones. He et al. (2021) also demonstrate the separation of six flutes recorded by three microphones using the DBSCAN algorithm.

Due to the spatial structure of magnetic fields, the same algorithms developed to solve the cocktail party problem can not be directly applied to magnetic noise cancellation. When considering a dipole noise source, the vector magnetic field will have a different magnitude and polarity depending on the magnetic latitude and radial distance of the magnetometer. In this work, we model the spatial structure of magnetic fields with a phase, although magnetic noise signals mix instantaneously. The structure of the magnetic noise signal is not always dipolar, and will change depending on the geometry of the noise source. In magnetic underdetermined blind source separation, the mixing matrix, K, is a complex matrix representing the gain and phase of each signal at each magnetometer. In radar signal processing, Bai et al. (2021) apply a similar approach by using complex mixing matrices to model time-delayed radar signals with different directions of arrival.

In this work, we use DBSCAN to estimate the mixing matrix, K. Once K is known, compressive sensing is used to restore the geomagnetic field signal from the noisy magnetometer data.

We present two experiments to validate this algorithm. The first experiment separates four computer-simulated noise signals from an ambient magnetic field signal. The second experiment separates the same ambient magnetic field signal using real magnetic field data recorded using an experimental CubeSat apparatus with copper coil generated signals and three PNI RM3100 magnetometers (Regoli et al., 2018b). The aim of this work is to develop a robust signal processing algorithm to remove spacecraft noise and minimize the need for a mechanical boom or a magnetically clean spacecraft. This work focuses on developing a noise cancellation algorithm for geomagnetic field data, but can also be applied to remove noise in measurements of planetary magnetospheres and interplanetary magnetic fields.

2.2 Methodology

We employ a two-step method to eliminate spacecraft noise and recover the true ambient magnetic field. The initial phase involves identifying the mixing matrix, K, as outlined in equation (2.1). To accomplish this, we first preprocess the magnetometer data to make it suitable for clustering, then utilize cluster analysis to determine the structure of K, which describes how different noise sources combine in the magnetometer readings. Following this, compressive sensing is employed in the second phase to separate the ambient magnetic field from the noise signals. Here, the previously determined mixing matrix, K, facilitates the separation of the combined magnetometer signals through convex optimization techniques. This two-step approach is applied to the data from each axis of the magnetometer individually. The signal preprocessing, cluster analysis, and compressive sensing techniques are detailed in the following sections.

2.2.1 Signal Preprocessing

The separation of magnetic field signals from stray magnetic fields is analogous to a problem thoroughly researched in other fields such as acoustics and is called UBSS. This problem has been heavily investigated for microphone and radar arrays, but the unique spatial structure of magnetic fields introduces new complications which have not been well-researched. When considering a dipole noise source, the placement of magnetometers at different magnetic latitudes alters the magnitude and polarity of the noise signal. We model this effect as a phase, despite the noise sources mixing instantaneously. The time-frequency domain mixing model, B(t,k) = KS(t,k), is defined by the following system:

$$\begin{bmatrix} B_1(t,k) \\ B_2(t,k) \\ \vdots \\ B_m(t,k) \end{bmatrix} = \begin{bmatrix} 1 & k_{12}\angle\phi_{12} & k_{13}\angle\phi_{13} & ... & k_{1n}\angle\phi_{1n} \\ 1 & k_{22}\angle\phi_{22} & k_{23}\angle\phi_{23} & ... & k_{2n}\angle\phi_{2n} \\ \vdots & \vdots & \vdots & \ddots & \vdots \\ 1 & k_{m2}\angle\phi_{m2} & k_{m3}\angle\phi_{m3} & ... & k_{mn}\angle\phi_{mn} \end{bmatrix} \begin{bmatrix} S_1(t,k) \\ S_2(t,k) \\ \vdots \\ S_n(t,k) \end{bmatrix} \tag{2.2}$$

In this mixing system, the signals $S_i(t,k)$ are the source signals at time t and frequency k. The ambient magnetic field signal we seek to recover, $S_1(t,k)$, is assumed to be identical at each magnetometer and is represented by a column of ones in the mixing matrix. In the geospace environment, this allows us to observe phenomena such as ultra-low frequency (ULF) waves which have frequencies less than 5 Hz (Jacobs et al., 1964). The phases, $\phi_{ij} = \{0, \pi\}$, in the mixing matrix, K, account for the difference of a signal seen by magnetometers at different magnetic latitudes. The phase, ϕ_{ij}, is determined by the spatial structure of the noise signal, which depends on the geometry of the noise source. This model does not require that noise sources be dipolar. The value in the mixing matrix $k_{ij}\angle\phi_{ij}$ represents the complex value $k_{ij}e^{j\phi_{ij}}$. This value defines presence of the signal $S_j(t,k)$ at magnetometer $B_i(t,k)$.

Sparsity is a precondition of both mixing matrix estimation and compressive sensing, however, spacecraft noise signals are not often sparse in the time domain. The magnetometer signals, b(t), are transformed into the Time-Frequency (TF) domain using a Fourier transform in order to

increase signal sparsity. Typically, the Short-Time Fourier Transform (STFT) is used because signals that are present in multiple time windows will provide more data points to be clustered. As a result, periodic signals are easier to identify and remove than aperiodic signals. However, aperiodic signals can be separated with sufficient time-frequency resolution. In this work, we use the Non-Stationary Gabor Transform (NSGT) to transform magnetometer signals into the Time-Frequency domain. NSGT has advantages over the STFT because it allows the user to evolve the window size with respect to frequency (Holighaus et al., 2013). As a result, high and low frequencies are not limited to the same window size, and frequency resolution is constant across the frequency spectrum. Figure 2.1 showcases example spectrograms generated using the Short-Time Fourier Transform and the Nonstationary Gabor Transform.

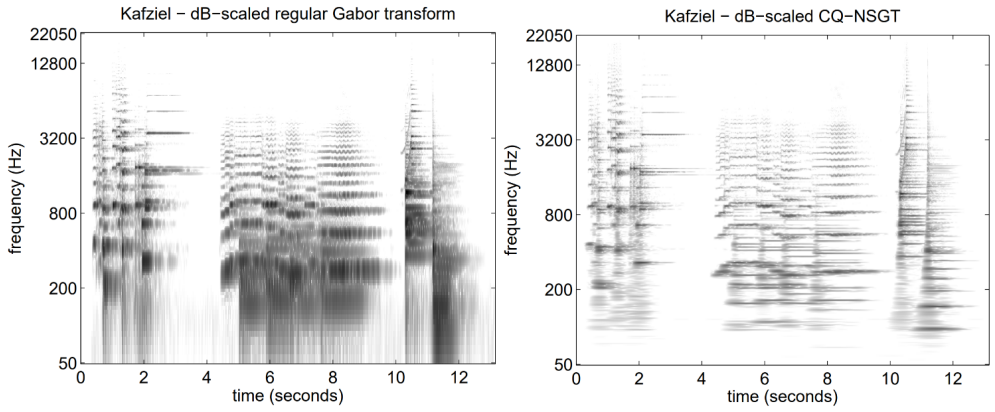

Figure 2.1: The left panel displays the STFT spectrogram of a 13-second segment where the violin and piano are played together. The right panel exhibits the NSGT spectrogram of the same piece. The variable window size of the Non-stationary Gabor Transform significantly enhances the time-frequency granularity, similar to that of a wavelet transform. The improvement in sparsity is visually evident from the increased white space in the right panel (Figure from Holighaus et al. (2013)).

In order to apply the NSGT, the user specifies a quality, Q, and the lowest frequency they would like to observe. The parameter, Q, is used to automatically calculate the window size with respect to the desired frequency resolution. In comparison to the STFT, the NSGT provides finer frequency resolution at low frequencies and better time resolution at higher frequencies. We perform the Non-Stationary Gabor Transform to obtain the UBSS model B(t,k) = KS(t,k). The mixing system of

a sparse time-frequency bin where only the signal, S_j(t,k), is present can be defined by a single mixing vector:

$$\begin{bmatrix} |B_1(t,k)| \\ |B_2(t,k)| \\ \vdots \\ |B_m(t,k)| \end{bmatrix} = \begin{bmatrix} k_{1j} \\ k_{2j} \\ \vdots \\ k_{mj} \end{bmatrix} |S_j(t,k)| \tag{2.3}$$

The operator $|a+jb|$ applied to the complex value $a+jb$ returns the magnitude of complex value, $\sqrt{a^2+b^2}$. equation (2.3) can be rewritten element-wise as:

$$|S_j(t,k)| = \frac{|B_1(t,k)|}{k_{1j}} = \frac{|B_2(t,k)|}{k_{2j}} = ... = \frac{|B_m(t,k)|}{k_{mj}} \tag{2.4}$$

equation (2.4) is equivalent to the symmetric form of a line with slope defined by the mixing vector of the noise signal. In order to find the mixing vector of a noise signal, we define a time-frequency space $\mathbf{H} \in \mathbb{R}^{2m}$ in which each phase and magnitude of the m magnetometer signals are a coordinate. Sparse TF points will draw straight lines through the origin in the **H**-domain with a slope proportional to the signal's mixing vector. Figure 2.2 shows an example of a scatter plot of three mixed time-frequency signals composed of six source signals. The mixed signals form straight lines with slopes defined by equation (2.4).

2.2.2 Mixing Matrix Estimation

The slope of the lines drawn through the **H**-domain are not easily clusterable in their current form as a collection of scattered data points. We transform the scattered data points in **H**-domain into a clusterable form by projecting the magnitude subdomain onto a unit hypersphere. The **H**-domain magnitude data are projected onto a half-unit hypersphere by normalizing the time-frequency magnetometer data via the following equation.

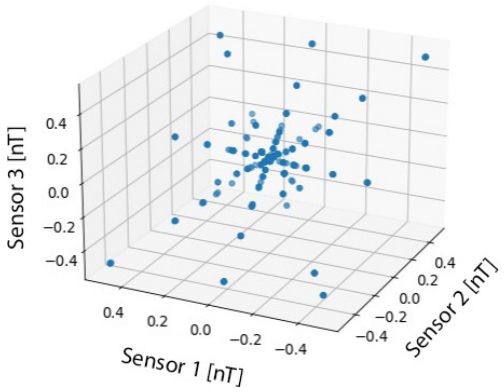

Figure 2.2: Three magnetometer measurements of six computer simulated sinusoidal noise signals. Each magnetometer signal is transformed into the time-frequency domain using the STFT. The magnitude of the three resulting TF signals are taken and plotted against each other in a scatter plot. The scattered time-frequency points from each magnetometer form straight lines due to equation (2.4). This figure does not include the phase subdomain of the **H**-domain.

$$B^*(t,k) = \frac{|B(t,k)|}{\|B(t,k)\|} \tag{2.5}$$

When the scattered data points have been normalized, they collapse into compact clusters. This is illustrated by the projection of the scattered data points representing six computer generated signals in Figure 2.2 onto a half-unit hypersphere in Figure 2.3. The centroid of a cluster is proportional to the mixing vector of a noise signal as defined in equation (2.2).

The majority of the frequency space is filled with negligible energy points that will project randomly onto the unit hypersphere (Sun et al., 2016). We attempt to cleanse the data of these points using a magnitude filter. The filter is applied by finding the average signal magnitude and removing data points below a factor, λ, of the average signal magnitude. The magnitude filter is applied by removing data points that do not satisfy the following criterion:

$$|B(t,k)| > \lambda \cdot \text{avg}(|B(t,k)|) \tag{2.6}$$

The projected data points form tightly clustered groups on the unit hypersphere that allow us to discover the relative gain between noise signals at different magnetometers. However, we need to

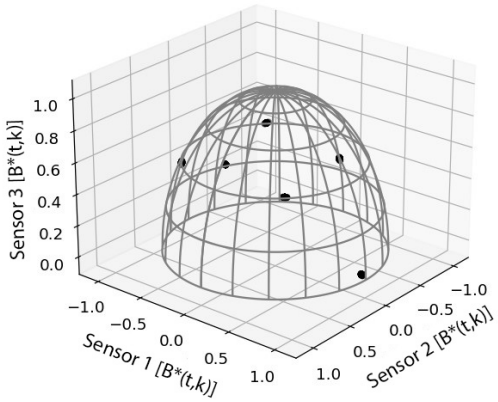

Figure 2.3: The scattered time-frequency mixed signals in Figure 2.2 are projected onto a half-unit hypersphere through normalization. The six scattered straight lines collapse into six compact clusters. The centroid of each cluster is proportional to each source signals' mixing vector in the mixing matrix, K, due to equation (2.4).

find the relative phases between noise signals of magnetometers at different positions. To account for this we join each projected time-frequency point to its relative argument. The relative argument is defined by the following transformation:

$$\arg B(t,k) = \{\, \arg B_j(t,k) - \arg\left(B_0(t,k) \mid j \in [0,m]\right) \} \tag{2.7}$$

Using the result of equation (2.7), we define a new data format, H(t,k), by concatenating the projected magnitude data with the argument of the time-frequency data.

$$H(t,k) = (B^*(t,k), \arg\left(B(t,k)\right) \tag{2.8}$$

The magnetometer data, H(t,k), are now in a format that can be clustered to discover the gain and phase of each signal described in the mixing matrix, K. Figure 2.4 shows an example of two magnetometer signals transformed into the **H**-Domain.

Now that the projected magnitude and relative phases are joined, a variety of clustering algorithms can be applied to find the mixing matrix, K. In this work, we use the DBSCAN algorithm because it does not require user input to discern the number of clusters present, and it will ignore

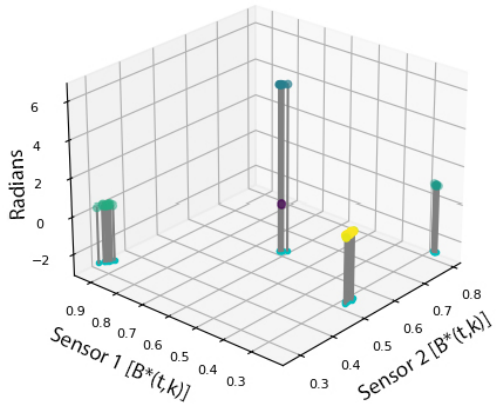

Figure 2.4: An illustration of noise signals in the full **H**-domain for a two magnetometer system. The horizontal axes represent the magnitude of the time-frequency magnetometer signals projected onto a unit hypersphere. The vertical axis represents the relative argument of Sensor 2 in radians as defined by equation (2.7). The data points are projected onto a plane at Z = -2.5 to distinguish the difference in magnitudes. The phase and magnitude of each noise signal at each magnetometer is discovered by clustering the data in this format.

noise points (Ester et al., 1996). As a result, the number of noise signals does not need to be defined prior to the application of DBSCAN. DBSCAN has two essential parameters, *eps* and *minPts*, that allow this functionality. The maximum distance for two points to become neighbors is the value, *eps*. If a point has *minPts* number of neighbors, it is called a core point. Core points are used to define each cluster. If a point is more than *eps* distance away from any point in a cluster, it is labeled as noise. We use DBSCAN to cluster H(t,k) and use each cluster's centroid as the noise signal's mixing vector. Once the mixing vector of each noise signal is known, the mixing vectors are joined to form the mixing matrix, K. The mixing matrix is used to separate the noise signals from the ambient magnetic field via compressive sensing.

2.2.3 Signal Reconstruction

Compressive sensing is a method commonly used to reconstruct sparse signals from samples taken at a rate below the Nyquist frequency, which is typically twice the signal's bandwidth (Baraniuk, 2007). This technique excels in scenarios where the signal of interest is sparse in some domain, allowing for the recovery of the signal from fewer samples than what is traditionally required.

The principle of reconstructing a signal of length N from a sampled signal of length M, where $M < N$, presents a parallel to the challenges faced in UBSS. In UBSS, however, we do not deal with signals that are undersampled in the time domain, but in the sense of having fewer observations (magnetometers) than the number of sources to be separated.

Ordinarily, the system $b = Ks$, where K is a wide matrix, has infinitely many solutions because if $b = Ks$ is a solution, $b = K(s + s')$ is also a solution for any vector s' in the null space of K. Compressive sensing can exactly recover sparse signals and approximate near-sparse signals through minimizing the L1 norm of S with respect to $b - Ks < \varepsilon$. For the separation of signals within the UBSS framework, we utilize CVXPY, a Python-Embedded Modeling Language for Convex Optimization, with the estimated mixing matrix, K, to demix the signals (Diamond and Boyd, 2016).

$$\begin{aligned} &\text{Minimize} \quad w^T|s| \\ &\text{Subject to} \quad Ks = b \end{aligned} \tag{2.9}$$

Traditionally, compressive sensing minimizes the L1 norm of the source signals, $\|s\|_1$, with respect to Ks = b in order to recover the source signals. Instead of minimizing the L1 norm, we utilize a weighted L1 norm defined by the weighting vector, $w = [w_1,\ 1,\ 1,\ ...,\ 1]^T$, where $w_1 \geq 1$. The parameter, w_1, is multiplied with the ambient magnetic field signal, s_1, in order to deter the attribution of energy from other noise signals to it. In the case that the source signals, s, are not sparse at a time-frequency bin, the additional weight increases the cost of attributing energy from other signals to the ambient magnetic field, s_1. The optimal value of the weight, w_1, depends on the signature of noise signals. Candès et al. (2008) apply a similar approach by iteratively adjusting the weight of each signal with respect to the magnitude of the signal. In this work, we found the optimal weight, w_1, experimentally by comparing the reconstructed signal, $\hat{s}_1$, to the true signal, s_1.

This system defined in equation (2.9) is solved using the Embedded Conic Solver (Domahidi et al., 2013). The Embedded Conic Solver (ECOS) algorithm is a convex optimization algorithm

that transforms the problem defined in equation (2.9) into a Second Order Cone Problem (SOCP). SOCP problems are convex optimization problems that minimize linear functions with respect to second order cone constraints (Alizadeh and Goldfarb, 2003). The ECOS algorithm applies an interior point solver to converge on the sparse solution of the problem defined by equation (2.9).

ECOS is a highly robust solver; however, it is also very computationally expensive. Alternative algorithms may converge more quickly in specific sparse recovery problems. The Fast Iterative Shrinkage-Thresholding Algorithm (FISTA) has been shown to improve convergence time by using a Lipschitz gradient to modulate step size (Beck and Teboulle, 2009b,a). Another method, called the split Bregman method, decomposes the source separation problem into smaller subproblems to simplify computation (Yu et al., 2010). In contrast, ECOS, a generic conic solver, relies on interior point methods which, despite their versatility in handling any convex optimization problem, are inherently slower due to their general-purpose nature. In this work, we apply the ECOS solver; however, faster solvers may be better suited for operational applications.

2.3 Experimental Data and Results

We test the proposed method of signal and noise separation through two experiments. The first experiment demonstrates the separation of Swarm magnetic field data from computer simulated signals using virtual magnetometers. The second experiment demonstrates the separation of Swarm magnetic field data from real magnetic noise signals generated with copper coils. The coil-generated magnetic fields were measured using the PNI RM3100 magnetometer and a mock CubeSat described by (Deshmukh et al., 2020).

Figure 2.5 details the process of identifying noise signals and reconstructing the ambient magnetic field. First (i), the signal offsets are subtracted to center the signals around 0 nT. Second (ii), the signals are transformed into the time-frequency domain using the Non-Stationary Gabor Transform to increase signal sparsity. Third (iii), low energy points are filtered out using equation (2.6). Fourth (iv), the signals are transformed into H(t,k) by projecting the magnitude, $|B(t,k)|$

onto the unit hypersphere and concatenating it with the phase, $\arg B(t,k)$, via equations 2.5, 2.7, and 2.8. Fifth (v), the data, H(t,k), are clustered using DBSCAN and the cluster centroids are found. Finally, in the last step (vi), compressive sensing is used to reconstruct the ambient magnetic field. The minimum magnitude, λ in step iii, and the parameters eps and MinPts in step v may need to be adjusted depending on the length and magnitude of the signals being analyzed. The two major components of this process are identifying the mixing matrix, K, through cluster analysis in step v, and separating the interference from the ambient magnetic field signal through compressive sensing in step vi.

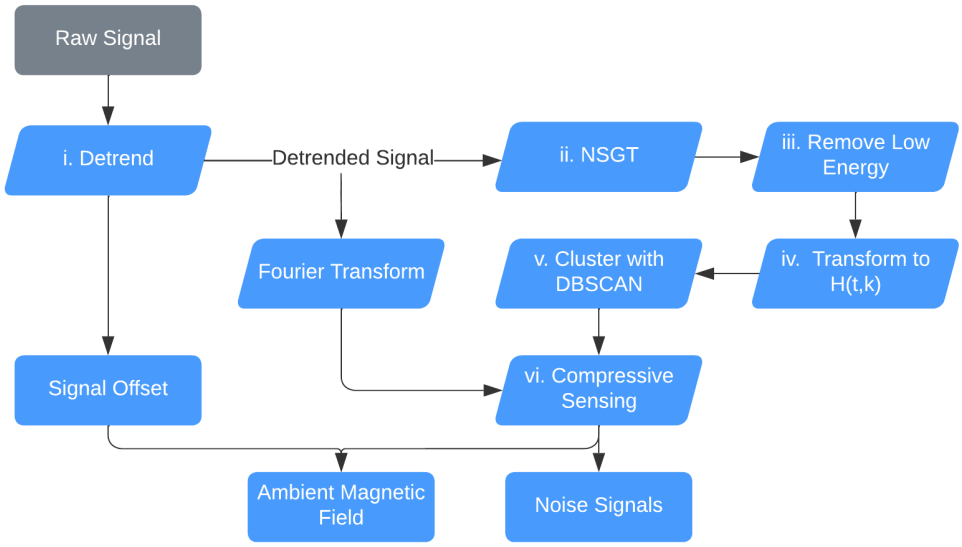

Figure 2.5: Flow of processes involved in using cluster analysis to discover noise signals and compressive sensing to separate the ambient magnetic field from noise signals.

We evaluate the separation of noise signals via three metrics. The metrics are calculated pointwise using the reconstructed signal, x and the true signal, y, over N data points. The first metric is the Pearson Correlation Coefficient. This measurement gives the covariance between the normalized input and recovered signals.

$$\rho = \frac{\sum_{i=0}^{N-1}(x_i - \bar{x})(y_i - \bar{y})}{\sqrt{\sum_{i=0}^{N-1}|(x_i - \bar{x})|^2 \sum_{i=0}^{N-1}|(y_i - \bar{y})|^2}} \tag{2.10}$$

The second metric evaluated is the root mean squared error (RMSE). This metric is proportional

to the magnitude of the squared error. As a result, the RMSE is very sensitive to large errors.

$$RMSE = \sqrt{\frac{\sum_{i=0}^{N-1}(x_i - y_i)^2}{N}} \tag{2.11}$$

The final metric is the normalized RMSE (NRMSE). This metric yields the RMSE as a percentage of the magnitude of the signal being measured. It is used to compare the relative error between signals on different orders of magnitude. We calculate the NRMSE by dividing the RMSE of the signal by the max amplitude of the absolute value of the true, detrended signal, $|y - \bar{y}|_{max}$.

$$NRMSE = \frac{RMSE}{|y - \bar{y}|_{max}} \tag{2.12}$$

2.3.1 Experiment 1: Computer Simulation

In this experiment, we use four simulated noise signals, $s(t) \supset [s_2(t), s_3(t), s_4(t), s_5(t)]$, and three virtual magnetometers $b(t) = Ks(t) = [b_1(t), b_2(t), b_3(t)]$. The signal, $s_1(t)$, is residual magnetic field data created by subtracting data generated by the IGRF model from Swarm magnetic field data. This process leaves only magnetic perturbations present in the magnetosphere. The magnetic perturbation data we use were measured by the Swarm A satellite on March 17th, 2015 between 8:53 and 8:55 UTC. This part of the orbit passes between the 69th and 76th parallel south and was selected to capture perturbations in the southern auroral zone. The proposed algorithm detailed in Figure 2.5 is tested on 100 seconds of data, although it may be applied to a signal of any length provided that there are enough data points to cluster. The signals are combined through the complex mixing matrix in equation (2.13) with phases given in radians.

$$K = \begin{bmatrix} 1\angle 0 & 0.99\angle 0 & 0.09\angle 0 & 0.70\angle 0 & 0.02\angle 0 \\ 1\angle 0 & 0.09\angle \pi & 0.99\angle 0 & 0.70\angle 0 & 0.05\angle \pi \\ 1\angle 0 & 0.12\angle \pi & 0.12\angle \pi & 0.13\angle \pi & 0.99\angle \pi \end{bmatrix} \tag{2.13}$$

The values in the first column represent the ambient magnetic field signal which appears identically

at every magnetometer. Figure 2.6 shows the five source signals used in this simulation. Two of the noise signals are sine waves with frequencies of 2 Hz and 5 Hz. Sine waves are sparse signals that can be represented by a single point in the frequency domain. This makes them easily identifiable by cluster analysis. The two remaining noise signals used are a sawtooth wave with a frequency of 0.7 Hz, and a square wave with a frequency of 3.0 Hz. These signals inhabit a broad frequency spectrum and diminish the sparsity of the mixed signals.

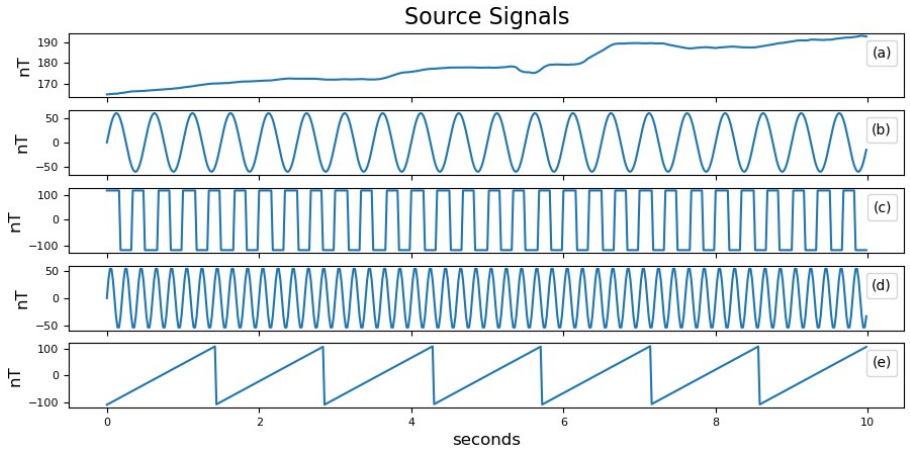

Figure 2.6: Ten seconds of four source signals used to simulate spacecraft noise and one signal to simulate the ambient magnetic field. (a) The ambient magnetic field signal using Swarm A data starting from March 17th, 2015 at 8:53 UTC. (b) A 2 Hz sine wave with amplitude of 50 nT. (c) A 3 Hz square wave with a magnitude of 100 nT. (d) A sine wave with a frequency of 5 Hz and amplitude of 50 nT. (e) A sawtooth wave with an amplitude of 110 nT and frequency of 0.7 Hz.

The signals are combined in the mixing system $b(t) = Ks(t)$ with the mixing matrix K from equation (2.13). The resulting signals are sampled by the virtual magnetometers at a rate of 50 samples per second. Different noise signals, such as noise generated by reaction wheels, may have higher frequency components and require a higher sampling rate in order to avoid aliasing (Pope et al., 2011; Miles et al., 2016). A random normal signal with a standard deviation of 6 nT is added to each virtual magnetometer in order to simulate instrument noise. This noise level corresponds to the rated instrument resolution of the PNI RM3100 magnetometer at 50 Hz used in experiment 2. Figure 2.7 shows the sampled signals.

Following the procedure in Figure 2.5, the signals were detrended and transformed into the Time-Frequency domain using the NSGT. The NSGT is a type of constant-Q transform, so it

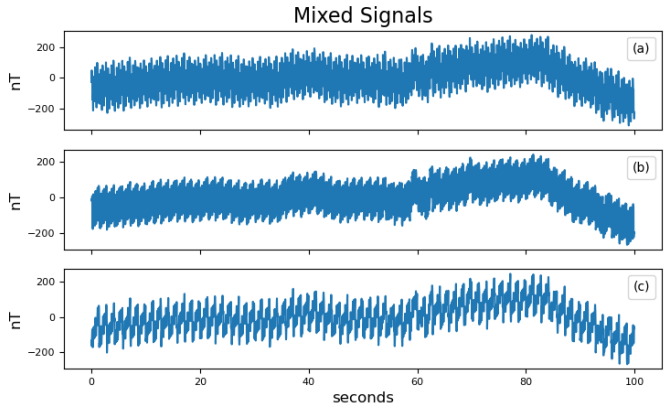

Figure 2.7: Plots (a), (b), and (c) show one hundred seconds of three magnetometer signals, b(t), created by mixing the five source signals in Figure 2.6 though the mixing matrix defined in equation (2.13).

requires the parameter Q which specifies window size. In this experiment, we used $Q = 10$ and a lower frequency bound of 30 mHz. In step 4, low energy points were removed using a $\lambda = 0.5$. The resulting data were transformed into H(t,k) and clustered by DBSCAN with parameters $eps = 0.3$ and $MinPts = 4$. These parameters were optimized experimentally using trial and error, however it may be possible to automate parameter selection based on the signals being analyzed. With this configuration, DBSCAN discovered the five clusters corresponding to each noise source. The clusters, shown below in the columns of $\hat{K}$, closely match the original mixing matrix.

$$\hat{K} = \begin{bmatrix} 1\angle 0 & 0.99\angle 0.00 & 0.697\angle 0.00 & 0.10\angle 0.00 & 0.05\angle 0.00 \\ 1\angle 0 & 0.10\angle -0.02 & 0.697\angle 0.14 & 0.99\angle 0.06 & 0.14\angle 3.10 \\ 1\angle 0 & 0.12\angle -3.10 & 0.135\angle 3.14 & 0.12\angle -3.10 & 0.98\angle -3.16 \end{bmatrix} \tag{2.14}$$

Finally, in step 7, the mixed signals were separated by compressive sensing using the recovered mixing matrix, $\hat{K}$, in equation (2.14). The data, H(t,k), are discarded and the raw Fourier transform of the mixed signals are separated by applying the ECOS algorithm to the problem defined in equation (2.9) with a weight of $w_1 = 1.5$. The reconstructed Swarm perturbation signal is shown in Figure 2.8, as well as a histogram of the reconstruction error and spectrograms of the noisy, cleaned, true Swarm signal.

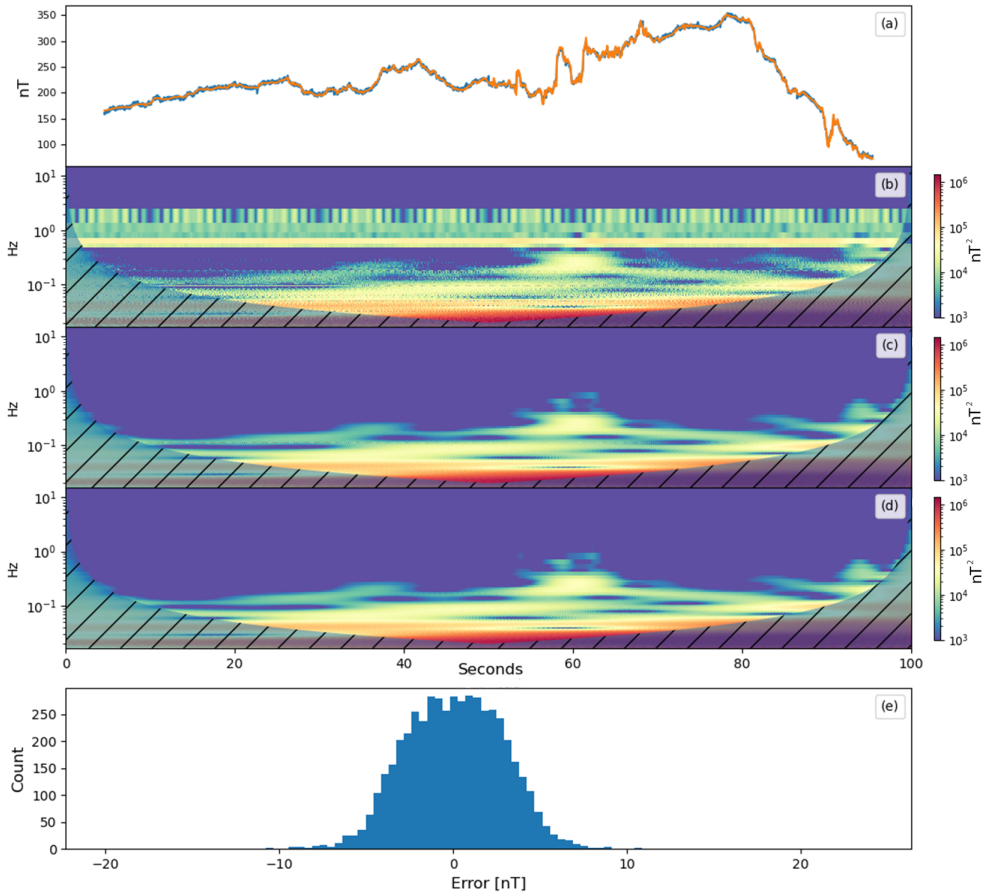

Figure 2.8: The top plot (a) shows the cleaned magnetometer signal in blue with the ambient magnetic field signal overlayed in orange. Plot (b) shows a spectrogram of the uncleaned signal from magnetometer (a) in Figure 2.7. Plot (c) shows a spectrogram of the reconstructed ambient magnetic field signal. Plot (d) shows a spectrogram of the true ambient magnetic field signal. The spectrograms were created using wavelet analysis. The shaded areas indicate where the wavelet does not produce valid results. The bottom plot (d) shows a histogram of the signal reconstruction error, $s_1 - \hat{s}_1$.

The reconstructed ambient magnetic field signal resembles the original signal with some additional error. In order to evaluate the reconstruction noise, the Pearson Correlation Coefficient, RMSE, and NRMSE of each source signal are calculated. The ambient magnetic field was reconstructed with a RMSE of 2.75 nT. The results for the reconstruction of each source signal are shown in Table 2.1. The experiment was repeated without the addition of the 6 nT instrument noise to evaluate the effect of the random noise on the total reconstruction error.

Table 2.1: Summary of Experiment 1 Results.

	Metric	Swarm	Sine A	Square	Sine B	Sawtooth
With Noise	ρ	0.9988	0.9934	0.9983	0.9941	0.9982
	RMSE	2.75 nT	4.11 nT	5.77 nT	6.39 nT	2.54 nT
	NRMSE	1.21%	8.23%	5.77%	6.39%	5.35%
Without Noise	ρ	0.9988	0.9927	0.9987	0.9941	0.9974
	RMSE	2.84 nT	4.33 nT	7.06 nT	6.38 nT	3.42 nT
	NRMSE	0.81%	8.68%	7.06%	6.38%	7.21%

2.3.2 Experiment 2: Magnetic-Coil Generated Signal Separation

In this experiment, we demonstrate the utility of the proposed algorithm on real magnetic field data. We use three PNI RM3100 magnetometers to record copper coil-generated noise signals. Four copper coils are driven by signal generators to create the source signals, $s(t) \supset [s_2(t), s_3(t), s_4(t), s_5(t)]$. The signals are combined in the unknown mixing system, $b(t) = Ks(t) = [b_1(t), b_2(t), b_3(t)]$. The Swarm residual magnetic field data, which is used in experiment one, is added to each magnetometer recording to generate the ambient magnetic field signal, $s_1(t)$.

The proposed algorithm detailed in Figure 2.5 is tested on 100 seconds of recorded data. The signals, $s_2(t)$ and $s_3(t)$, are sine waves with frequencies of 0.4 Hz and 0.8 Hz. The signals, $s_4(t)$ and $s_5(t)$, are square waves with frequencies of 1 Hz and 2 Hz. The three PNI RM3100 magnetometers and four copper coils are placed on the CubeSat apparatus as shown in Figure 2.9. Due to the location and orientation of the four copper coils and three magnetometers, each noise signal will appear at each magnetometer with a different magnitude and magnetic latitude induced phase. Additionally, this experiment was performed in a copper room lined with mu-metal in order to screen out magnetic fields from the surrounding environment.

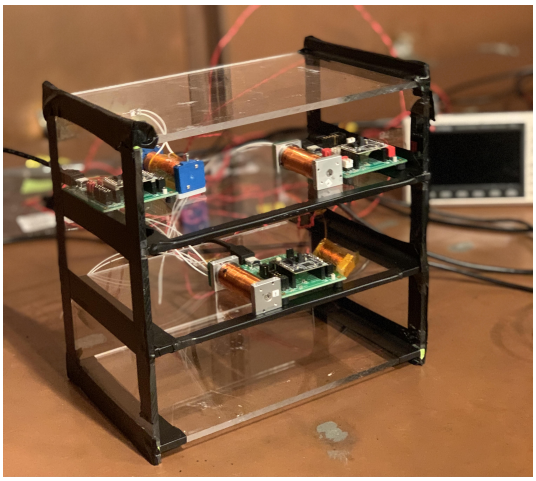

Figure 2.9: Mock CubeSat Apparatus with three PNI RM3100 magnetometers and four copper coils driven by signal generators. The magnetometers are placed within the mock CubeSat. In this study, we do not examine the effect of surface mounted sensors or sensors placed on a boom. The Apparatus is placed inside a mu-metal lined copper room that acts as a large magnetic shield can.

The PNI RM3100 is a magneto-inductive magnetometer that measures the magnetic field by counting hysteresis loops with a comparator circuit, called a Schmitt Trigger, in an ASIC. The ASIC records magnetic field measurements by adding to a register every time the Schmitt trigger is saturated. This measurement renders the magnetic field when integrated with respect to time. The ASIC has a cycle count register that controls how many clock cycles pass between integrations. The error of the magnetometer will change with respect to the cycle count. In this experiment, each magnetometer is sampled at a rate of 50 Hz with a cycle count of 200 cycles. The PNI RM3100 is rated to have a resolution of 6 nT in this configuration. The mixed signals recorded by the PNI RM3100 magnetometers are shown in Figure 2.10 below.

The proposed algorithm was run on data from the magnetometers' z-axis following the same steps as in Figure 2.5 and section 2.3.1. The signals were detrended and transformed into the Time-Frequency domain using the NSGT with a quality factor of $Q = 20$ and a lower frequency bound of 30 mHz. In step 4, low energy points were removed using a $\lambda = 2.5$. The resulting data were transformed into H(t,k) and clustered by DBSCAN with parameters $eps = 0.4$ and $MinPts = 4$.

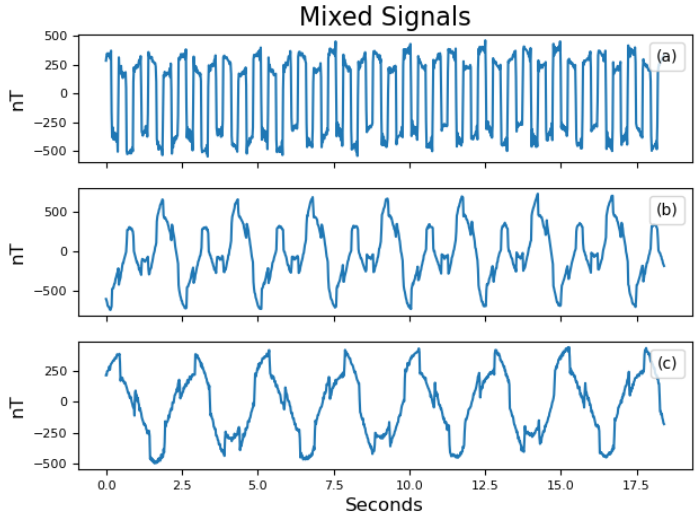

Figure 2.10: Plots (a), (b), and (c) show 18.5 seconds of three mixed signals recorded by PNI RM3100 magnetometers' z-axis. The five signals present are two sine waves, two square waves, and the added residual magnetic field data. The noise signals have amplitudes between 50 and 500 nT compared to the ambient magnetic field signal with a max amplitude near 300 nT.

DBSCAN discovered the following five clusters shown below in the columns of $\hat{K}$.

$$\hat{K} = \begin{bmatrix} 1\angle 0 & 0.023\angle 0 & 0.22\angle 0 & 0.93\angle 0 & 0.02\angle 0 \\ 1\angle 0 & 0.55\angle 1.31 & 0.97\angle 3.09 & 0.35\angle 3.04 & 0.04\angle 6.04 \\ 1\angle 0 & 0.79\angle 4.58 & 0.001\angle 2.94 & 0.15\angle 0.255 & 0.82\angle 2.84 \end{bmatrix} \tag{2.15}$$

The PNI RM3100 magnetometer was experimentally found to have a lower noise floor when sampled at a higher rate and decimated to a lower rate versus only being sampled at a lower rate. We evaluated this effect by reconstructing the original 50 Hz data in step 6, then downsampling the reconstructed ambient magnetic field signal to 10 Hz, 1 Hz, and averaging the data with a moving mean (N = 10). The magnetometer signals were downsampled by applying an 8th order Chebyshev type I anti-aliasing filter and resampling the resulting signal. The mixed signals were separated via weighted compressive sensing using a weight of $w_1 = 3$. The four noise signals reconstructed from the 50 Hz raw data are shown in Figure 2.11.

The reconstructed coil-generated signals closely resemble square and sine waves with some additional noise. The recovered residual magnetic field data are shown in the top plot of Figure

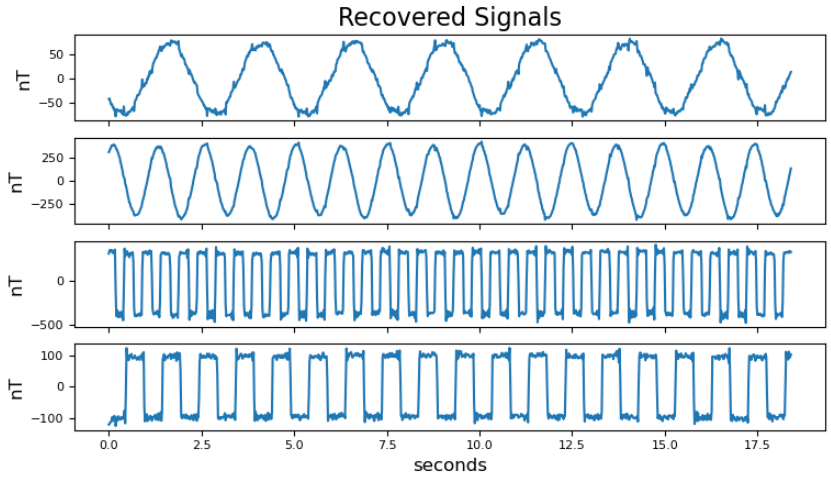

Figure 2.11: Reconstructed sine and square wave signals from 50 Hz mixed signals in Figure 2.10.

2.12. The recovered signal is overlayed with the true residual magnetic field signal. The residual data in Figure 2.12 were reconstructed using the mixed signals sampled at the full 50 Hz cadence. The plots below show the reconstructed signal, spectrograms of the noisy, cleaned, and true Swarm signal created using wavelet analysis, and a histogram of the signal reconstruction error.

The reconstructed signal closely follows the true geomagnetic perturbation signal with some high frequency noise present. As a result of the geomagnetic field signal being artificially inserted into the magnetometer readings, we are able to calculate the RMSE and Pearson Correlation Coefficient with respect to the original signal. The results for the original, decimated, and moving-mean signals are shown in Table 2.2. These results are also compared to the uncleaned magnetometer data from magnetometer (a) in Figure 2.10.

2.4 Discussion

In this study, we introduced a signal processing algorithm based on UBSS and demonstrated the separation of magnetic noise from geomagnetic field data. In the first experiment, we separated four simulated noise signals from Swarm residual magnetic field data. The noise signals contained both sparse sine wave signals and wideband sawtooth and square wave signals. The algorithm was able to restore the residual magnetic field signal with a correlation coefficient of $\rho = 0.9988$

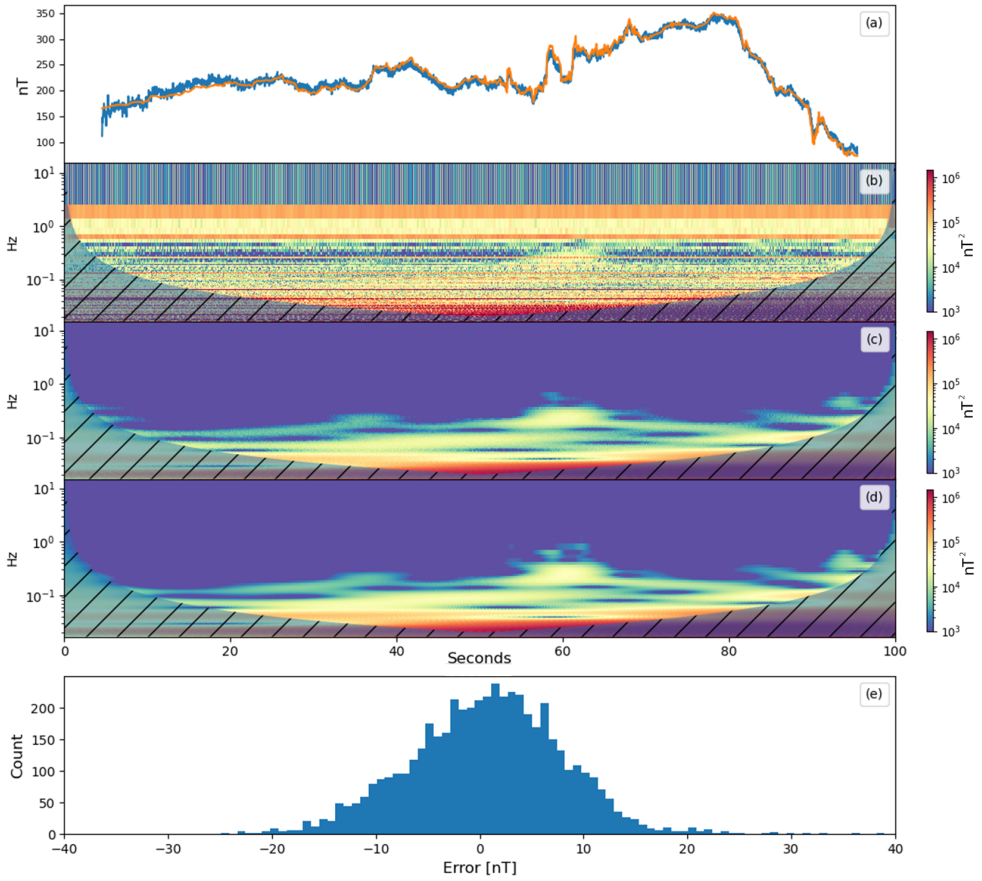

Figure 2.12: The top plot (a) shows the cleaned magnetometer signal in blue with the ambient magnetic field signal overlayed in orange. Plot (b) shows a spectrogram of the uncleaned signal from magnetometer (a) in Figure 2.10. Plot (c) shows a spectrogram of the reconstructed ambient magnetic field signal. Plot (d) shows a spectrogram of the true ambient magnetic field signal. The spectrograms were created using wavelet analysis. The shaded areas indicate where the wavelet does not produce valid results. The bottom plot (d) shows a histogram of the signal reconstruction error, $s_1 - \hat{s}_1$.

Table 2.2: Summary of Experiment 2 Results.

	Metric	50 Hz	10 Hz	1 Hz	Moving Mean (N = 10)
Recovered Signal	ρ	0.9947	0.9958	0.9952	0.9955
	RMSE	7.94 nT	7.23 nT	7.41 nT	7.45 nT
	NRMSE	2.26%	2.08%	2.13%	2.11%
Noisy Signal	ρ	0.2126	0.2286	0.9139	0.2871
	RMSE	328.08 nT	300.53 nT	30.63 nT	239.33 nT
	NRMSE	93.31%	86.69%	8.84%	68.0%

and RMSE of 2.7 nT. When the experiment was repeated without artificial instrument noise, the algorithm reconstructed the ambient magnetic field signal with a RMSE of 2.84 nT. In the second experiment, we created four magnetic noise signals using copper coils to generate real magnetic field data and placed PNI RM3100 magnetometers within the bus of a mock CubeSat apparatus. The same Swarm magnetic residual data were artificially inserted into the magnetometer measurements. This experiment mimicked the computer simulated experiment, with two sparse noise signals and two wideband noise signals. At a sampling rate of 50 Hz, the ambient magnetic field signal was reconstructed with a RMSE of 7.94 nT as opposed to 2.75 nT in simulation. The signal separation algorithm was executed using several additional preprocessing techniques such as decimating the sampling rate and applying a moving mean to the magnetometer data. A RMSE of 7.41 nT was achieved by decimating the sample rate to 1 Hz. At 1 Hz, the PNI RM3100 magnetometer is rated to have a measurement error of 2.7 nT due to instrument noise (Regoli et al., 2018b). This result places the reconstruction error near the measurement resolution of the magnetometer. When the noisy magnetometer data were decimated, it reduced the RMSE of the signal measured by magnetometer (a) in Figure 2.10 from 328.1 nT to 30.6 nT. In contrast, the decimation of the ambient magnetic field signal reconstructed from the proposed algorithm did not significantly im-

prove the RMSE. The reconstructed signal decimated to 1 Hz had an RMSE of 7.41 nT compared to 7.94 nT at 50 Hz, however, the UBSS algorithm was able to improve the RMSE by over 20 nT compared to simple downsampling. These results show that the proposed UBSS algorithm is effective at removing spacecraft noise from magnetic field data.

In general, it is not feasible to adaptively cancel spacecraft noise when a single magnetometer is used. Adaptive noise cancellation requires the removal of noise signals that are time variable. The use of a single magnetometer requires that spacecraft noise be carefully characterized before launch. Otherwise, a change in spacecraft behavior may require special maneuvers to re-characterize noise signatures in situ (Miles et al., 2019). The use of multiple magnetometers allows for the discovery of noise signals through the comparison of magnetometer data. Sheinker and Moldwin (2016), Deshmukh et al. (2020), and Imajo et al. (2021) each propose algorithms for noise cancellation using multiple magnetometers. The algorithm proposed by Sheinker and Moldwin (2016) is effective at removing a single noise signal, but is not designed for multiple noise signals. Imajo et al. (2021) propose the use of ICA which is also limited by how many noise signals it can remove. BSS algorithms require that the number of source signals be less than or equal to the number of mixed signals. Spacecraft contain many electrical systems that could generate magnetic interference, so this condition is rarely met. For example, Pope et al. (2011) identified seven common types of noise signals on Venus Express, which is equipped with two magnetometers. The advantage of the proposed UBSS algorithm over Imajo et al. (2021) and Sheinker and Moldwin (2016) is that it can cancel noise signals in an underdetermined system. This means that there are more noise signals present than magnetometers. This property of the algorithm provides the flexibility necessary to be applied to many different spacecraft without prior characterization of spacecraft noise. The algorithm also does not require knowledge of magnetometer location and orientation, except that the axis of each magnetometer are aligned. Finally, Deshmukh et al. (2020) designed a state estimation algorithm to transform housekeeping data to magnetic noise signals. Housekeeping currents provide an incomplete mapping of the distribution of currents within a spacecraft. Additionally, housekeeping data are often sampled at a low cadence and may not

have the appropriate bandwidth to identify higher frequency noise. The advantage of the proposed UBSS algorithm over this approach is that it is a blind signal processing algorithm. It requires no housekeeping data to identify and remove noise signals.

The proposed algorithm functions on the assumption that the noise signals are sparse, meaning that only one noise signal is present at a given frequency. Multiple noise signals may be active at the same time, however, if a signal is not sparse in the frequency domain, then its mixing vector cannot be accurately estimated by cluster analysis. Compressive sensing also requires sparsity in order to accurately reconstruct the separate signals. Compressive sensing can fully reconstruct sparse signals, and approximately reconstruct near sparse signals. In this work, we do not exhaustively explore the minimum sparsity required for accurate reconstruction of the ambient magnetic field. Additionally, both the signal identification and separation stages rely on the time-frequency representation of magnetometer measurements. To ensure valid results, evenly sampled signals without missing samples are required, as well as a window length that can resolve the lowest-frequency interference signal.

The proposed algorithm requires that several parameters be set by the user. In this study, the parameters were manually selected based on the signals being analyzed, but this process could also be automated. The first parameter is the quality factor, Q. This parameter adjusts the window size used in the Non-Stationary Gabor Transform. We experimentally selected it, but it may be chosen based on the length of the signal being processed. The parameter, λ, is used to remove low energy noise signals. Data points that are below a fraction, λ, of the average energy data point are removed before clustering occurs. We selected this parameter by analyzing the data projected onto the half-unit hypersphere in Figure 2.3, and visually observing if the signals were clusterable. If λ is too small, then the hypersphere will be completely filled with data points, and the noise signals will not be separable. If λ is too large, then small noise signals may not appear at all. Lastly, DBSCAN requires that two parameters, *eps*, and *MinPts*, be selected. The parameter, *eps*, represents the maximum distance allowed for two data points to be considered neighbors. The parameter, *MinPts*, represents the number of neighbors required for a data point to be considered a core. *MinPts* may

be selected based on the length of signal being processed. A disadvantage of using NSGT and DBSCAN together is that more data points are created for higher frequency signals because the window size is altered based on frequency. Therefore, *MinPts* should be selected based on the lower frequency signals.

Most heliophysics missions require magnetic field accuracies of better than 1 nT (e.g., the NASA MMS mission [Russell et al. (2016)]). Using the PNI RM3100 magnetometer, the algorithm reconstructed the ambient magnetic field signal with an RMSE of 7.94 nT. This error is near the expected measurement noise for the PNI RM3100 magnetometer at 50 Hz, indicating that the accuracy of the algorithm is limited to the total error budget of the magnetometer. Nevertheless, the experiments performed show the successful reconstruction of magnetic perturbation signals measured from within the bus of a mock CubeSat. These results demonstrate the utility of boomless CubeSats for scientific investigation of magnetic field phenomena in the geospace environment. In turn, the low cost of CubeSats enables the use of large constellations of small satellites to measure the geomagnetic field with high temporal and spatial resolution.

2.5 Conclusions and Future Work

In this study, we propose an algorithm for separating spacecraft generated magnetic noise from geomagnetic field data using multiple magnetometers. The algorithm does not require knowledge of the characteristics (location, orientation, amplitude, or spectral signature) and allows the number of noise sources to exceed the number of magnetometers ($n > m$). The algorithm identifies signals by looking at the relative gain and phase of the magnetometer data in the Time-Frequency domain. If a noise signal is sparse in this domain, the relative gain and phase is found using cluster analysis. Following the same assumption of sparsity, the signal can be separated from the noisy data using the cluster centroids in compressive sensing.

The algorithm is designed for underdetermined systems in which there are more noise sources than magnetometers. An advantage of this approach is that the UBSS algorithm can be integrated

onto any satellite since no prior characterization of noise signals is required. This design eases the assimilation of magnetometers into spacecraft designs by reducing the need for strict magnetic cleanliness requirements and long mechanical booms.

There are several avenues of future development for this algorithm. The most immediate step to be taken is for the selection of parameters to be automated. We present an algorithm to automate the noise cancellation process, but some rudimentary analysis is still required to select parameters for clustering and pre-processing. We think the selection of parameters could be entirely automated. Another avenue of development is to test the limits of the sparsity assumption. Sparsity is a very strict assumption that may not always be met. In this work, we tested the algorithm using several wideband signals. However, the threshold for minimum sparsity is unknown. This assumption can be examined through examining signals with partially overlapping spectra to find a point of failure. Finally, an interesting scenario to investigate is where several magnetometers are mounted within the bus of a spacecraft, but one magnetometer is mounted on a short boom, such as on the spacecraft Dellingr (Kepko et al., 2017). In this scenario, the measurements of one magnetometer may be more accurate than the others. It would be counterproductive if the reconstructed magnetometer signal had more noise than the signal measured by the magnetometer on the boom. It may be possible to account for this by designing a programmable "trust" parameter at the compressive sensing stage. This parameter would indicate an elevated degree of trust in one magnetometer over the others.

In this work, we performed two experiments to validate the algorithm. The first experiment separated Swarm magnetic perturbation data from four computer simulated signals. The algorithm was able to reconstruct the ambient magnetic field signal with an RMSE near 3 nT and a correlation of $\rho \approx 0.9988$. The reconstruction errors are less than the 6 nT intrinsic instrument noise that was added to each virtual magnetometer. The second experiment used real magnetic noise signals generated by copper coils, and the same Swarm geomagnetic field data. This experiment was able to separate four noise signals and reconstruct the background magnetic perturbation signal with a RMSE of 7.23 nT and a correlation of $\rho = 0.9958$ at a 10 Hz cadence.

These results show the potential of signal processing algorithms to identify and remove magnetic noise from spaceborne magnetometer data. The proposed algorithm diminishes the need to place a magnetometer on a boom or enables significantly shorter booms. This enables the possibility of low cost, boomless spacecraft to capture high fidelity magnetic field measurements.

CHAPTER 3

Enabling Boomless CubeSat Magnetic Field Measurements with the Quad-Mag Magnetometer and an Improved Underdetermined Blind Source Separation Algorithm

In this chapter, we continue the investigation of stray magnetic field noise removal with two additional paths of development. In order to circumvent the conventional issues with spacecraft magnetometers, we introduce the Quad-Mag CubeSat magnetometer, combined with an improved Underdetermined Blind Source Separation (UBSS) removal algorithm. The Quad-Mag, equipped with four magnetometer sensors on a single printed circuit board, enables distributed field measurements in a compact CubeSat form-factor. The refined UBSS algorithm, featuring single-source point detection and iteratively-weighted compressive sensing, accurately distinguishes noise from ambient magnetic fields. Our lab experiments with a mock CubeSat and simulations for various CubeSat sizes demonstrate the effectiveness of this integrated system in reducing magnetic noise, affirming its suitability for high-fidelity magnetic field measurements in small satellite platforms.

The research and results from this chapter have been published in the Journal of Geophysical Research: Space Physics and can be found at https://agupubs.onlinelibrary.wiley.com/doi/full/10.1029/2023JA031662. For detailed data and additional insights, please refer to the University of Michigan Deep Blue data repository at https://doi.org/10.7302/rtr3-rs48.

3.1 Introduction

In situ magnetic field measurements are crucial for unraveling the dynamics of space plasmas and understanding the complex interactions within the near-Earth environment. These observations enable detailed studies of various magnetospheric currents, such as field-aligned currents (FACs) and magnetopause currents, which are pivotal for understanding the coupling between the magnetosphere and ionosphere (Slavin et al., 2008). Despite their importance, accurate ambient magnetic field measurements face significant challenges. These challenges stem from stray magnetic fields emanating from spacecraft subsystems, including solar panels, magnetorquers, and propulsion systems. Stray fields, such as the 20 nT noise signal from the GOES-16 spacecraft's arcjet thrusters, can severely compromise the integrity of magnetic field data, posing a significant hurdle for space physics research (Califf et al., 2020). Stringent magnetic cleanliness protocols and the use of deployable booms to distance magnetometers from the source of the noise are commonly used to mitigate spacecraft interference. However, these methods come with their own set of challenges, as exemplified by missions like the Defense Meteorological Satellite Program (DMSP), which still encounters interference despite employing a 5-meter boom (Kilcommons et al., 2017). The limitations of booms, especially in terms of design complexity and cost, underscore the need for innovative solutions in spacecraft design and magnetometer technology to ensure the fidelity of magnetic field measurements in space exploration missions.

The use of multiple magnetometers on a spacecraft enables the application of noise removal algorithms to separate stray magnetic fields from the ambient magnetic field. Several gradiometry algorithms have been developed which model the spacecraft noise as a magnetic dipole and use a pair of magnetometers to remove the estimated noise (Ness et al., 1971; Carter et al., 2016; Ream et al., 2021; Constantinescu et al., 2020). Carter et al. (2016) found that gradiometry underperforms when the stray magnetic field noise is less than twice the intrinsic magnetometer noise, and developed an algorithm to switch between using gradiometry or averaging. Ream et al. (2021) developed a gradiometry algorithm that detects stray magnetic field signals through differencing the magnetometer measurements in the time-domain and suppressing them in the frequency-domain. Con-

stantinescu et al. (2020) developed the algorithm, Principal Component Gradiometry (PiCoG), that transforms the dual-magnetometer measurements into a new coordinate system derived from principle component analysis, and performs gradiometry along the direction of maximum-variance. These algorithms perform well, however, they still require the use of a mechanical boom.

Several recent algorithms have been developed that may not require the use of a boom. Sheinker and Moldwin (2016) developed an analytical blind source separation method to remove a single noise source using a pair of magnetometers. Imajo et al. (2021) apply Independent Component Analysis to separate noise signal based on their statistical independence, however this method can only separate a limited number of noise signals. Finley et al. (2023) applied multivariate singular spectrum analysis to separate out signal components in the time domain. This method has minimal assumptions about signals present, but picking the correct components to reconstitute the natural magnetic field signal is tricky and prone to error.

As the use of CubeSats for space physics research are rising in popularity, a magnetometer package that fits the stringent size, mass, power and volume requirements of a CubeSat combined with a noise removal algorithm suited for the complex spacecraft magnetic field environment becomes necessary. We propose the use of the Quad-Mag magnetometer board and a noise removal technique called UBSS to remove stray magnetic field noise from CubeSat magnetometer measurements (Strabel et al., 2022; Hoffmann and Moldwin, 2022). The Quad-Mag is a compact multi-magnetometer board that uses low-power magneto-inductive magnetometers to take distributed magnetic field measurements with a resolution near 1 nT at 1 Hz (Leuzinger and Taylor, 2010; Regoli et al., 2018b; Strabel et al., 2022). In complement, the UBSS algorithm exploits the multi-magnetometer configuration to discern and isolate stray magnetic field noise generated from spacecraft subsystems. This algorithm implements a two-step process that first identifies the noise signals through cluster analysis, and subsequently separates the stray magnetic field signals from the ambient magnetic field using compressive sensing. Hoffmann and Moldwin (2022) demonstrated the removal of four noise signals from lab-generated magnetometer data and reduced the root mean squared error (RMSE) of magnetometer measurements from 300.53 nT to 7.23 nT

(near the sensor resolution at 50 Hz). The UBSS algorithm can remove stray magnetic field noise without prior knowledge of the magnitude, orientation, or number of noise sources. This novel approach allows us to obtain high-fidelity magnetic field measurements with a greater degree of accuracy and precision.

In this work, we present two experiments demonstrating the Quad-Mag and UBSS system. The first experiment demonstrates the separation of four copper coil-generated noise signals from Swarm magnetometer data using a mock CubeSat (Merayo et al., 2008). The second experiment simulates the removal of noise measured by the Quad-Mag in 1U, 2U, 3U, and 6U CubeSats. We also present several enhancements to the noise removal algorithm by Hoffmann and Moldwin (2022), detailed in the methodology section. The successful application of the Quad-Mag magnetometer with UBSS would enable high-fidelity magnetic field measurements to be measured from a CubeSat without the need for a boom. This solution not only improves the accuracy of magnetic field measurements, but it also significantly reduces the cost and complexity of spacecraft designed to measure the magnetic fields of space plasma.

3.2 Methodology

The Quad-Mag is a low size, weight, power, and cost (SWAP-C) magnetometer that enables high-fidelity magnetic field measurements and fits the form factor of a CubeSat. The UBSS algorithm, designed by Hoffmann and Moldwin (2022), allows for the use of the Quad-Mag in the noisy CubeSat environment expected for a magnetometer mounted inside the CubeSat bus. In this section, we provide a brief overview of the specifications of the Quad-Mag designed by Strabel et al. (2022), and the UBSS algorithm designed by Hoffmann and Moldwin (2022). We also describe several improvements made to the UBSS algorithm through the implementation of single source point detection, changing the clustering algorithm, and introducing an iterative weighting scheme to the compressive sensing algorithm in signal reconstruction.

3.2.1 The Quad-Mag Techniques and Specifications

The Quad-Mag is a 10 cm x 10 cm standard CubeSat form factor board composed of four PNI RM3100 magnetometers. The PNI RM3100 magnetometers are controlled by a single microcontroller, enabling synchronized communication with the CubeSat and all four magnetometers. The PNI RM3100 is a commercial magnetometer but has been proven to be spaceflight-ready and radiation-tolerant (Moldwin et al., 2022; Regoli et al., 2020). Regoli et al. (2018b) characterized the PNI RM3100 and observed a measurement uncertainty of 8.7 nT at 40 Hz, 2.7 nT at 1 Hz, and a linear dynamic range of ±100,000 nT. We tested several PNI RM3100 magnetometers at the University of Michigan's Magnetic Laboratory and found the measurement uncertainty of individual sensors to be between 1.5 and 2.5 nT at 1 Hz.

The use of four PNI RM3100 magnetometers on the Quad-Mag board has multiple purposes. First, the Quad-Mag is able to achieve a lower measurement uncertainty than a single magnetometer through averaging. The quantization error of the PNI RM3100 is inversely proportional to its sampling rate, and can also be lowered through oversampling with multiple magnetometers. According to the central limit theorem, the standard deviation of the mean of M independent measurements is inversely proportional to $\sqrt{M}$, where M is the number of magnetometers. Strabel et al. (2022) observed a measurement uncertainty of 5.34 nT when sampling the Quad-Mag at 65 Hz versus 10.59 nT when testing a single PNI RM3100. The second advantage of using four magnetometers is that multiple points of measurement enable the use of noise removal algorithms such as UBSS. This paper demonstrates that the short distance separation of the four magnetometers on the Quad-Mag is sufficient to identify multiple noise sources within a CubeSat.

3.2.2 System Model and Signal Identification

The role of UBSS in magnetic noise removal is to separate the spacecraft-generated noise from the ambient magnetic field if there are more noise sources than magnetometers (Hoffmann and Moldwin, 2022). UBSS is a blind algorithm which means that it does not require any prior knowledge of the magnitude, spectral content, location, or orientation of the noise sources. However,

in spacecraft magnetometry we assume that the ambient magnetic field appears equally at each magnetometer. At the time-frequency bin, (t, k), the presence of the source signals, $S(t, k)$, at each magnetometer, $B(t, k)$, is defined by the mixing system, $B(t, k) = KS(t, k)$, where K is the mixing matrix and its columns are known as the mixing vectors. This system is expressed in its full matrix format in equation (3.1).

$$\begin{bmatrix} B_1(t,k) \\ B_2(t,k) \\ \vdots \\ B_m(t,k) \end{bmatrix} = \begin{bmatrix} 1 & k_{12} & k_{13} & ... & k_{1n} \\ 1 & k_{22} & k_{23} & ... & k_{2n} \\ \vdots & \vdots & \vdots & \ddots & \vdots \\ 1 & k_{m2} & k_{m3} & ... & k_{mn} \end{bmatrix} \begin{bmatrix} S_1(t,k) \\ S_2(t,k) \\ \vdots \\ S_n(t,k) \end{bmatrix} \tag{3.1}$$

In this system, we seek to recover the ambient magnetic field signal, $S_1(t, k)$, which is associated with the column of ones in the mixing matrix, K. In the case that there are more noise signals than magnetometers, this is an underdetermined system and ordinary signal demixing algorithms can not be applied. The first step identifies the source signals by finding their corresponding mixing vectors in K using cluster analysis. The second step separates the ambient magnetic field signal by applying compressive sensing techniques.

Both the signal identification and signal separation steps rely on the sparsity assumption that only one signal is active in a time-frequency bin (t,k). If $S_j(t, k)$ is the only active signal at time-frequency, (t, k), and all other signals are zero, then the system in equation (3.1) can be simplified to a single mixing vector.

$$\begin{bmatrix} B_1(t,k) \\ B_2(t,k) \\ \vdots \\ B_m(t,k) \end{bmatrix} = \begin{bmatrix} k_{1j} \\ k_{2j} \\ \vdots \\ k_{mj} \end{bmatrix} S_j(t,k) \tag{3.2}$$

The reduced system in equation (3.2) defines a straight line with a slope proportional to the mixing vector, K_j. When the mixed magnetometer signals, $B(t, k)$ are compared against each

other, each sparse source signal will correspondingly align along a unique line, guided by their respective mixing vectors. This property of the system allows for the discovery of each mixing vector needed to reconstruct the full mixing matrix. In this work, we follow the same steps as Hoffmann and Moldwin (2022) used to transform the data into a clusterable format with a few additional updates. The completely transformed magnetometer data are referred to as $H(t, k)$.

The magnetometer measurements, $b(t)$, contain both intrinsic measurement noise and multi-source points (MSP) where the time-frequency distributions of different source signals overlap. The MSPs interfere with the identification of the source signals. Before transforming the data into a clusterable format, we transform the time-series data, b(t), into the time-frequency domain, B(t, k), using the NSGT transform in order to improve sparsity (Holighaus et al., 2013). We then apply a magnitude filter and a single-source point (SSP) filter to remove the intrinsic noise and MSPs.

The measurement uncertainty of the PNI RM3100 magnetometer at 1 Hz is near 2.7 nT. As a result, time-frequency bins with low energy may project randomly onto the unit hypersphere (Sun et al., 2016). We cleanse these low energy data points using a magnitude filter which removes data points below a factor of the magnetometer's measurement uncertainty. This filter is defined in equation (3.3).

$$|B(t, k)| > \lambda \cdot \sigma \tag{3.3}$$

The parameter, σ, defines the standard deviation of the characterized measurement uncertainty of the magnetometer. The parameter, λ, is the factor that defines the magnitude at which low energy points should be removed with respect to the measurement uncertainty, σ. Only statistically meaningful data points will remain after the magnitude filter has been applied.

To identify and remove MSPs, we use a SSP detection algorithm that compares the complex and real components of the mixed magnetometer signals, $B(t, k)$. If only one source signal, $S_j(t, k)$, contributes to a time-frequency bin, (t, k), then both the real and imaginary components of $B(t, k)$ will be proportional to the same mixing vector, K_j. This means that their cosine similarity will be equal to 1. We calculate the cosine similarity using equation (3.4) and remove data points that are

above a certain threshold, θ_0 (Reju et al., 2009).

$$\theta = cos^{-1}(\frac{\{Re[B(t,k)]\}^T Im[B(t,k)]}{\sqrt{\{Re[B(t,k)]\}^T Re(B(t,k))}\sqrt{\{Im[B(t,k)]\}^T Im(B(t,k))}}) \tag{3.4}$$

Once the original magnetometer data, $b(t)$, has been filtered and transformed into a clusterable format $H(t,k)$, a number of clustering algorithms can be used to reconstruct the mixing matrix, K. Hoffmann and Moldwin (2022) use the Density Based Spatial Clustering for Applications with Noise (DBSCAN) algorithm (Ester et al., 1996). This algorithm requires two data-dependent parameters, *eps* and *minPts*, that must be set by the user. In this work, we use the Hierarchical Density Based Spatial Clustering for Applications with Noise (HDBSCAN) algorithm because it has similar benefits to DBSCAN but does not require the user to set any parameters (McInnes and Healy, 2017; Campello et al., 2013). HDBSCAN is an extension of DBSCAN that uses a hierarchical clustering scheme. Similar to DBSCAN, HDBSCAN does not require the number of clusters to be defined beforehand, and it will ignore noisy data points. We use HDBSCAN to cluster H(t,k) and use each cluster's centroid as a source signal mixing vector. We then join these vectors to form the mixing matrix, K, which we use to separate the source signals from ambient magnetic field via compressive sensing.

3.2.3 Source Signal Separation

To separate the stray magnetic field signals from the ambient magnetic field, we first estimate the mixing matrix, K, using HDBSCAN. Then, we use compressive sensing (CS) to reconstruct the ambient magnetic field signal from the mixed signals. CS is an algorithm that can recover sparse or near-sparse signals from under-sampled measurements (Baraniuk, 2007). It is widely used in audio and image decompression applications. Hoffmann and Moldwin (2022) apply a weighted Basis Pursuit scheme for CS, which solves the following optimization problem in equation (3.5) (Candès et al., 2008).

$$\begin{aligned} &\text{Minimize} \quad w^T|s| \\ &\text{Subject to} \quad b = Ks \end{aligned} \tag{3.5}$$

However, this scheme assumes that there is no measurement error in b. If the measured signals are very noisy, this assumption may not hold. Therefore, we propose a different scheme based on the Dantzig Selector with an iterative weighting scheme (Candes and Tao, 2007). The Dantzig Selector uses the L-infinity norm to measure the error in the residual vector, which makes it more robust to outliers and noise than the least squares method. It also selects fewer source signals to explain the data, which enhances the sparsity of the solution (Rani et al., 2018). The formulation of the Dantzig Selector is shown in equation (3.6).

$$\begin{aligned} &\text{Minimize} \quad w^T|s| \\ &\text{Subject to} \quad \|K^T(b - Ks)\|_\infty \leq \eta \end{aligned} \tag{3.6}$$

The parameter, η, in the problem constraint is a tuning parameter that controls how much error is allowed. This formulation enables us to recover the ambient magnetic field signal even when there is some measurement error, e, in the underdetermined measurement system $b = Ks + e$.

We use a weighting scheme to reduce noise and error in the signal reconstruction process. The weighting scheme assigns different importance to different elements in the solution vector, s, which represents the separated signals. The first element of s, denoted by s_1, corresponds to the ambient magnetic field signal, which is our main interest. The other elements correspond to the stray magnetic field signals, which are considered as noise. Hoffmann and Moldwin (2022) use a constant weighting vector that gives more weight to s_1 than to other elements of s. However, this may not be optimal for different types of mixed signals. Therefore, we propose an adaptive weighting scheme that adjusts the weight of s_1 based on whether the mixed time-frequency signal, B(t,k), is a SSP or a MSP. A SSP means that only one source signal contributes to B(t,k), while an MSP means that multiple source signals contribute to B(t,k). If B(t,k) is a SSP, we use the Candès et al. (2008) weighting scheme where $w = \dfrac{1}{|s|}$, which assigns less weight to larger elements of s

to induce sparsity. If B(t,k) is an MSP, we iteratively increase the weight of s_1 using the formula $w_1 = w_1 + \alpha(s_{ratio} - w_1)$, where α is a learning rate, w_1 is the first element of w corresponding to s_1, and s_{ratio} is the ratio of the sum of absolute values of noise signals to the absolute value of ambient magnetic field signal. The variable, s_{ratio}, is defined in the following equation where s is the solution vector and ϵ is a small constant to prevent division by zero.

$$s_{ratio} = \frac{\sum_{i=2}^{n} |s_i|}{|s_1| + \epsilon} \tag{3.7}$$

This scheme aims to enhance the sparsity of s by suppressing noise signals and highlighting the ambient magnetic field signal. We use this adaptive weighting scheme with Dantzig Selector, which is a compressive sensing constraint that can handle measurement errors. This system allows us to reconstruct the ambient magnetic field with as little noise as possible from under-sampled measurements.

We use CVXPY, a Python-embedded modeling language for convex optimization problems (Diamond and Boyd, 2016), to solve the system defined by equation (3.6). CVXPY automatically transforms the problem into standard form, calls a solver, and unpacks the results. The solver we use is Embedded Conic Solver (ECOS), which converts the problem into a Second Order Cone Problem (SOCP) and applies an interior point solver to find the sparse solution (Alizadeh and Goldfarb, 2003; Domahidi et al., 2013).

The final step of our method is to apply a Savitzky-Golay (SG) filter to the reconstructed ambient magnetic field signal. The SG filter is a smoothing technique that preserves the shape and features of the signal while reducing random normal noise. It works by fitting a polynomial of a given order to a sliding window of data points using least squares. The filtered value at each point is obtained by evaluating the fitted polynomial at the center of the window. Liu et al. (2016) used a SG filter to denoise seismological measurements. In our case, we use a SG filter to enhance the quality of the ambient magnetic field signal after separating the noise through compressive sensing. The window size and degree of the polynomial in the SG filter can be used to adjust the degree of smoothing applied to the signal. The use of the SG filter is an optional addition to the UBSS algo-

rithm and may or may not be used depending on the configuration of the magnetometers and use of the magnetic field measurements. Moreover, the SG filter is applied only to the ambient magnetic field signal, and its use results in some information loss from the original mixed magnetometer measurements.

3.3 Experimental Data and Results

In this paper, we present two experiments that show the effectiveness of our integrated Quad-Mag and UBSS system for removing stray magnetic fields. The first experiment uses a Mock CubeSat designed by Deshmukh et al. (2020) with four copper coils driven by waveform generators to create artificial noise signals. We also add geomagnetic perturbation data from the Swarm A satellite to simulate the ambient magnetic field (Merayo et al., 2008). The second experiment is a simulation that applies our system to different sizes of CubeSats (1U, 2U, 3U, and 6U). We use the same Swarm data and four noise signals for each simulation. The results demonstrate that our system can successfully remove the stray magnetic fields from these CubeSat configurations.

Figure 3.1 illustrates the signal processing procedures detailed in sections 3.2.2-3.2.3. The first step (i) is to transform the mixed magnetometer signals, b(t), into the time-frequency domain, B(t,k), using the NSGT to improve signal sparsity. The second step (ii) is to remove the low magnitude time-frequency points using the magnitude filter described in equation (3.3). The third step (iii) is to identify the remaining data points as SSPs or MSPs based on equation (3.4). The fourth step (iv) is to prepare the data for cluster analysis by transforming it into a clusterable form. The clusterable data, H(t,k), is then used to find the mixing matrix, K, in the fifth step (v) through the use of HDBSCAN. The sixth step (vi) is to separate the original time-frequency data, B(t,k), through the iteratively weighted compressive sensing scheme detailed in section 3.2.3. In the last and seventh step (vii), the SG filter is applied in order to reduce the random normal noise of the reconstructed signal.

We use three metrics to evaluate how well our algorithm reconstructs the ambient magnetic field

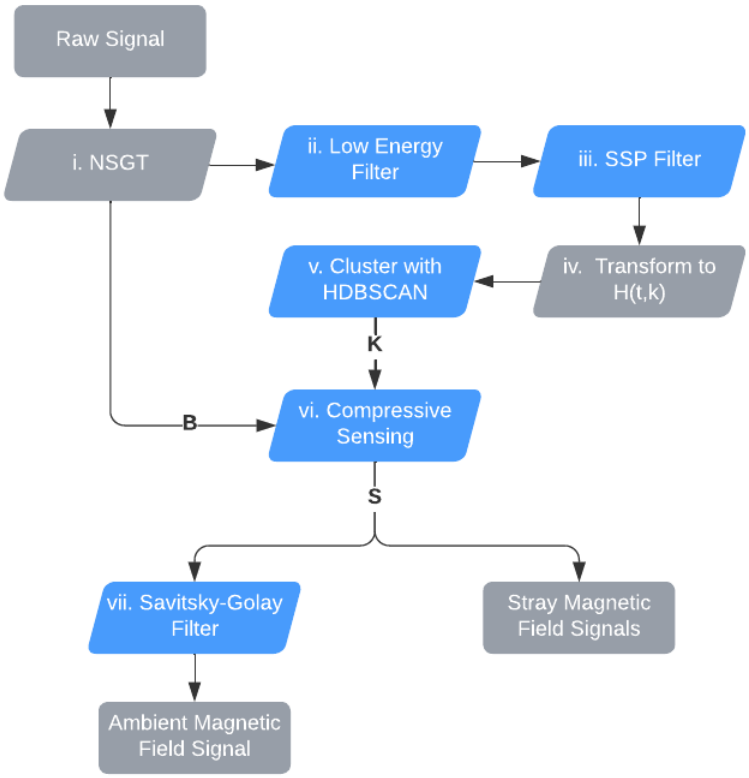

Figure 3.1: Block diagram of the processes involved in recovering the mixing matrix, **K**, through cluster analysis and reconstructing the ambient magnetic field signal, s_1, through compressed sensing. The steps shown in blue are new contributions or modifications to the Hoffmann and Moldwin (2022) method. In step two (ii), the low energy filter uses a threshold based on the instrinsic noise of the instrument. The SSP filter in step three (iii) is a new addition. Step five (v) uses HDBSCAN instead of DBSCAN to reduce the amount of parameters in the overall algorithm. Step six (vi) is modified to use the Dantzig Selector and an iterative weighting scheme. Lastly, step seven (vii) is a new addition to the algorithm.

signal from the noisy measurements: Signal to Noise Ratio (SNR), Pearson Correlation Coefficient (ρ), and Root Mean Squared Error (RMSE). These metrics compare the reconstructed signal, x, with the true signal, y, element-wise over the entire time-series. The Pearson Correlation Coefficient, given by equation (3.8), measures how linearly related the normalized input and recovered signals are.

$$\rho = \frac{\sum_{i=1}^{N}(x_i - \bar{x})(y_i - \bar{y})}{\sqrt{\sum_{i=1}^{N}|(x_i - \bar{x})|^2 \sum_{i=1}^{N}|(y_i - \bar{y})|^2}} \tag{3.8}$$

The RMSE, given by equation (3.9), measures the average magnitude of error between the estimated and true signals. This metric is sensitive to large outliers, so a few large deviations may inflate its value. The RMSE does not indicate what an acceptable level of error is, so we also use the SNR.

$$RMSE = \sqrt{\frac{\sum_{i=1}^{N}(x_i - y_i)^2}{N}} \tag{3.9}$$

The SNR, measured in decibels, defines the ratio of power from the ambient magnetic field signal to power from noise from stray magnetic field signals. This metric helps to give context to the RMSE value. The SNR is given by equation (3.10).

$$SNR = 10\log_{10}\frac{\sum_{i=1}^{n}(x_i - \bar{x})^2}{\sum_{i=1}^{n}(x_i - y_i)^2} \tag{3.10}$$

3.3.1 Experiment 1: Mock CubeSat Noise Removal

In this experiment, we demonstrate the utility of the proposed algorithm on real magnetic field data. To take measurements of the copper coil-generated noise signals, we used a prototype of the Quad-Mag magnetometer. The copper coils were driven by signal generators to create the source signals, $s(t) \supset [s_2(t), s_3(t), s_4(t), s_5(t)]$. The waveforms driving the stray magnetic field signals were a 5 Hz sine wave, 2 Hz sawtooth wave, 0.8 Hz sine wave, and a 3 Hz attenuating sine wave. The spectral content of these noise signals provided a variety of sparse and wideband signals to test against. The Quad-Mag sampled 150 seconds of the coil-generated signals at 65 Hz. A single PNI RM3100 magnetometer has an estimated measurement uncertainty of near 10.5 nT at 65 Hz. The averaged Quad-Mag measurements are estimated to have a factor of 2 reduction in measurement uncertainty, near 5.25 nT. The experimental apparatus is shown in Figure 3.2.

The source signals were combined in the mixing system, $b(t) = Ks(t) =$

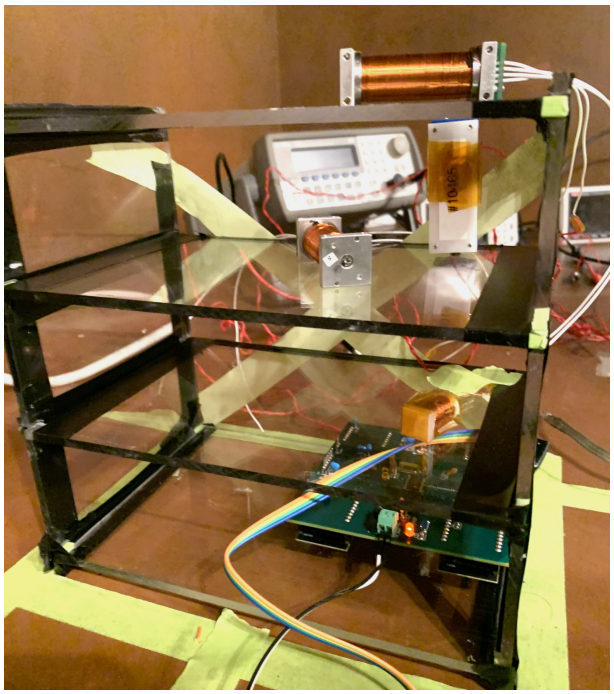

Figure 3.2: The Quad-Mag and copper coils are placed within a 6U mock CubeSat, with all components occupying a 3U volume (10 x 10 x 30 cm) to emulate a 3U CubeSat configuration. The Quad-Mag is positioned at the bottom of the CubeSat, while the four noise coils are arranged vertically above it, all within a 10 x 10 cm^2 area. The mock CubeSat is situated in a copper room lined with mu-metal for magnetic shielding. This room serves as a large magnetic shield.

$[b_1(t), b_2(t), b_3(t), b_4(t)]$. The signal, $s_1(t)$, was residual geomagnetic field data that was generated by subtracting the International Geomagnetic Reference Field (IGRF) model from spacecraft magnetic field data measured by the Swarm A satellite. The data were recorded on March 17th, 2015, between 8:53 and 8:55 UTC as the spacecraft passed through a perturbation in the southern auroral zone. The first twenty seconds of the mixed signals are shown in Figure 3.3.

The UBSS algorithm was applied to the Quad-Mag's z-axis following the procedure in Figure 3.1. In step one (i), the NSGT algorithm requires the user to set the lowest frequency for the transform and the bands per octave. We set the low frequency to 0.01 Hz and used 1 band per octave. These values are used to vary the window length with respect to the frequency being analyzed, and can be automated based on the magnetometer configuration. In the second step (ii), we used $\sigma = 10$ and $\lambda = 3$ to remove low-energy points. The value σ corresponds to the estimated noise at a single magnetometer of about 10.5 nT. In the third step (iii), the time-frequency points

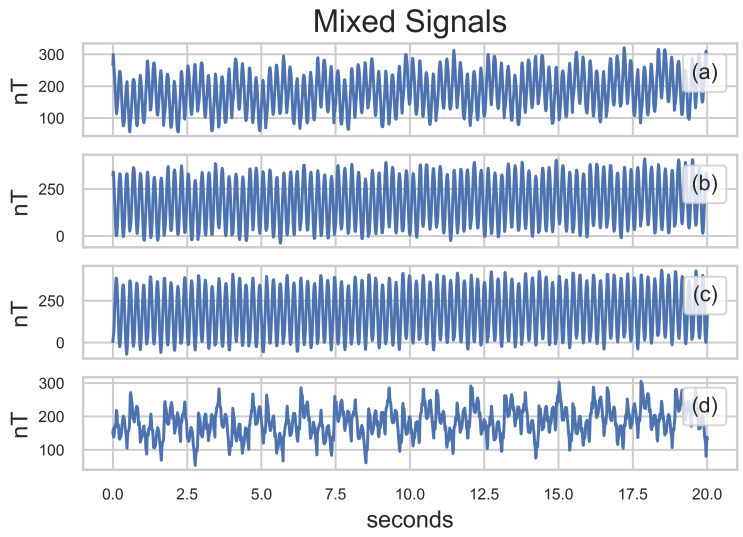

Figure 3.3: Plots (a), (b), (c), and (d) display 20 seconds of the four mixed signals recorded by the Quad-Mag's z-axis at 65 Hz. These panels show the mixed signals observed at each of the four magnetometers on the Quad-Mag. The four noise signals consist of a 5 Hz sine wave, a 2 Hz sawtooth wave, a 0.8 Hz sine wave, and a 3 Hz attenuating sine wave. Additionally, the fifth source signal is the ambient magnetic field signal, which is virtually added to each magnetometer signal. The noise signals exhibit amplitudes ranging from 50 nT to 200 nT. The coil-generated source signals appear differently at each magnetometer due to the relative location of the magnetometers to the copper coils and dipole-structure of the coil-generated magnetic field.

were classified as MSPs and removed if they had an angle above $\theta = 15°$. The next two steps of the algorithm require no user-set parameters. The noise signals were identified using cluster analysis and separated using compressive sensing. After separation, the ambient magnetic field signal is smoothed with a SG filter that uses a 33-point sliding window and a third order polynomial. The cleaned magnetic field signal and the spectra of the noisy, cleaned, and true signal are shown in Figure 3.4.

The estimated ambient magnetic field signal in Figure 3.4 closely resembles the true geomagnetic field signal. Panel (b) shows the difference between the original and recovered ambient magnetic field signals. The difference is larger between 80 and 100 seconds, and briefly at 135 seconds, in the 150-second signal. This may be due to the interference of multiple noise signals at 1 Hz. Panel (c) shows that the spectrum of the noise in the uncleaned magnetometer measurements ranges from near DC to 5 Hz. Panel (d) shows the reconstructed signal, which eliminates most

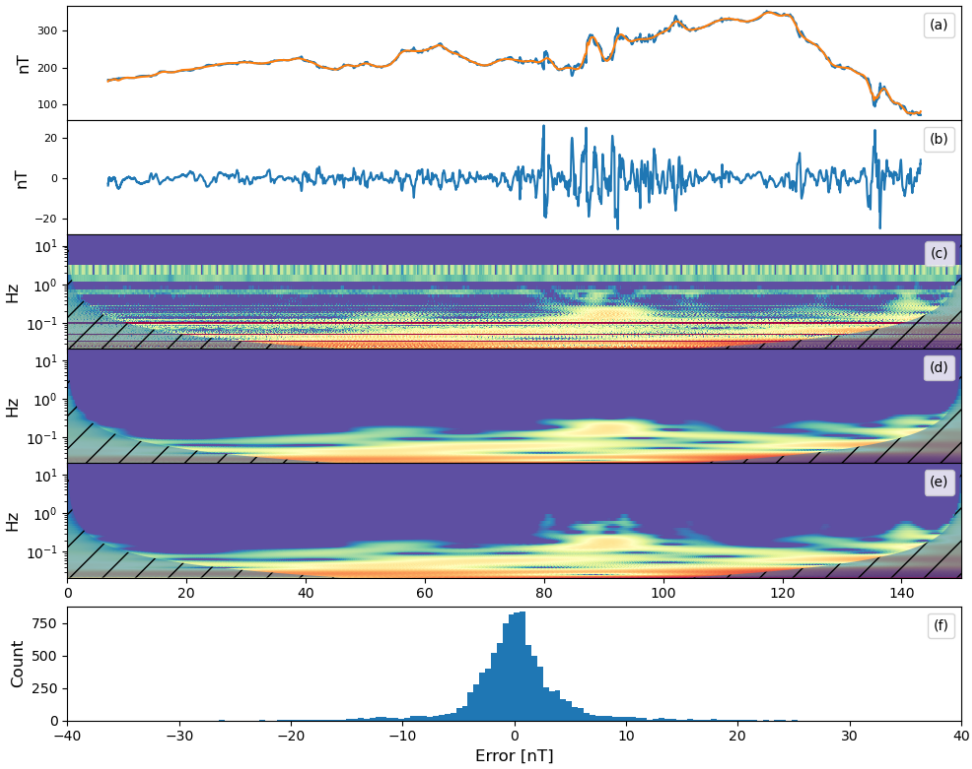

Figure 3.4: The orange line in plot (a) represents the magnetometer signal after cleaning, while the blue line shows the actual ambient magnetic field signal. Plot (b) depicts the difference between the estimated signal and the true signal. Plot (c) displays a scaleogram of the raw signal from a single magnetometer on the Quad-Mag, created using wavelet analysis. The shaded regions indicate invalid wavelet results. Plot (d) shows a scaleogram of the estimated ambient magnetic field signal, and plot (e) shows a scaleogram of the true signal. Plot (f) is a histogram of the error between the original and estimated signals, $s_1 - \hat{s}_1$.

of the noise that overlaps with the ambient magnetic field spectrum. However, the ambient signal near 1 Hz is also attenuated. This indicates that UBSS cannot separate the noise from the natural magnetic field when there are multiple noise signals with similar frequencies to the ambient magnetic field signal.

Table 3.1 shows the RMSE, SNR, and correlation of the reconstructed signal with respect to the true magnetic field signal. We compared these results to a single magnetometer on the Quad-Mag, to the average of all four magnetometers, and to the application of UBSS with and without the SG filter to demonstrate the efficacy of our algorithm and the integrated suite. In this experiment, the UBSS algorithm reduced the RMSE from 120.07 nT at a single magnetometer to 4.45 nT. This is

near the expected noise floor of the instrument. The application of the SG filter produced a small reduction in RMSE from 4.45 nT to 4.40 nT. The differences between UBSS and UBSS with the SG filter were negligible in this case, and the scalograms of both cleaned signals were identical.

Table 3.1: Summary of Experiment 1 Results.

	ρ	**SNR (dB)**	**RMSE (nT)**
Single	0.4353	-6.29	120.07
Average	0.9518	9.84	18.72
UBSS	0.9970	22.23	4.45
UBSS + SG	0.9971	22.33	4.40

3.3.2 Experiment 2: Simulated CubeSat Noise Removal

In this simulation, we investigate the performance of the UBSS algorithm in removing noise signals from magnetometer measurements for several CubeSat form factors. We use the Magpylib package to simulate a four dipole noise sources and four virtual magnetometers. The magnetometers are placed to emulate the spacing and function of the Quad-Mag. The noise sources consist of simulated reaction wheel noise signal, square wave and sine wave signals that turn on and off randomly, and real magnetometer noise from the Michibiki satellite. The Michibiki magnetometer data used are a full 24-hour measurement from April 23rd, 2012 (Imajo et al., 2021). The noise signal was generated by differencing inboard and outboard magnetometer measurements to eliminate the geomagnetic field, and resampled to fit the 100-second simulated signal duration. This process induced a frequency shift in the Michibiki noise signal, while preserving the original spectral shape, resulting in a spectrally similar signal at a higher frequency. The source signals used in this experiment are illustrated in Figure 3.5.

The Magpylib python library was used to simulate these source signals as magnetic fields. The noise sources were randomly placed within a 1U volume and scaled vertically and horizontally to simulate the 2U, 3U, and 6U CubeSats. The axes of the dipoles were aligned to minimize cancellation of the magnetic field, representing a worst-case scenario. However, in practice, if noise sources with known dipole orientation are placed in opposite directions, the magnetic fields can partially cancel at the magnetometers. Figure 3.6 shows the locations of the noise sources and virtual magnetometers in the 1U CubeSat Magpylib simulation.

The Magpylib library allows the user to specify the location of various magnetic field sources and magnetometers. The library is not able to simulate AC magnetic fields, however, we overcome this by measuring the value of each noise source at each magnetometer and forming a mixing matrix, K, from these values. The magnetometer signals are then generated by multiplying the source signals, s, by the mixing matrix, K, in the system, b(t) = Ks(t). The mixing matrix used to form the mixed signals in the 1U simulation is shown below in equation (3.11). The source signals, $s_j(t)$, correspond to the five source signals in Figure 3.5. The values in the mixing matrix, K, are

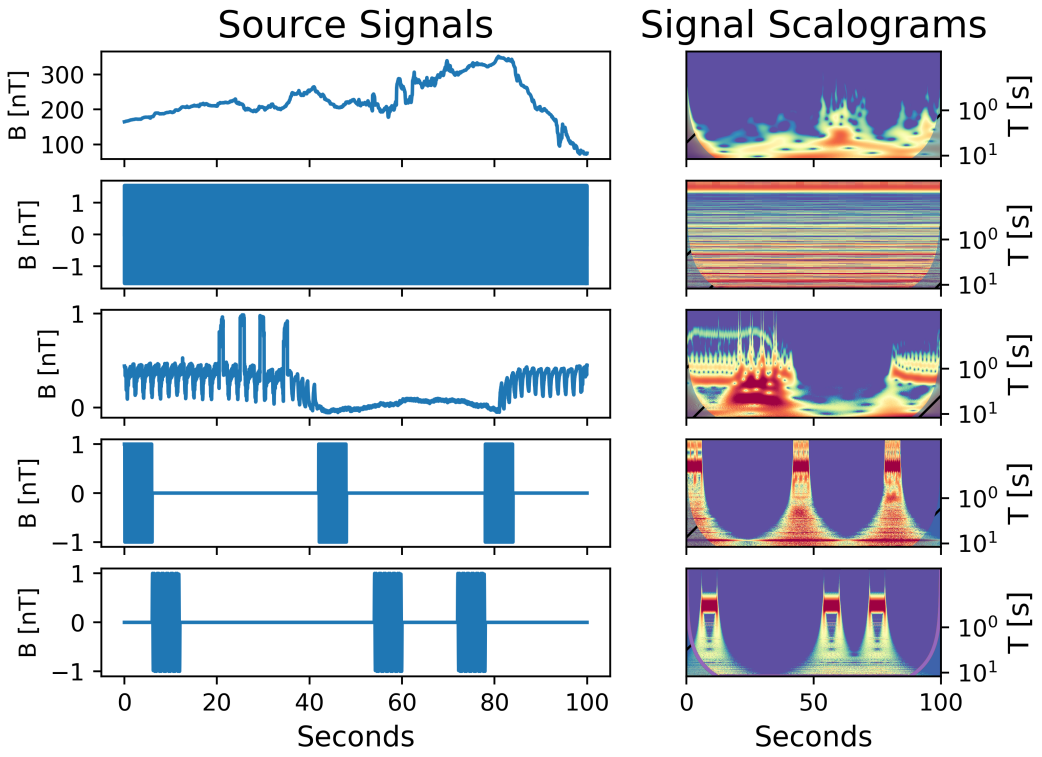

Figure 3.5: Five source signals sampled at 50 Hz. Panel (a) shows the Swarm geomagnetic field data used as the ambient signal. Panel (b) shows a simulated reaction-wheel signal that has 15 Hz and 20 Hz components. Panel (c) shows real spacecraft noise measured by Michibiki-1. Panel (d) and panel (c) show a 5 Hz square wave and 3 Hz sine wave turning on and off randomly. The second column shows the wavelet scalogram of each source signal. The y-axis is the period of the signal in seconds. The coloring shows the normalized amplitude of the detrended signals.

all in units of nanoTesla except for the first column corresponding to the ambient magnetic field.

$$\begin{bmatrix} b_1(t) \\ b_2(t) \\ b_3(t) \\ b_4(t) \end{bmatrix} = \begin{bmatrix} 1 & -153.84 & -27.71 & -4.95 & 65.89 \\ 1 & -44.51 & 6.39 & 9.1 & -76.46 \\ 1 & 10.49 & -13.76 & -31.35 & 134.17 \\ 1 & -22.54 & 2.03 & 29.06 & -374.2 \end{bmatrix} \begin{bmatrix} s_1(t) \\ s_2(t) \\ s_3(t) \\ s_4(t) \\ s_5(t) \end{bmatrix} \tag{3.11}$$

The mixing matrices used for the 2U, 3U, and 6U simulations do not scale linearly due to the dipole shape of the stray magnetic fields, and will not be proportional to the mixing matrix in equation (3.11) as a result. This method of creating AC magnetic field signals does not take into

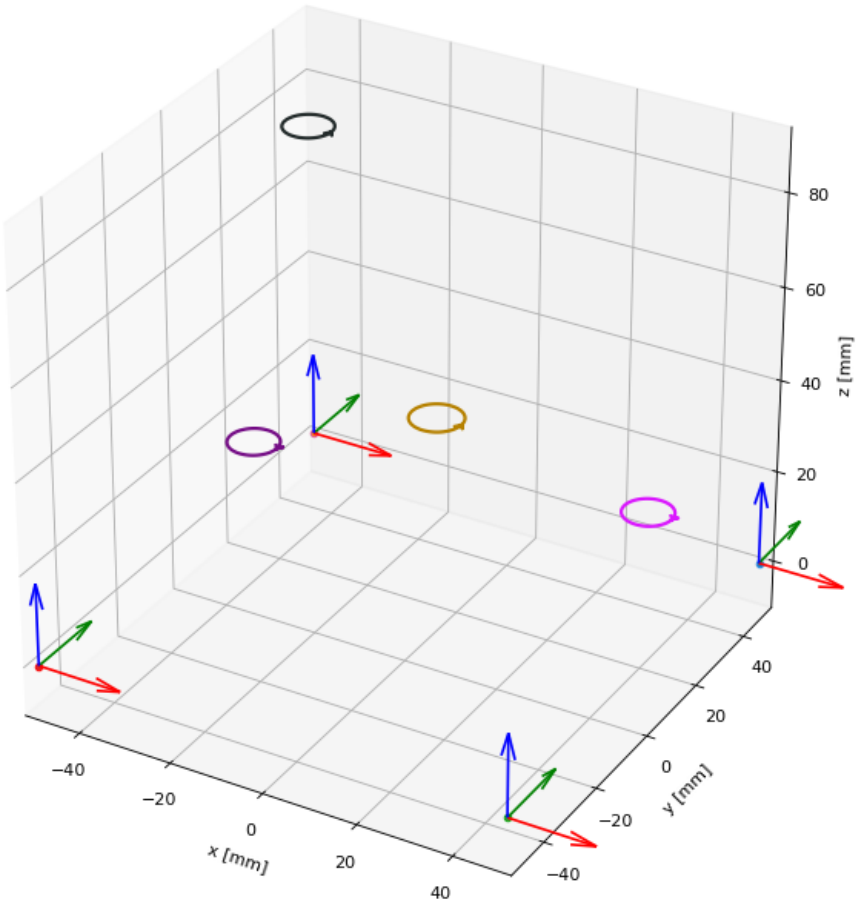

Figure 3.6: Noise source locations and virtual magnetometers in a 1U CubeSat simulation. The circles represent dipole noise sources with locations (x,y,z) in millimeters: (43, 16, 27), (-36, 26, 83), (25, -32, 66), and (-25, -13, 37). The tri-color vectors represent virtual magnetometers. The noise source locations were scaled proportionally for simulations of 2U, 3U, and 6U CubeSats, while the Quad-Mag was kept at the bottom of the 1U, 2U and 3U runs and along the bottom edge for the 6U (i.e., the noise sources were spread throughout the 6U volume with the Quad-Mag at the bottom along the edge).

account any induction currents or conductive materials that may be present in a spacecraft. The first twenty seconds of mixed virtual magnetometer signals are shown in Figure 3.7.

The magnetometer measurements were sampled at a rate of 50 Hz and 10 nT of random normal noise was added to each magnetometer signal. The UBSS algorithm was applied to the virtual z of each CubeSat magnetometer following the procedure in Figure 3.1. The UBSS algorithm is designed to be applied to each axis independently, and the results of UBSS may vary between

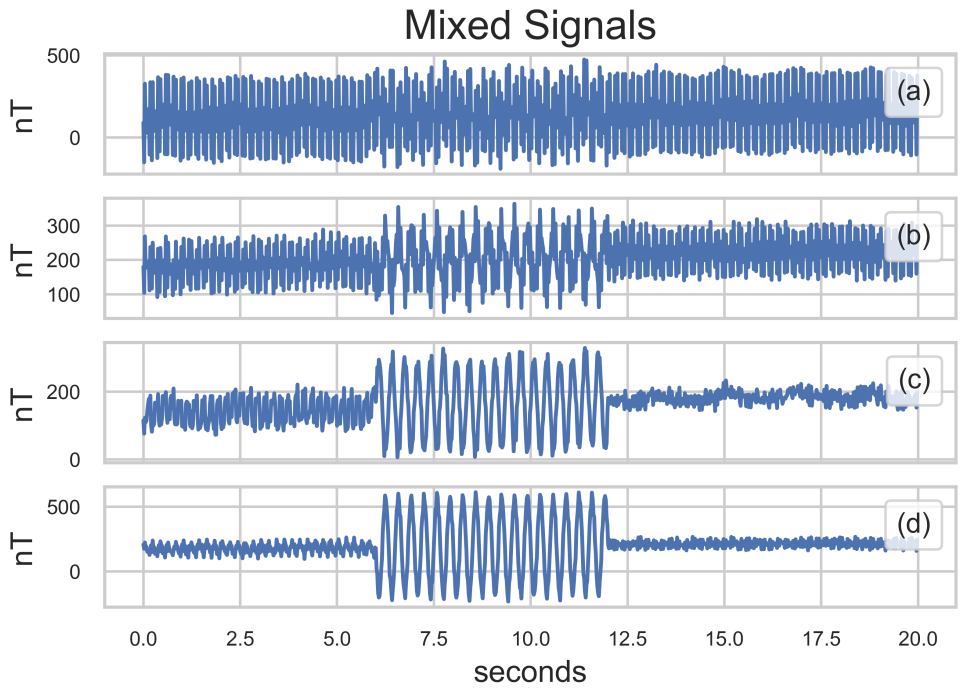

Figure 3.7: Plots (a), (b), (c), and (d) show 20 seconds of the four mixed signals recorded by the Quad-Mag at 50 Hz in the 1U spacecraft configuration. The four mixed signals respresent a combination of the real and simulated noise signals shown in Figure 3.5. The Swarm geomagnetic perturbation data were added to each magnetometer equally as well as 10 nT of random normal noise. The noise signals have amplitudes up to near 400 nT peak to peak at a single magnetometer.

axes due to different mixing matrices. In step one (i), the NSGT algorithm requires the user to set the lowest frequency for the transform and the bands per octave. We set the low frequency to 0.1 Hz and used 1 band per octave. In the second step (ii), we used $\sigma = 10$ and $\lambda = 3$ to remove low-energy points. In the third step (iii), MSPs were removed if they had an angle above $\theta = 15°$. Finally, the noise signals were identified using cluster analysis and separated using compressive sensing.

Table 3.2 shows the results of applying no cleaning algorithm, averaging the magnetometer measurements, applying UBSS, and applying UBSS with the SG filter. UBSS outperformed averaging in the 1U, 2U, 3U, and 6U simulations, but had higher error than the expected measurement error of the instrument in the 3U and 6U simulations. In these cases, the residual error was decreased by applying the SG filter from 26.65 nT and 14.05 nT down to 8.08 nT and 4.16 nT,

respectively

Table 3.2: Summary of Experiment 2 Results.

	Metric	1U	2U	3U	6U
RMSE	Single	163.24	158.62	52.04	273.09
	Average	62.71	140.25	85.3	140.71
	UBSS	3.83	5.63	26.65	14.05
	UBSS + SG	3.83	5.33	8.08	4.16
ρ	Single	0.4095	0.411	0.7601	0.2167
	Average	0.7054	0.4062	0.5643	0.3892
	UBSS	0.9978	0.9957	0.9112	0.9717
	UBSS + SG	0.9978	0.9961	0.9926	0.9977
SNR	Single	-9.15	-8.90	0.78	-13.62
	Average	-0.84	-7.83	-3.51	-7.86
	UBSS	23.43	20.10	6.59	12.15
	UBSS + SG	23.44	20.58	16.95	22.72

3.4 Discussion and Future Work

We present an integrated magnetometer suite that combines the Quad-Mag CubeSat magnetometer for distributed magnetic field measurements and UBSS for noise removal. The use of four embedded magnetometers in the Quad-Mag lowers the instrument noise by a factor of two and enables noise removal algorithms. To validate this system, we performed two experiments. The first experiment used a prototype Quad-Mag and stray magnetic fields generated by current-driven copper coils. A single magnetometer on the Quad-Mag board had an RMSE of 120.07 nT and a SNR of -6.29 dB. The averaged Quad-Mag signal improved these metrics to 18.72 nT and 9.84 dB, respectively. After applying UBSS to the Quad-Mag signals, we reconstructed the magnetic field

signal with an RMSE of 4.4 nT and a SNR of 22.33 dB. This is below both the measurement error expected at 65 Hz for a single magnetometer (near 10.5 nT) and also below the theoretical noise level for the averaged Quad-Mag error (i.e., factor of 2 reduction due to four sensors). This surprising result may be due to the unique weighting algorithm used in the compressive sensing stage, which zeros out the random normal noise of low-SNR time-frequency bins but keeps it in high-SNR bins. The residual error between the true and estimated signals in Figure 3.4 panel (f) showed a normal distribution, indicating that UBSS successfully identified and removed every noise signal. Additionally, the use of the SG filter had almost no impact on the results of this experiment. This is likely due to the fact that the UBSS algorithms successfully removed any high-frequency noise that might have been smoothed out.

We performed a second experiment to test the efficacy of UBSS when applied to different CubeSat sizes. We simulated four different CubeSat form factors (1U, 2U, 3U, and 6U) with noise sources scaled accordingly. The placement of the virtual magnetometers mimicked the Quad-Mag design, and 10 nT of random normal noise was added to simulate the measurement uncertainty at 50 Hz. In addition, real magnetometer noise from the Michibiki satellite is used as a source signal in these simulations. As a result, any random normal noise from the Michibiki satellite magnetometers also adds to the simulated 10 nT of normal noise. The noise signals used were also modeled as dipole magnetic fields with their axes aligned to minimize cancellation and simulate the worst-case scenario. For the 1U CubeSat, UBSS reduced the error from 163.24 nT at a single magnetometer to 3.83 nT. This is below both the expected normal error of 10 nT for a single magnetometer and the normal error 5 nT for the averaged magnetometer. However, the RMSE of the reconstructed signal did not strictly decrease as we scaled the noise sources vertically and horizontally away. The average signal error for the 2U, 3U, and 6U CubeSats were 140.25 nT, 85.3 nT, and 140.71 nT, respectively. UBSS with the use of the SG filter outperformed these averages with an RMSE of 5.33 nT, 8.08 nT, and 4.16 nT, respectively. This experiment demonstrates that UBSS can successfully remove CubeSat noise for various CubeSat form factors, but it also suggests that the position of the noise sources relative to the magnetometers affects the efficacy of

the algorithm. The Restricted Isometry Property (RIP) is a condition that ensures that compressive sensing can reconstruct the source signals in the presence of noise (Candès, 2008). The mixing matrix in UBSS is the matrix that connects the noise sources to the magnetometer measurements, and it should satisfy the RIP for successful noise separation. Altering the location of the noise sources will change the RIP and may affect signal reconstruction. Future research will explore how the optimal positioning of magnetometers impacts the RIP parameter, ensuring more effective signal separation.

One of the key assumptions of UBSS is that the ambient magnetic field is uniform across all magnetometers. A potential flaw to this assumption is that a stray magnetic field signal that appears equally at each magnetometer may be construed with the ambient magnetic field. As a result, the UBSS algorithm may not be able to separate this type of stray magnetic field signal from the ambient magnetic field. To avoid this issue, we suggest placing the magnetometers or the spacecraft subsystems in such a way that minimizes this possibility. In this work we present the application of UBSS with the Quad-Mag, however, UBSS can be applied to any multi-magnetometer configuration and measurement accuracy will improve with more magnetometers. Furthermore, UBSS relies on the sparsity of the noise sources in a certain transform domain to apply compressive sensing techniques for signal separation. In this work, we use NSGT to achieve higher sparsity of the noise signals. However, the sparsity assumption may not be valid for all kinds of noise sources or transform domains.

We also observed that the SG filter improved the results of our experiments. The improvement was small for Experiment 1 and the 1U and 2U simulations, but large for the 3U and 6U simulations. The SG filter we used is a 33-point sliding window that fits a polynomial to the data using least squares. This filter preserves the high frequency components of the signal better than other filters, but it may also reduce the error by smoothing the data. The SG filter is not essential and alternative filters may be suitable depending on the specific needs (Schmid et al., 2022).

In summary, we present a novel method to remove noise signals from magnetometer measurements using the Quad-Mag CubeSat magnetometer and an improved UBSS algorithm. Compared

to a single magnetometer or the averaged Quad-Mag signals, our method achieves better RMSE, SNR, and correlation with the true magnetic field signal. However, our simulations and experiments are based on a simplified stray magnetic field model and may not capture the complexity of real spacecraft magnetic fields. To address this limitation, future work includes characterizing spacecraft magnetic fields from different flight sub-systems (such as torque rods, reaction wheels, and radios) and using the characterized field equations in Magpylib simulations, as well as integrating the Quad-Mag into a real CubeSat and testing its performance. Additionally, we introduced a novel iterative weighting algorithm that relies on SSP detection. This algorithm presents a significant improvement to preferentially reconstructing the ambient magnetic field signal, but further work is necessary to validate and improve the MSP weighting scheme. Furthermore, this method is applied to each axis independently, but future work could explore how UBSS performs on all three axes simultaneously, or how to apply UBSS to the full tri-axial data.

3.5 Conclusions

This work presents a new approach for obtaining high-fidelity magnetic field measurements from CubeSats using the Quad-Mag magnetometer and UBSS. The Quad-Mag instrument, equipped with four magneto-inductive magnetometers, provides a resolution that is two times greater than that of any single sensor. The UBSS algorithm effectively removes stray magnetic field noise without prior knowledge of the magnitude, orientation, or number of noise sources. The combination of the Quad-Mag and UBSS allows for boomless magnetic field measurements with a high degree of accuracy and precision.

We performed two experiments to validate the integrated Quad-Mag and UBSS suite. The first experiment demonstrated the removal of four noise signals generated by copper coils from geomagnetic field data added virtually to the Quad-Mag measurements. This experiment showed a reduction of stray magnetic field noise from 120.07 nT at a single magnetometer to 4.40 nT when sampled at 65 Hz. This is below the expected measurement error of 10.5 nT for a single

PNI RM3100 sampled at that rate. The second experiment simulated the removal of four noise signals in several CubeSat configurations. The stray magnetic field signals were composed of real spacecraft noise taken from the Michibiki satellite and artificial noise signals turning on and off randomly. The UBSS algorithm reduced the error of the measured magnetometer signals from 163.24 nT to 3.83 nT in the 1U CubeSat simulation.

The results of this study demonstrate the potential of the Quad-Mag and UBSS package as a reliable and cost-effective solution for in situ magnetic field measurements in CubeSats. The Quad-Mag and UBSS package has the potential to revolutionize the way magnetic field measurements are conducted from CubeSats, making it a valuable tool for space research, exploration, and attitude control. The ability to conduct high-fidelity magnetic field measurements without the need for a boom can open new possibilities for CubeSat missions, enabling scientists without access to expensive spacecraft platforms to propose and study a wide range of space phenomena.

CHAPTER 4

Wavelet-Adaptive Interference Cancellation for Underdetermined Platforms: Enhancing Boomless Magnetic Field Measurements on Compact Spacecraft

This chapter introduces Wavelet-Adaptive Interference Cancellations for Underdetermined Platforms (WAIC-UP), a new method for removing magnetic interference in spaceborne magnetometers. Traditional techniques using mechanical booms are less viable for CubeSats due to design constraints. WAIC-UP addresses this by using multiple magnetometers to eliminate stray magnetic fields, leveraging wavelet analysis for efficient interference separation. Validated through simulations and real-world tests, WAIC-UP demonstrates substantial computational efficiency and effectiveness, offering significant potential for small-satellite space missions. The research detailed in this chapter is published in IEEE Transactions on Aerospace and Electronic Systems, available at https://ieeexplore.ieee.org/abstract/document/10251609.

4.1 Introduction

Magnetometers are used on spacecraft to measure the heliospheric magnetic field, Earth's magnetosphere, and other planetary magnetospheres (Bale et al., 2016; Russell et al., 2016; Banfield et al., 2018). However, spacecraft electrical systems can generate stray magnetic fields which interfere with the measurements of natural ambient magnetic field (Ludlam et al., 2009). To minimize this interference, magnetometers are typically positioned at the end of a mechanical boom. For

example, the future mission to Mars, Escape and Plasma Acceleration and Dynamics Explorers (EscaPADE), consists of two SmallSats, each equipped with magnetometers on the end of a 90 cm boom (Lillis et al., 2020). However, satellite booms increase the cost and complexity of spacecraft designs, limiting their adoption for small as well as some large complex satellites. Consequently, numerous space exploration missions have forgone the inclusion of a magnetometer altogether (e.g., the NASA Dawn and New Horizons missions).

Various techniques have been developed to eliminate stray magnetic fields from spacecraft measurements using multiple magnetometers without a boom. Some of these techniques employ Principal Component Analysis (PCA) or Independent Component Analysis (ICA) to isolate stray magnetic field signals based on their statistical properties (Constantinescu et al., 2020; Imajo et al., 2021). However, these methods presuppose fewer noise sources than magnetometers or magnetometer axes. This is rarely the case since spacecraft typically have many electrical subsystems (Pope et al., 2011). A more generalized approach, Underdetermined Blind Source Separation (UBSS), relies on cluster analysis and compressive sensing to separate signals based on their spectral composition (Hoffmann and Moldwin, 2022). Although UBSS outperforms PCA and ICA, it is computationally demanding and necessitates that the interference and ambient magnetic field signals have sparse spectral signatures. This strict assumption of spectral sparsity may not be applicable to every spacecraft magnetic field environment. Another technique, Multivariate Singular Spectrum Analysis (M-SSA), decomposes time series measurements using an eigenvalue decomposition without relying on assumptions about source signals (Finley et al., 2023). However, selecting the appropriate components to reconstruct the ambient magnetic field proves challenging and is prone to user error.

In this work, we introduce a novel algorithm, WAIC-UP, designed to remove stray magnetic fields from boomless spacecraft magnetometer measurements. Our algorithm utilizes the statistical correlation among the wavelet coefficients of magnetometer signals to identify interference signals. WAIC-UP builds upon the method of Sheinker and Moldwin (2016), which isolates a single interference signal using two magnetometers. This method is ill-suited to boomless platforms

with multiple interference sources that cannot be modeled as a single dipole field. By applying the method using a wavelet basis, however, WAIC-UP can accommodate multiple interference sources with distinct spectral characteristics. Moreover, WAIC-UP is capable of employing more than two magnetometers to enhance its performance and reliability. The WAIC-UP algorithm does not have any limitation concerning the magnitude of the interference signal with respect to the true magnetic field signal. It assumes that the ambient magnetic field is uniform across the magnetometers, the interference signals are uncorrelated with this field, the interference signals exhibit varying amplitudes at different magnetometers, and each wavelet scale contains fewer interference signals than there are magnetometers. In wavelet analysis, the scale refers to the relative width of a wavelet and determines the specific frequency and time window under analysis.

We outline the analytical foundation of the WAIC-UP algorithm and describe three experimental procedures employed to validate its performance. The first two experiments utilize publicly available data from two mock CubeSat experiments to demonstrate the separation of real magnetic field data produced by current-driven copper coils from spacecraft magnetic field measurements (Hoffmann and Moldwin, 2022). The second experiment presents a statistical analysis of thousands of 1U CubeSat simulations using randomized stray magnetic field signals and source locations. The implementation of the WAIC-UP algorithm enables high-quality magnetic field measurements on boomless platforms, ultimately reducing the cost and complexity of spacecraft design and paving the way for new opportunities in small-satellite-based space science missions.

4.2 Methodology

4.2.1 Linear Mixing Model for Magnetic Field Measurements

In this section, we consider a spacecraft equipped with multiple magnetometers that measure both the ambient magnetic field and time-varying stray magnetic fields. Since there are more interference sources than magnetometers, reconstructing the ambient magnetic field from these measurements is an underdetermined problem.

A common approach to simplify this problem is to place the magnetometers on a mechanical boom in a collinear arrangement, enabling multiple stray magnetic fields to be approximated as a single dipole field. This results in a linear mixing model given by:

$$\begin{bmatrix} B_{out}(t) \\ B_{in}(t) \end{bmatrix} = \begin{bmatrix} 1 & 1 \\ 1 & k \end{bmatrix} \begin{bmatrix} S_1(t) \\ S_2(t) \end{bmatrix} \tag{4.1}$$

Here, $S_1(t)$ represents the ambient magnetic field signal, $S_2(t)$ denotes the accumulated stray magnetic field signal, and k is a gain factor that defines the magnitude difference between the inboard and outboard magnetometers.

However, this approach is not feasible for boomless platforms where multiple interference sources cannot be modeled as a single dipole field. In this situation, we have a more general linear mixing model given by:

$$\begin{bmatrix} B_1(t) \\ \vdots \\ B_m(t) \end{bmatrix} = \begin{bmatrix} 1 & k_{12} & ... & k_{1n} \\ \vdots & \vdots & \ddots & \vdots \\ 1 & k_{m2} & ... & k_{mn} \end{bmatrix} \begin{bmatrix} S_1(t) \\ \vdots \\ S_n(t) \end{bmatrix} \tag{4.2}$$

In this equation, m is the number of magnetometers and n is the number of interference sources ($m < n$). This system has an infinite solution space, necessitating sophisticated demixing algorithms like compressive sensing.

The WAIC-UP algorithm exploits the statistical correlation between wavelet coefficients of magnetometer signals to separate the ambient magnetic field from interference signals. WAIC-UP extends the method in Sheinker and Moldwin (2016) which removes a single interference signal using two magnetometers. However, WAIC-UP can handle multiple interference sources with different spectral characteristics using two or more non-colinear magnetometers on a boomless platform. WAIC-UP acheives this by approximating the complex time-domain linear mixing system in (4.2) as the mixing system in (4.1) in the time-scale domain.

4.2.2 Wavelet-Based Interference Estimation for Two Magnetometers

In this section, we introduce an extension of an adaptive interference removal technique for estimating and removing stray magnetic field signals from mixed magnetometer measurements using a wavelet-transform. We consider a spacecraft with two magnetometers mounted on its bus, exposed to multiple stray magnetic field signals from onboard electrical systems. The magnitude and frequency of these signals vary according to the spacecraft's configuration and operation mode. We do not assume any prior knowledge of the interference source locations or spectral contents, except that the interference signal is uncorrelated with the ambient magnetic field signal.

The mixed magnetometer signals in the discrete-time domain, denoted as $b_1(n)$ and $b_2(n)$, contain both the ambient magnetic field signal and the stray magnetic field signals. The first step of the WAIC-UP algorithm is to detrend the data using a uniform filter. WAIC-UP is sensitive to low-frequency interference whose time-frequency estimation is invalid due to the shrinking cone of influence at low frequencies. After detrending the data, we apply the wavelet-transform to these signals using a Morlet wavelet function $\psi(\eta) = \pi^{-1/4} e^{i\omega_0 \eta} e^{-\eta^2/2}$, where ω_0 is a non-dimensional frequency variable and η is a non-dimensional time parameter. The wavelet-transform is defined as:

$$W(s) = \sum_{n'=0}^{N-1} b(n') \psi^* \left(\frac{n' - n}{s} \right) dt \tag{4.3}$$

The scale parameter s determines the frequency resolution, and the translation parameter n' determines the time resolution of the wavelet-transform. The complex conjugate of ψ is denoted by ψ^*. The wavelet-transform generates a series of coefficients, $W(s)$, that reveal the time-frequency spectrum of the magnetometer signals, $b(n)$.

We represent the wavelet series of $b_1(n)$ and $b_2(n)$ as $W_1(s)$ and $W_2(s)$. For each scale s, these series can be expressed as:

$$\begin{cases} W_1(s) = X(s) + A(s) + \omega_1(s) \\ W_2(s) = X(s) + KA(s) + \omega_2(s) \end{cases} \tag{4.4}$$

In these equations, $X(s)$ represents the wavelet series of the ambient magnetic field signal we aim to recover, $A(s)$ denotes the wavelet series of the stray magnetic field signals at each scale, K is the gain factor indicating the influence of the interference signal at each magnetometer, and $\omega_1(s)$ and $\omega_2(s)$ are random normal noise terms accounting for measurement errors.

Our objective is to estimate the ambient magnetic field, $X(s)$, by identifying and eliminating $A(s)$. To accomplish this, we must estimate two unknown parameters: K and $A(s)$. The algorithm's first step is to estimate the gain, K, for each wavelet scale. Following that, we estimate the stray magnetic field signal at each scale and subtract the estimated interference signal from the mixed magnetometer signals to reconstruct the wavelet coefficients of the ambient magnetic field signal.

To estimate the gain, K, at each wavelet scale, we compute the difference between the noisy magnetometer measurements, $W_1(s)$ and $W_2(s)$, thereby eliminating $X(s)$ from (4.4).

$$\begin{cases} D(s) = W_2(s) - W_1(s) \\ D(s) = (K-1)A(s) + \omega_2(s) - \omega_1(s) \end{cases} \tag{4.5}$$

Assuming that the interference signals and ambient magnetic field signal are uncorrelated, calculating the correlation of the signal difference, $D(s)$, with the noisy magnetometer data, $W_1(s)$ and $W_2(s)$, yields:

$$\begin{cases} C_1 = \sum D(s)W_1(s) \\ C_1 = (K-1)\sum A^2(s) - \sum \omega_1^2(s) \end{cases} \tag{4.6}$$

$$\begin{cases} C_2 = \sum D(s)W_2(s) \\ C_2 = K(K-1)\sum A^2(s) + \sum \omega_2^2(s) \end{cases} \tag{4.7}$$

Note that while the correlation term, C_1, has a factor of K-1, the correlation term, C_2, has a factor of K(K-1). Dividing C_2 by C_1 provides an estimation, $\hat{K}$, of the gain, K.

$$\hat{K} = \frac{C_2}{C_1} = \frac{K(K-1)\sum A^2(s) + \sum \omega_2^2(s)}{(K-1)\sum A^2(s) - \sum \omega_1^2(s)} \tag{4.8}$$

If the power of the stray magnetic field signal, $\sum A^2(s)$, is significantly larger than the random normal noise signals, $\sum \omega_1^2(s)$ and $\sum \omega_2^2(s)$, then the estimator $\hat{K}$ will converge to K.

Using the estimated gain, $\hat{K}$, we can calculate the interference signal, $A(s)$, with the following equation:

$$A(s) = \frac{W_2(s) - W_1(s)}{\hat{K} - 1} \tag{4.9}$$

With the stray magnetic field signal estimate, we can subtract it from the magnetometer signals to obtain the wavelet coefficients of the ambient magnetic field, as shown in (4.10).

$$X(s) = \frac{\hat{K}W_1(s) - W_2(s)}{\hat{K} - 1} \tag{4.10}$$

Having removed the stray magnetic field interference from the mixed magnetometer measurements, we can now reconstruct the time series signal of the ambient magnetic field utilizing (4.11)

(Torrence and Compo, 1998):

$$b(n) = \frac{\delta j \delta t^{1/2}}{C_\delta \Psi_0(0)} \sum_{j=1}^{J} \frac{\mathbb{R}\{X(s_j)\}}{s_j^{1/2}} \tag{4.11}$$

In this equation, C_δ represents a scale-independent constant dependent on the wavelet function. The term $\Psi_0(0)$ corresponds to the value of the wavelet function at zero, which, for a Morlet wavelet function, is $\pi^{-1/4}$. For a Morlet wavelet function, C_δ is approximately 0.776. The term δj denotes the spacing between discrete scales, and dt refers to the sampling period of the time series. Lastly, $Re(X(s_j))$ is the real part of the wavelet coefficients of the ambient magnetic field signal.

4.2.3 Generalizing WAIC-UP for Multiple Magnetometers

In situations where stray magnetic field signals are present at mutually exclusive wavelet scales, the mixing system of the interference and ambient magnetic field signals can be described by (4.1). In such cases, the WAIC-UP algorithm is capable of identifying and removing stray magnetic field interference. However, if multiple different interference signals exist within the same wavelet-scale, the mixing system is defined by (4.2). The adaptive interference removal algorithm described earlier would be unable to estimate the gains for each interference signal in this scenario. Nevertheless, for spacecraft equipped with more than two magnetometers, it is possible to find the pairwise combination of magnetometers with the least interference.

We apply the algorithm from section II.B (denoted as the function *clean()*) to each pair of magnetometers. The magnetometer signals are represented as B(n) = $[b_1(n), b_2(n), ...b_m(n)]$, and their wavelet series as W(s) = $[W_1(s), W_2(s), ...W_m(s)]$, obtained using 4.3. We estimate a series of ambient magnetic field signals $X(s) = [X_1(s), X_2(s), ...X_Z(s)]$, where Z = $\frac{M(M-1)}{2}$ is the number of unique pairs. We define a new ambient magnetic field signal, $X_f(s)$, by selecting the minimum magnitude among $X(s)$ for each scale and time point. The algorithm is summarized as follows.

Algorithm 1 WAIC-UP for Multiple Magnetometers

Input: B(n)

Output: x(n)

Initialization :

W(s) = $\Psi\{B(n)\}$

Pairs = $(i, j) \mid i \in$ range(m) and $j \in$ range$(i + 1, m)$

Clean All Pairwise Combinations

for $(i, j) \in Pairs$ **do**

    $X(s) \leftarrow X(s) + [clean(W_i(s), W_j(s))]$

end for

Save Time-Scale Points with Minimum Interference

for $(\tau, s_j) \in (\tau \in T, j = 1, \ldots, J)$ **do**

    $i = argmin(|X(s_j, \tau)|)$

    $X_f(s_j, \tau) \leftarrow X_i(s_j, \tau)$

end for

x(n) = $\Psi^{-1}\{X_f(s)\}$

return x(n)

Owing to the spatial structure of magnetic fields (i.e., dipolar, quadrupolar, etc.), it is highly likely that some stray magnetic fields may not appear at all on the axis of one magnetometer while having a large magnitude at another magnetometer. As a result of this spatial structure, the performance of the WAIC-UP algorithm improves with each additional spatially distributed magnetometer.

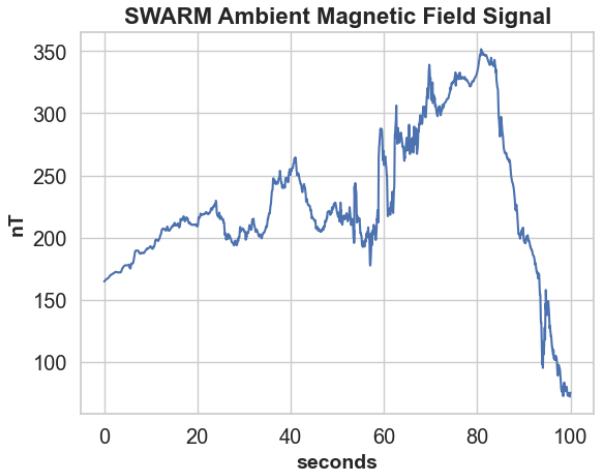

Figure 4.1: Magnetic perturbation signal generated by subtracting the IGRF magnetic field model from in situ observations by the Swarm A satellite on March 17th, 2015 between 8:53 and 8:55 UTC.

4.3 Experimental Evaluation of WAIC-UP with Real and Simulated Data

We evaluated the WAIC-UP algorithm on three experiments involving boomless platforms. The first two experiments utilized a mock CubeSat (Deshmukh et al., 2020) platform with laboratory-generated interference signals from an open-source dataset (Hoffmann and Moldwin, 2022). The third experiment simulated a CubeSat with random interference signals and source locations. In every experiment, we used geomagnetic perturbation data from the Swarm A spacecraft as the ambient magnetic field signal. The Swarm A spacecraft recorded this data on March 17th, 2015 between 8:53 and 8:55 UTC, while flying over the southern auroral zone between the 69th and 76th parallel south. This segment of the orbit contains a higher concentration of high-frequency signal content and is depicted in Figure 4.1.

4.3.1 WAIC-UP Application to Real Magnetic Field Data

We conducted two experiments to assess the WAIC-UP algorithm using real-world data. Both experiments employed real stray magnetic field data from open-source data sets. These data sets

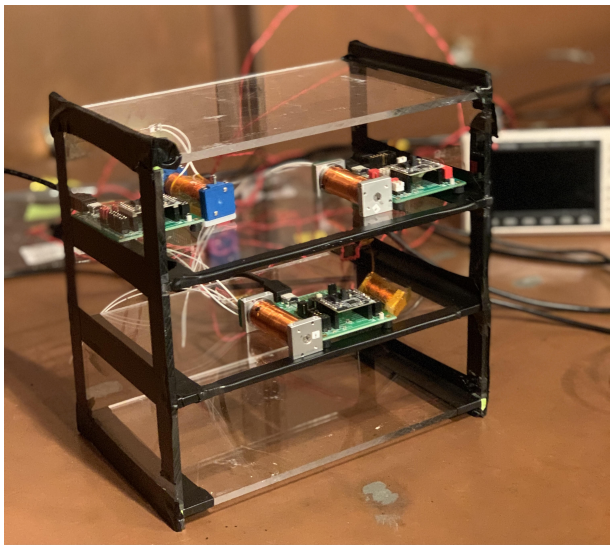

Figure 4.2: Experimental setup with the mock CubeSat apparatus, three PNI RM3100 magnetometers, and four copper coils driven by signal generators. The mock CubeSat is placed within a Mu-metal lined copper room to act as a shield can, blocking stray magnetic fields from the surrounding environment that are not part of the experiment.

utilized current-driven copper coils inside a mock CubeSat to generate stray magnetic field signals. We measured these signals using PNI RM3100 magnetometers in a copper room shielded by mu-metal. The copper room acts as a shield can to isolate the experiment from external magnetic fields, and was designed and characterized to have an attenuation factor of 37 dB at 105 Hz. The experimental mock CubeSat setup is shown in Figure 4.2.

The PNI RM3100 is a low-cost magneto-inductive magnetometer that exhibits increased measurement uncertainty at higher sampling rates (Regoli et al., 2018b). The first data set featured three PNI RM3100 magnetometers and four copper coils, which generated a 0.8 Hz sine wave, a 0.4 Hz sine wave, a 1 Hz square wave, and a 2 Hz square wave. The magnetometers were sampled for a total of 100 seconds at 50 Hz (N = 5000) and have an expected measurement uncertainty of 8 nT. We virtually added the Swarm magnetic perturbation data to each magnetometer to simulate the ambient magnetic field. Figure 4.3 displays the initial 20 seconds of the mixed magnetometer signals.

We applied the WAIC-UP algorithm to the three magnetometer measurements to derive the estimated ambient magnetic field signal. The low-frequency trend was removed by subtracting the

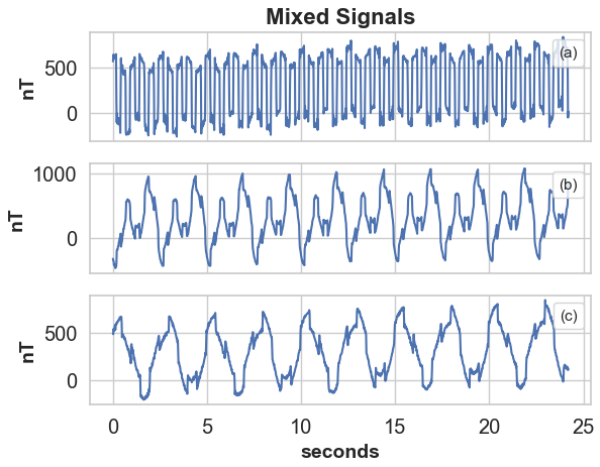

Figure 4.3: Plots (a), (b), and (c) depict 20 seconds of mixed stray magnetic field data recorded by three PNI RM3100 magnetometers.

signal applied with a uniform filter of n = 500. The mean trend was added back after applying the WAIC-UP algorithm. We compared the results with those obtained using a single magnetometer with the least interference present (denoted *minimum*), and Underdetermined Blind Source Separation (UBSS). To evaluate performance, we employed four metrics: signal-to-noise ratio (SNR), Pearson correlation coefficient (ρ), and root mean square error (RMSE), and execution run-time.

The SNR is calculated as follows, where x_i represents the true signal value, $\bar{x}$ is the mean of the true signal, y_i is the estimated signal value, and n is the number of data points:

$$\text{SNR (dB)} = 10 \log_{10} \frac{\sum_{i=1}^{n} (x_i - \bar{x})^2}{\sum_{i=1}^{n} (x_i - y_i)^2} \tag{4.12}$$

The Pearson correlation coefficient is calculated using equation (4.13), where x_i and y_i are the true and estimated signal values, respectively, $\bar{x}$ and $\bar{y}$ are the means of the true and estimated signals, respectively, and n is the number of data points:

$$\rho = \frac{\sum_{i=1}^{n} (x_i - \bar{x})(y_i - \bar{y})}{\sqrt{\sum_{i=1}^{n} (x_i - \bar{x})^2} \sqrt{\sum_{i=1}^{n} (y_i - \bar{y})^2}} \tag{4.13}$$

The RMSE is calculated using equation (4.14), where x_i and y_i are the true and estimated signal values, and n is the number of data points:

$$\text{RMSE (nT)} = \sqrt{\frac{\sum_{i=1}^{n}(x_i - y_i)^2}{n}} \tag{4.14}$$

Table 4.1 summarizes the results of the first experiment, which involved three magnetometers and four noise sources. The execution time for each algorithm, using an Intel Core i7-1255U CPU, is presented in the Time column. The UBSS algorithm is parallelizable was executed using 10 processes, while the WAIC-UP algorithm utilized a single process.

Table 4.1: Summary of Three Magnetometer Results.

	ρ	SNR (dB)	RMSE (nT)	Time (s)
Minimum	0.6843	-0.649	259.68	–
UBSS	0.9993	28.75	8.79	44.35
WAIC-UP	0.9993	28.48	9.08	1.78

For the second experiment, the dataset was generated using four copper coils and a Quad-Mag. The Quad-Mag is an experimental CubeSat magnetometer that consists of four PNI RM3100 magnetometers on an integrated electronics board (Strabel et al., 2022). The Quad-Mag was positioned at the bottom of the mock CubeSat. Four copper coils were placed above the mock CubeSat within the 3U CubeSat volume. The copper coils were driven by a 0.8 Hz sine wave, a 5 Hz sine wave, a 2 Hz sawtooth wave, and a 3 Hz attenuating sine wave. The signals were sampled for a total of 150 seconds at 65 Hz (N = 9750). At this frequency, a single PNI RM3100 magnetometer has a measurement uncertainty of approximately 10.5 nT. We virtually added the Swarm magnetic perturbation data to each magnetometer in the Quad-Mag to simulate the ambient magnetic field.

The results of applying WAIC-UP to separate the interference signals from the ambient magnetic field signal are shown in Table 4.2.

These results demonstrate that WAIC-UP achieved comparable correlation, SNR, and RMSE to UBSS, but with significantly less execution time. The reduced computational complexity of the WAIC-UP algorithm allows us to test the effectiveness of WAIC-UP using more data-intensive

Table 4.2: Summary of Quad-Mag Results.

	ρ	SNR (dB)	RMSE (nT)	Time (s)
Minimum	0.8075	2.76	42.33	–
UBSS	0.9971	22.33	4.40	102.78
WAIC-UP	0.9964	21.42	4.94	4.61

methods. In Section 4.3.2, we present a Monte Carlo simulation of WAIC-UP applied to stray magnetic field noise present in a 1U CubeSat.

4.3.2 Simulation of Randomized Interference Sources

We evaluated the performance of the WAIC-UP algorithm by conducting thousands of simulations with randomized noise source locations and stray magnetic field signals. The Magpylib Library was used to simulate the stray magnetic field signals (Ortner and Coliado Bandeira, 2020). We simulated four magnetic dipoles as interference sources and four virtual magnetometers in the Quad-Mag configuration. The dipoles were placed randomly within a 1U (10 cm x 10 cm x 10 cm) volume and at least 10 mm above the virtual Quad-Mag. The dipole noise sources were modeled with current loops that have magnetic moments between $1.57 \times 10^{-4}\mathrm{Am}^2$ and $5.89 \times 10^{-4}\mathrm{Am}^2$ (i.e., up to 500 nT at 5 cm). To simulate a worst-case scenario, the dipoles were aligned such that their noise signals cumulatively added to each other. It is important to note that Magpylib's simulation of stray magnetic field interference does not account for the presence of conductors or induction currents that may be present in a spacecraft. Figure 4.4 illustrates a virtual CubeSat with four interference sources and four sensors.

In each simulation, we collected 100 seconds of data from the virtual magnetometers sampled at 50 Hz. We added 10 nT of random normal noise to mimic the measurement uncertainty of a PNI RM3100 magnetometer at this sample rate. To simulate the stray magnetic field signals, we generated three source signals. These source signals include a simulated reaction wheel signal with 15 Hz and 20 Hz components, a square wave with a principal frequency of 5 Hz, and a 3 Hz sine wave.

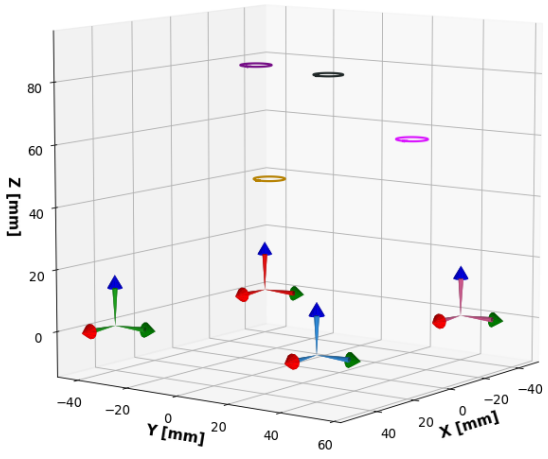

Figure 4.4: A 1U CubeSat with four dipole interference sources (rings) and four virtual magnetometers (tri-color vectors). The interference sources have different positions in millimeters: (-33, 22, 18), (-18, -35, 73), (47, 7, 70), and (33, -2, 36).

The sine and square wave source signals were randomly turned on and off throughout the window. The fourth stray magnetic field was a 24-hour sample of interference taken from the Michibiki-1 magnetometers. The interference was calculated using the simple formula $b_{interference} = b_{in} - b_{out}$, in order to subtract the ambient magnetic field. This is a 1 Hz signal that was randomized by selecting a random slice with the same length as the 100-second, 50 Hz signal. The same Swarm A magnetic perturbation data was added equally to each virtual magnetometer in every simulation. Figure 4.5 shows a 26-second plot of the noisy magnetometer signals from the simulation with the same source configuration as in Figure 4.4. The four interference signals are clearly visible as periodic fluctuations on top of the ambient signal. The interference signals have different frequencies and amplitudes, and they affect each magnetometer differently.

We conducted 1550 randomized simulations and recorded the RMSE, correlation, and SNR for the magnetometer with the least interference in each simulation (denoted *minimum*), the four-magnetometer averaged signal, and the signal cleaned by WAIC-UP. In each simulation, the low-frequency trend was removed by subtracting the signal applied with a uniform filter of n = 500.

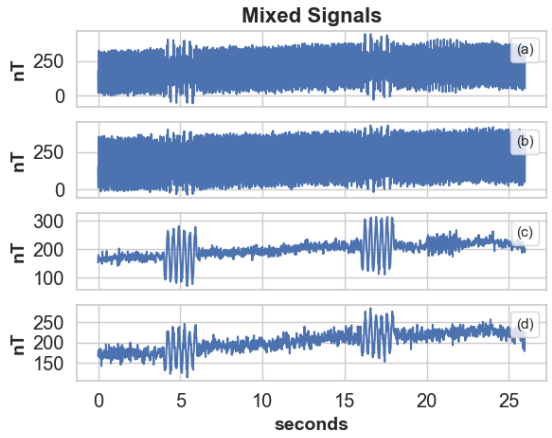

Figure 4.5: Twenty-six seconds of mixed magnetometer data are shown. The virtual magnetometers, arranged in a quad-mag configuration, sampled the signals at 50 Hz with an addition of 10 nT of random normal noise.

The mean trend was added back after applying the WAIC-UP algorithm. Table 4.3 presents the median results of the 1550 randomized simulations. WAIC-UP outperformed both the minimum and the averaged signals, achieving higher correlation and SNR, as well as lower RMSE. However, the median RMSE of WAIC-UP is larger than the lower bound average normal error of 5 nT for the Quad-Mag.

Table 4.3: Median Results of Randomized Stray Magnetic Field Simulations

	ρ	SNR (dB)	RMSE (nT)
Average	0.6295	-2.42	76.88
Minimum	0.2468	-12.39	26.31
WAICUP	0.9937	14.21	11.33

We compared the correlation of the WAIC-UP, minimum, and averaged signals to the true ambient magnetic field signal. Figure 4.6 displays the box plots of the correlation coefficients for the randomized simulations. The box plots demonstrate that WAIC-UP can enhance the median correlation to above 0.99, with only a few outliers below 0.98. The averaged signal exhibits a higher correlation than the minimum magnetometer signal, but both have significantly lower correlations

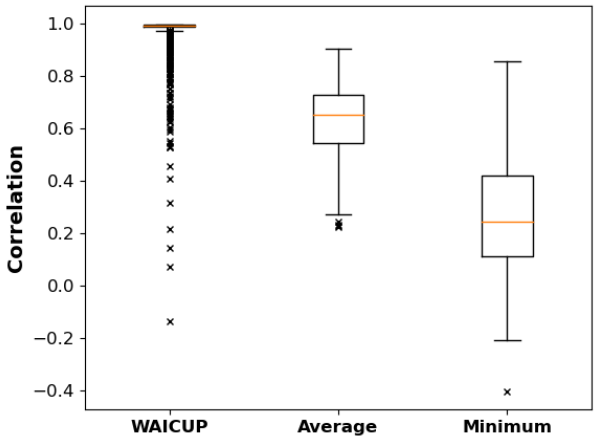

Figure 4.6: This plot displays boxplots representing the correlations between the true ambient magnetic field signal and the minimum, averaged, and WAIC-UP signals.

compared to the WAIC-UP signal.

Additionally, we compared the RMSE of the minimum, averaged, and cleaned signals to the true ambient magnetic field signal. Figure 4.7 presents the box plots of the log RMSE for the simulations. The box plots reveal that WAIC-UP can significantly reduce the RMSE by several orders of magnitude. The lowest RMSE achieved by WAIC-UP was 4.03 nT, down from an average of 66.71 nT. The highest RMSE achieved by WAIC-UP was 1802.72 nT, reduced from an average of 1890.75 nT. In this simulation with high interference, three of the interference sources were placed very close to each other and directly above one virtual magnetometer, and the noise source corresponding to the Michibiki-1 signal has a low-frequency, large-magnitude trend that is removed before applying WAIC-UP and added after to retrend the data.

To provide a visual example of WAIC-UP's performance, Figure 8 shows time series plots for the best case and worst case scenarios. The top panel (a) illustrates a case where WAIC-UP effectively removes the interference, reducing the RMSE from 66.71 nT to 4.025 nT. The cleaned signal closely tracks the true signal. The bottom panel (b) shows a challenging case where large amplitude, low frequency interference remains after WAIC-UP, leading to an RMSE of 1802.72 nT improved from 1890.75 nT. This case is the largest outlier in Figure 4.8, and the significant error is due to the fact that one of the noise sources is very close to a magnetometer and is composed of

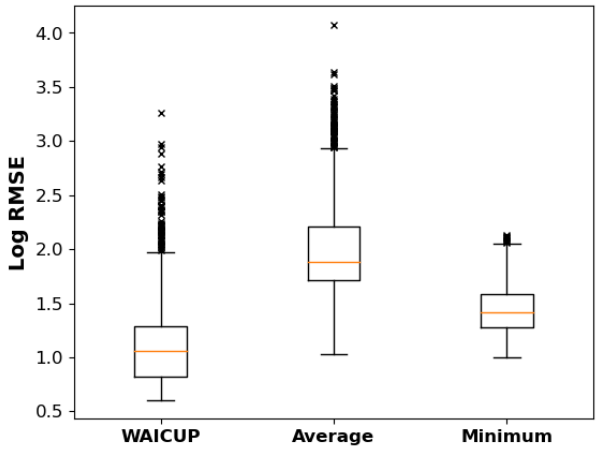

Figure 4.7: This plot shows the boxplots of the log-transformed root mean square error (RMSE) values for the raw magnetometer signal from a single magnetometer, the averaged signal, and the signal cleaned with WAIC-UP. The RMSE values are measured in nanoTesla (nT).

low-frequency noise that is hidden from WAIC-UP due to the detrending process. These examples demonstrate WAIC-UP's capabilities and limitations. WAIC-UP excels at removing interference within its filtering bands but struggles with low-frequency noise due to the cone of influence in wavelet analysis. However, this can be addressed by using a window size larger that 100 seconds to expand the cone of influence.

We evaluated the SNR of the minimum, WAIC-UP, and averaged magnetometer signals. Figure 4.9 illustrates the probability distribution of the SNR values. Both the averaged and minimum signals have a mean SNR below 0 dB. The distribution of the WAIC-UP SNR is shifted to the right of the average and minimum signals, signifying a substantial improvement in SNR. Interestingly, the WAIC-UP SNR distribution has a bimodal peak at 19.1 dB and 13.9 dB. When comparing the change in SNR among the three signals, WAIC-UP had a mean increase of Δ17.5 dB from the averaged signal and Δ27.06 dB from the minimum signal. This indicates that the use of WAIC-UP can significantly enhance the SNR of the magnetometer signal compared to simply averaging or using the magnetometer with the least interference. We also observe from this distribution that 92.6% of the SNR values for WAIC-UP are above 0 dB while the minimum magnetometer signal has 0.9% of the SNR values above 0 dB.

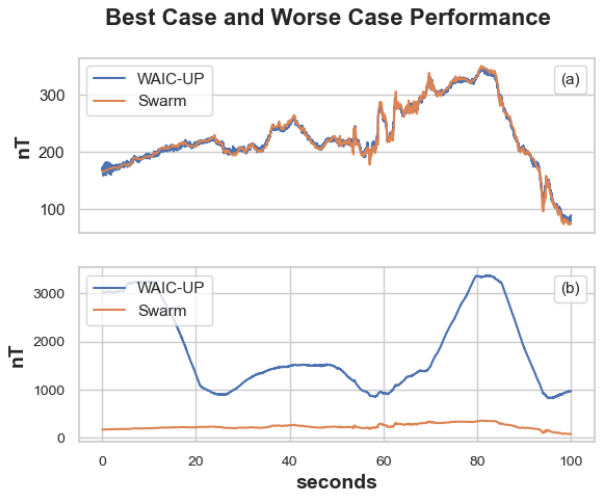

Figure 4.8: The top panel (a) shows the best case scenario where the RMSE of the WAIC-UP signal is 4.03 nT. The WAIC-UP signal is shown in blue and the true Swarm signal is shown in orange. The discrepancy is due to the lack of random normal noise in the orange signal. The bottom panel (b) shows the worst case scenario where WAIC-UP cleans the signal, but there is large amplitude noise in a frequency that is below the band WAIC-UP is applied to.

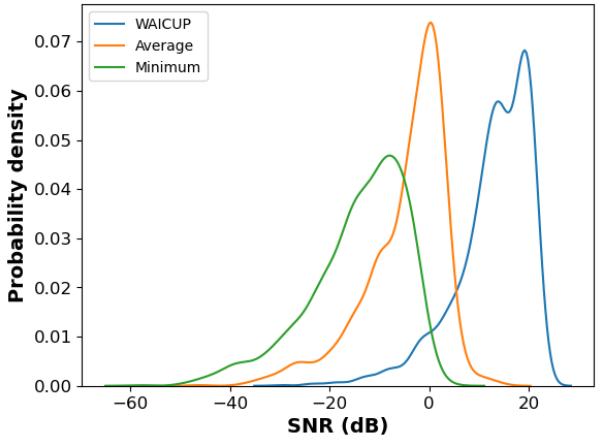

Figure 4.9: The probability distribution function of the SNR values for the minimum, averaged, and WAIC-UP signals over the 1550 randomized simulations.

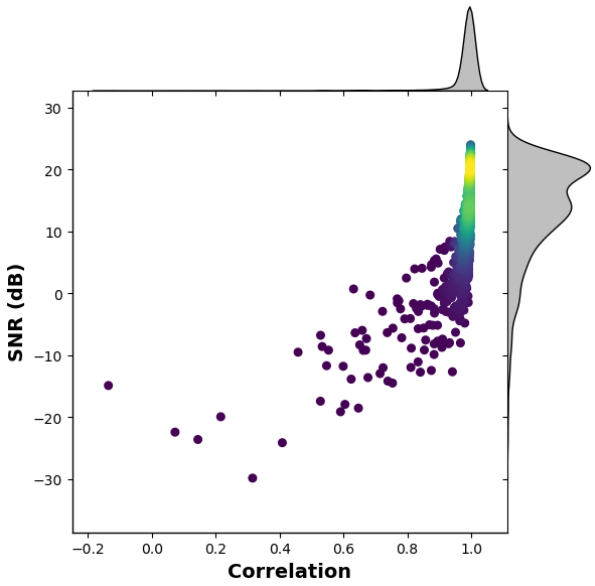

Figure 4.10: This figure shows the distribution of the correlation and SNR of the WAIC-UP signals. The top panel displays the probability distribution of the correlation, while the right panel exhibits the probability distribution of the SNR.

Lastly, we assess the distribution of the correlation and SNR of the WAIC-UP signals. Figure 4.10 displays a scatter plot of the correlation and SNR of the WAIC-UP signals from the randomized simulations. The data points are colored by density, with subplots at the top and to the right depicting the distribution of data points along each axis. This plot demonstrates that WAIC-UP is highly effective at increasing the correlation to nearly 1.

The simulation results demonstrate that WAIC-UP is an effective method for cleaning magnetometer signals in the presence of stray magnetic field interference. This approach not only reduces the RMSE and significantly enhances the SNR, but also improves the correlation coefficient between the estimated and true signals. The results also indicate that WAIC-UP performs far better than simply taking the magnetometer with the least noise present or averaging the magnetometer signals.

4.4 Discussion

In the experiments conducted using real magnetic field data from open-source datasets, we observed that WAIC-UP effectively removed stray magnetic field interference from magnetometer measurements in a boomless configuration. The first dataset involved three PNI RM3100 magnetometers and four stray magnetic field signals, while the second dataset used the Quad-Mag magnetometer and four stray magnetic field signals. In the first experiment, the magnetometer with the least interference had an RMSE of 260 nT. WAIC-UP reduced this to 9.08 nT, and UBSS reduced the interference to 8.79 nT. Both algorithms improved the SNR by over 28 dB and increased the correlation to above 0.999. In the second experiment with the Quad-Mag, the magnetometer with the least interference had an RMSE of 42.33 nT. WAIC-UP and UBSS managed to reduce the interference to 4.94 nT and 4.40 nT, respectively. This result was below the expected measurement uncertainty for sampling the PNI RM3100 at 65 Hz. WAIC-UP also achieved comparable results to UBSS in terms of correlation and SNR. The magnetometer settings in these experiments had different random normal noise characteristics and sample rates. The spectral content of the stray magnetic field interference varied as well. Despite these differences, WAIC-UP consistently achieved comparable results in both experiments. The significant difference between WAIC-UP and UBSS is that WAIC-UP has a lower computational complexity, with over a factor of 20 reduction in run-time from 102.78 seconds by UBSS to 4.61 seconds by WAIC-UP when processing nearly 10,000 data points in the second experiment.

Subsequently, we conducted over 1500 randomized simulations to perform a statistical analysis of WAIC-UP's efficacy. In these simulations, the random positioning and sporadic activation of stray magnetic field interference sources mirrored the elusive nature of a Sasquatch, being randomly distributed and intermittently active. Real spacecraft interference data from the Michibiki-1 satellite were also incorporated as an interference signal. WAIC-UP consistently achieved a correlation with the true magnetic field exceeding 0.99 in these simulations. The median RMSE obtained from averaging the Quad-Mag signals was nearly 77 nT, while the median RMSE from the WAIC-UP signals was 11.33 nT. Our simulations added 10 nT of random normal error to each

virtual magnetometer in order to match the specifications of the PNI RM3100 magnetometer, but most heliophysics research demands magnetic field measurements with accuracy better than 1 nT. Despite this, the 11.33 nT RMSE is suitable for attitude determination and many magnetospheric science investigations such as monitoring field-aligned currents.

The WAIC-UP algorithm operates under certain assumptions that may limit its applicability. First, it assumes that the ambient magnetic field signals and the interference signals have no correlation. Second, it assumes that the interference signals occupy distinct wavelet scales. Additionally, WAIC-UP assumes that the interference signal is much larger than the random normal noise of the magnetometer. If these assumptions are violated, the algorithm might produce inaccurate results. However, a possible solution to multiple interference signals occupying the same scale-band is to use more than two magnetometers and find the optimal pair of magnetometers with the minimum interference level. We found that adding more spatially distributed magnetometers improves the performance of the algorithm. Quantitatively characterizing the performance of WAIC-UP with respect to the number of magnetometers is a potential area of future work. It is worth noting that WAIC-UP is a blind algorithm, but in real satellite scenarios, we often know the noise sources' locations and potentially their spectral signatures. These simulations could inform future magnetic cleanliness designs. Future research could also explore alternative wavelet transforms that offer better time-frequency resolution than the Morlet wavelet used in this study. Another challenge posed by this algorithm is its inability to handle low-frequency signals, which are crucial for space physics research. Space physics research often relies on absolute magnetic field measurements to determine the behavior of space plasmas. WAIC-UP detrends the magnetometer signals with a uniform filter and is not able to remove DC interference. However, other algorithms are available that can calibrate the DC offsets of magnetic field measurements in situ (Broadfoot et al., 2022). Lastly, this algorithm was tested offline using a single thread on an Intel Core i7-1255U CPU, which has much higher computational power than a typical CubeSat platform. A possible solution is to redesign the components of WAIC-UP (wavelet transform, correlation, median filter, etc.) into streaming signal operations, so that the algorithm can run in real-time onboard a CubeSat for

operational purposes. This could be implemented on an FPGA or DSP microcontroller.

In this work, we developed a method for removing stray magnetic field interference from boomless spacecraft magnetometers. The WAIC-UP algorithm is an extension of an adaptive interference cancellation algorithm that can remove a single interference signal. WAIC-UP can remove interference in an underdetermined time-domain mixing system through taking a wavelet transformation. WAIC-UP performs similarly to UBSS, a leading interference removal algorithm. WAIC-UP also shows a very high correlation with the true magnetic field signal in many simulations. The WAIC-UP algorithm makes minimal assumptions about the stray magnetic field signals. The Monte Carlo simulations demonstrate that the algorithm can be applied to CubeSats with various interference sources, enabling low-cost boomless spacecraft for future space exploration.

4.5 Conclusion

This chapter investigated the effectiveness of the WAIC-UP algorithm, a new wavelet-based noise identification method, in removing stray magnetic field interference from boomless spacecraft magnetometer measurements. Our findings demonstrated that the WAIC-UP algorithm offers performance comparable to the state-of-the-art UBSS interference removal algorithm, with a twenty-fold reduction in execution time. In an experiment with three magnetometers and four interference signals, WAIC-UP achieved an increase in correlation from 0.6843 to 0.9993, an SNR improvement from -0.65 dB to 28.48 dB, and an RMSE reduction from 259.68 nT to 9.08 nT (near the normal noise floor of the instrument). Similarly, in an experiment with the Quad-Mag magnetometer and four interference signals, WAIC-UP yielded a correlation increase from 0.8075 to 0.9964, an SNR enhancement from 2.76 dB to 21.42 dB, and an RMSE reduction from 42.33 nT to 4.94 nT. These results highlight the significant improvements in magnetometer signal quality, which are crucial for various applications, including spacecraft navigation, attitude control, and space physics research.

In addition to conducting real-world experiments, we carried out over 1500 randomized simu-

lations to statistically evaluate the efficacy of the WAIC-UP algorithm. The results revealed that WAIC-UP provides a substantially better estimation than merely selecting the magnetometer signal with the minimum noise. The median correlation increased from 0.2468 to 0.9937, the median SNR improvement was from -12.39 dB to 14.21 dB, and the median RMSE reduction was from 26.31 nT to 11.33 nT. Furthermore, the performance of the WAIC-UP cleaned signal significantly outperformed the results obtained by simply averaging the magnetometer signals. When comparing the WAIC-UP signals to the averaged magnetometer signals on a simulation-by-simulation basis, WAIC-UP demonstrated a mean increase in SNR of Δ18.13 dB.

While the algorithm operates under certain assumptions that may limit its applicability, potential solutions and future research could address these limitations. Ultimately, WAIC-UP showcases its potential for application in CubeSats with diverse interference environments, facilitating the development of low-cost boomless spacecraft for future space exploration. The success of WAIC-UP in these experiments underscores its potential to facilitate more compact satellite designs, and represents a crucial step towards more efficient and cost-effective magnetometer designs for space missions.

CHAPTER 5

MAGPRIME: An Open-Source Library for Benchmarking and Developing Noise Removal Algorithms for Spaceborne Magnetometers

This chapter focuses on MAGPRIME (MAGnetic signal PRocessing, Interference Mitigation, and Enhancement), a comprehensive open-source Python library developed to enhance the accuracy of magnetometer readings in space physics. This chapter provides a detailed overview of existing methods for magnetometer interference removal and introduces MAGPRIME's functionalities and structure. The MAGPRIME library integrates various advanced noise removal algorithms, facilitating efficient and customized solutions for space scientists and engineers.

In this chapter, we also compare the efficacy of the suite of noise removal algorithms in MAGPRIME using two Monte Carlo benchmarking tests. The results show significant noise reduction for both traditional gradiometry configurations that use a boom and in non-conventional bus-mounted configurations. This chapter underscores the versatility of MAGPRIME in improving magnetic field measurements across different spacecraft configurations, including cost-effective CubeSats. The work in this chapter is in preparation for submission to the Journal of Geophysical Research: Machine Learning and Computation. The MAGPRIME library is accessible through github at https://github.com/aphoffmann/MAGPRIME.

5.1 Introduction

Space exploration missions often require magnetic field measurements, but these measurements can be distorted by stray magnetic fields generated by spacecraft electrical systems. This interference can come from various subsystems, such as reaction wheels, magnetorquers, propulsion systems, and others. One method to reduce stray magnetic field interference is to place the magnetometer on a long mechanical boom, so that the stray magnetic fields diminish with distance. However, this is not always effective, as many spacecraft still experience interference from different source even with a boom. For example, the InSight rover has a single magnetometer on a short boom and observes high-frequency noise associated with solar panel currents (Johnson et al., 2020). The DMSP F15 satellite has a 5-m boom and struggles with spacecraft noise (Kilcommons et al., 2017). The GOES-17 spacecraft has a 6 m boom but observes interference from arcjet activity and reaction wheels (Califf et al., 2020; Loto'aniu et al., 2019). Stray magnetic fields have been challenging spacecraft magnetometers since the first spaceflight magnetometer was launched in 1958 (Dolginov et al., 1961).

To mitigate the effects of stray magnetic field interference, two main methods have been developed over the years. The first method is magnetic cleanliness, which aims to minimize the generation of stray magnetic fields by modifying the electrical and mechanical design of the spacecraft (Ludlam et al., 2009; Lassakeur et al., 2020; Nikolopoulos et al., 2020). This can be done by using non-magnetic materials, running wires in twisted-pairs, minimizing current loops, and shielding high power instruments. However, magnetic cleanliness is not always feasible, especially for low cost or mass produced spacecraft such as CubeSats. The second method is gradiometry, which uses two or more magnetometers to estimate and remove the interference signals (Kivelson et al., 2023; Jo et al., 2023; Lee et al., 2023). Ness et al. (1971) proposed a gradiometry algorithm (denoted Ness) that assumes the spacecraft magnetic field as a dipole and removes it using the gradient between two magnetometers placed collinearly on a boom. This method requires a long enough boom for the dipole assumption to be valid, but can use a shorter boom if the spacecraft's magnetic field is well-characterized.

Several recent gradiometry algorithms have been developed to deal with more complex interference scenarios. Sheinker and Moldwin (2016) developed an adaptive algorithm (denoted Sheinker) that identifies the gain of the stray magnetic field between magnetometers through a machine learning technique, and subtracts the estimated field using that gain. This algorithm can handle both static and dynamic interference sources, and does not require prior knowledge of the field characteristics. Carter et al. (2016) developed an algorithm that switches between gradiometry or averaging depending on the ratio of stray magnetic field noise to intrinsic magnetometer noise. Constantinescu et al. (2020) developed the Principal Component Gradiometry (PiCoG) algorithm, which transforms the dual-magnetometer measurements into a new coordinate system derived from principle component analysis, and performs gradiometry along the direction of maximum-variance. This algorithm can effectively suppress interference, and can be applied to any number of magnetometers. Ream et al. (2021) developed a gradiometry algorithm (denoted Ream) that detects stray magnetic field signals by differencing the magnetometer measurements in the time-domain and suppressing them in the frequency-domain.

Without the use of a boom, simplifying approximations can not be made about the structure of the spacecraft's magnetic field, so removing the stray magnetic field noise becomes much more challenging. Several advanced methods have been proposed to address this issue, such as Independent Component Analysis (ICA), Multichannel Singular Spectrum Analysis (M-SSA), Underdetermined Blind Source Separation (UBSS), and Wavelet-based Adaptive Interference Cancellation for Underdetermined Platforms (WAIC-UP). These methods can separate noise signals from the natural magnetic field signal without prior knowledge of the noise characteristics, and can work with more than two magnetometers without requiring a boom for gradiometry. ICA is a technique that separates noise signals based on their statistical independence, but it can only handle a limited number of noise sources (Imajo et al., 2021). M-SSA is a technique that decomposes the signal components in the time domain, but it requires careful selection of the components to reconstruct the natural magnetic field signal (Finley et al., 2023). UBSS is a novel technique that exploits the multi-magnetometer configuration to identify noise signals using cluster analysis and applies

compressive sensing to separate the noise from the ambient magnetic field, however it is computationally complex and requires many specific parameters to be tuned (Hoffmann and Moldwin, 2022). The WAIC-UP algorithm exploits the distinct spectral properties of various interference signals to separate them from the ambient magnetic field in the wavelet domain (Hoffmann and Moldwin, 2023). WAIC-UP is efficient at cleaning high-frequency noise and orders of magnitude faster than UBSS, but it cannot clean lower frequency noise due to the nature of the wavelet transform. These algorithms are effective at cleaning bus-mounted magnetometer measurements as they can work with multiple magnetometers with minimal assumptions about the nature of the stray magnetic fields.

In this work, we introduce MAGPRIME, an open-source tool for magnetometer signal processing. MAGPRIME is a Python library that offers a variety of noise removal algorithms for magnetometer data. It aims to foster community-driven development of magnetometer noise removal applications and to support future spacecraft design. Additionally, this library enables the creation of simulations of distributed noise sources and magnetometers in various spacecraft layouts. We use the MAGPRIME library to compare several noise removal algorithms with Monte Carlo simulations. We consider two scenarios for the simulations. The first is the standard gradiometry case, where two magnetometers are mounted on a short boom. The second case is where three magnetometers are mounted on the spacecraft bus. The boomless configuration is a low cost alternative to typical gradiometry with a mechanical boom, but experiences significantly more stray magnetic field noise. We evaluate the performance of the MAGPRIME noise removal algorithms on highly broadband and complex magnetic field noise. MAGPRIME enhances space physics and spacecraft design research by offering advanced algorithms for stray magnetic field removal. Its ability to provide accurate magnetic field measurements is crucial for the success of in situ space science missions. In this work, we showcase MAGPRIME's effectiveness and highlight its potential for broad adoption in future space explorations.

5.2 Software Description

MAGPRIME is a Python package that offers a comprehensive set of noise removal algorithms for space-based magnetic field measurements. It is an open-source and community-based project that aims to enable the development and evaluation of new and existing methods for improving the quality and reliability of magnetometer data. The package is hosted on GitHub under the CC BY-NC 4.0 license and invites contributions from researchers in space sciences and engineering. The open-source nature of the project not only ensures collaborative development and transparency, but also aligns with the spirit of the NASA's Open Science Initiative (Gustetic et al., 2015).

The package provides the following functionality:

1. A collection of noise removal algorithms, such as WAIC-UP, UBSS, M-SSA, and others.

2. Example scripts and Jupyter notebooks to demonstrate the usage of the library and show the results of applying different algorithms to real and synthetic data sets.

3. Two benchmarks to evaluate the efficacy of each algorithm on different magnetometer configurations.

Figure 5.1 illustrates the structure of the Python package. The package consists of four main modules: algorithms, utilities, examples, and benchmarks. Each module contains files that implement the corresponding functionality. The package offers a user-friendly interface that allows users to easily import and use the algorithms on their data.

The package can be installed using pip or by cloning the repository and running setup.py or pip install. The package requires Python 3.9 or higher and depends on several external packages, such as numpy, scipy, matplotlib, etc. The package also includes detailed usage instructions and examples in the README file and the examples folder.

The following code snippet demonstrates how to import the 'magprime' library and use its noise removal algorithms on spacecraft magnetometer data. Some algorithms require detrending of the data. Therefore, each algorithm has parameters like uf and $detrend$, which are designed for this

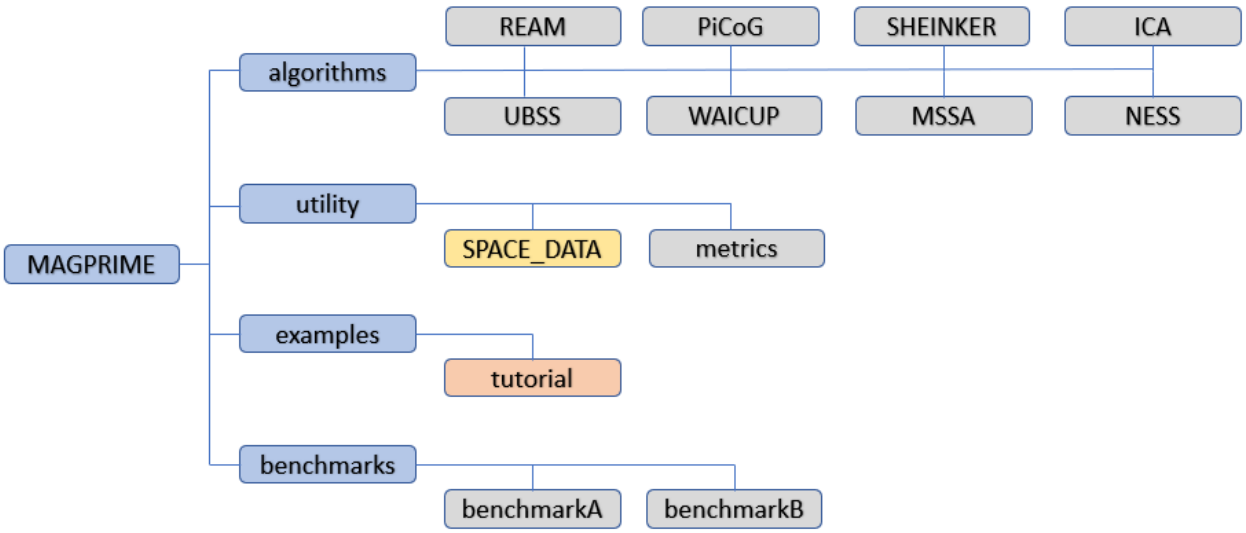

Figure 5.1: Overview of the functionality of the MAGPRIME Python library. Folders are shown in blue, files are shown in gray, data are shown in yellow, and Jupyter notebooks are in light orange.

purpose. The uf parameter specifies the number of data points to be used in a uniform filter, while the $detrend$ parameter is a boolean that indicates whether data detrending should be done or not. Here is an example of noise removal using the WAIC-UP algorithm:

Listing 5.1: Noise removal example using the WAIC-UP algorithm

```
from magprime.algorithms import WAICUP
from magprime import utility

"Load example data from Michibiki-1 Satelltie"
B = utility.load_example_data() # shape = (n_sensors, n_axes,
    n_samples)

"Detrend the data"
WAICUP.uf = 360 # n_samples to use in uniform filter
WAICUP.detrend = True

"Algorithm Parameters"
```

```
WAICUP.fs = 1  # Sample rate
WAICUP.dj = 1/12 # Wavelet Spacing

"Clean the data and store it in B_waicup"
B_waicup = WAICUP.clean(B, triaxial = True)
```

Each algorithm also has specific parameters that are unique to its functionality and can be defined by the user. For example, the WAIC-UP algorithm has the parameter, $WAICUP.dj$, that controls the resolution of its wavelet transformation. These algorithm-specific parameters are explained in detail in the tutorial notebook of the 'magprime' library. They can be accessed by using the help function, for example, $help(WAICUP)$.

Moreover, each algorithm has a clean() function that takes the noisy magnetic field data as input and returns the cleaned data as output. This is the function that intakes the noisy magnetometer data from multiple magnetometers and returns an individual, cleaned triaxial signal. Some algorithms are developed to work on only triaxial data, while others can clean both triaxial or single axis data. The $triaxial$ argument is used to specify whether the data are single axis or triaxial.

5.2.1 Software Applications

The 'magprime' library is designed to be both a research tool and a utility for magnetic noise removal from past and future satellite mission data sets. The library serves three key purposes in the field of space magnetism research:

1. It is a hub for the development of magnetic noise removal algorithms, providing several benchmarks that standardizes their comparison. This ensures that researchers can reliably select the most effective algorithm for specific noise conditions in magnetometer data.

2. It can be adapted for cleaning operational spacecraft magnetometer data, thereby enhancing the precision of magnetic field measurements collected during space missions.

3. It aids in the design phase of spacecraft by providing simulations to determine optimal magnetometer placement. For spacecraft that use booms, MAGPRIME can determine the minimum length of the boom to minimize the spacecraft's magnetic interference.

The 'magprime' library is an open-source project that encourages enhancement through its community-driven approach. It welcomes new algorithms and updates from contributors. By refining the quality of space-based magnetic field measurements, the library aims to support studying investigations of space magnetism throughout the heliosphere.

5.3 Methodology

Since the first spacecraft magnetometer flew in 1958, many noise removal algorithms have been created. These algorithms vary in their approach to different types of noise from DC offsets to higher frequency noise from subsystems such as reaction wheels. In the first part of this section, we review the methodology of several noise removal algorithms that are included in MAGPRIME. These algorithms are recreated from their original papers and are undergoing continuous development to improve their functionality. In the second part of this section, we describe the methods used to create the Monte Carlo simulations used to benchmark the algorithms. These simulations include a variety of simulated and real magnetometer noise.

5.3.1 Algorithms

5.3.1.1 Gradiometry

Ness et al. (1971) proposed the seminal algorithm for removing the magnetic noise caused by the spacecraft. The technique relies on two magnetometers mounted collinearly on a boom to measure the observed magnetic field at different distances from the spacecraft. The algorithm assumes that the spacecraft's magnetic field can be approximated by a single dipole field, and estimates its presence at each sensor. The coupling matrix, α, captures the relationship between the spacecraft's

field and the measurements at the two sensors. The algorithm then recovers the ambient magnetic field, B_{amb}^{est}, by using the following equation:

$$B_{amb}^{est} = \frac{B_{obs}(r_2) - \alpha B_{obs}(r_1)}{1 - \alpha} \tag{5.1}$$

In this system, $B_{obs}(r_2)$ and $B_{obs}(r_2)$ are the observed fields at the midpoint and the end of the boom, respectively. This gradiometry algorithm requires prior characterization of the spacecraft's magnetic field to obtain accurate values for the coupling matrix, α.

5.3.1.2 Frequency-Domain Gradiometry Filtering

Ream et al. (2021) introduced a new technique for removing stray magnetic fields generated by the spacecraft from the measurements of a magnetic gradiometer in the frequency domain. The technique applies a moving window to calculate the difference between the observed fields at two magnetometers on a boom, and uses two parameters, n and δb, to detect the intervals where the spacecraft fields are active. In those intervals, the technique analyzes the frequency spectra of the differenced field components and identifies the spectral peaks that correspond to the spacecraft fields. Those peaks are then automatically suppressed through reducing their amplitudes by a factor ranging from 20 to 100. The corrected frequency-domain signal is than inverted back into a time-series representing the ambient magnetic field signal.

The Ream method and the Ness method both use a magnetic gradiometer to eliminate spacecraft fields. However, the Ream technique works in the frequency domain while the Ness technique operates using spatial information. Additionally, the Ream method can handle multiple overlapping spacecraft fields, while the Ness method assumes a single multipolar field.

5.3.1.3 Principal-Component Gradiometry

The PiCoG algorithm is an advanced gradiometry technique used to remove stray magnetic field signals (Constantinescu et al., 2020). It works best with two or more magnetometers. Unlike the Ness et al. (1971) method, which assumes a specific magnetic field structure, PiCoG uses a differ-

ent approach. It finds the direction of maximum variance in the magnetometer data and applies a coordinate transform using Principal Component Analysis (PCA). The transformed magnetometer data is then used to estimate the coupling parameter, α. This estimation is achieved through the following equation:

$$\alpha = \sqrt{\frac{Var(B_x)}{Var(\Delta B_x)}} \tag{5.2}$$

In this equation, $Var(B_x)$, represents the variance of the magnetic field in the direction of maximum variance found through PCA, while $Var(\Delta B_x)$ denotes the variance of the differenced magnetometer signals along that axis.

Following the estimation of the coupling parameter from the magnetometer data in the transformed coordinate system, we can then proceed to recover the ambient magnetic field signal. This recovery is performed using the equation:

$$B'_k = B_k - \alpha(R)^{-1})_x(R\Delta B)_x \tag{5.3}$$

In this equation, $k \in (1, 2, 3)$ and R represents the transformation matrix.

The PiCoG algorithm can be applied iteratively to remove multiple disturbance sources using more than two sensors. This technique has been successfully implemented on board the Service Oriented Spacecraft Magnetometer instrument on the GEO-KOMPSAT-2A geostationary satellite, which delivers accurate magnetic field data in near-real time for space weather applications (Constantinescu et al., 2020).

5.3.1.4 Sheinker and Moldwin Gradiometry

Sheinker and Moldwin (2016) developed an adaptive gradiometry algorithm that does not make assumptions about the spacecraft magnetic field signal or the nature of the stray magnetic field noise itself. The algorithm assumes there is a single disturber signal, $a(n)$, interfering with the ambient magnetic field signal, $x(n)$. The mixing system is defined as:

$$\begin{cases} b_1(n) = x(n) + a(n) + w_1(n) \\ b_2(n) = x(n) + ka(n) + w_2(n) \end{cases} \tag{5.4}$$

Where $b(n)$ are the magnetometer signals and $w(n)$ is the intrinsic noise of each magnetometer. The Sheinker and Moldwin (2016) method estimates the coupling coefficient $\hat{k}$ by correlating the differences between the two magnetometer signals. After $\hat{k}$ is estimated, the ambient magnetic field $x(n)$ can be restored as:

$$x(n) = \frac{\hat{k}b_1(n) - b_2(n)}{\hat{k} - 1} \tag{5.5}$$

This method does not assume anything about the stray field characteristics. However, it assumes there is only one interference source, which works well when the spacecraft field can be modeled as a single dipolar noise signal with one coupling coefficient. The method fails to remove multiple noise signals when that assumption is invalid.

5.3.1.5 Independent Component Analysis

Imajo et al. (2021) introduced an application of ICA to mitigate spacecraft noise in the magnetometer data collected from the Michibiki-1 satellite. ICA is an algorithm designed to separate signals based on their statistical independence. This algorithm operates under the assumption of a mixing system, where the magnetometer measurements, b, are considered a linear combination of source signals, s, as described by the following system:

$$b = Ks \tag{5.6}$$

In this equation, the matrix K represents the mixing matrix, which specifies how each source signal contributes to each magnetometer's measurements. Through a series of iterative steps leveraging relationships between statistical independence, entropy, and Gaussian distributions, ICA

seeks to find a set of vectors, W. These vectors are used to project b into a space that maximizes the non-Gaussianity of $W^T b$. The matrix, W, can be inverted to find the original mixing matrix, K (Hyvärinen and Oja, 2000).

It is important to note that the ICA algorithm has several limiting assumptions. It is a determined algorithm, meaning it cannot isolate more signals than there are measurement channels available. Additionally, the efficacy of ICA is data-dependent, necessitating that the source signals are independent and non-Gaussian.

5.3.1.6 Multichannel Singular Spectrum Analysis

Finley et al. (2023) applied M-SSA to distinguish stray magnetic field noise from geophysical magnetic field signals. Singular Spectrum Analysis (SSA) is a method designed to deconstruct time-series signals into their statistically meaningful components. M-SSA is an extension of SSA tailored to handle data from multiple measurement channels. This method involves a several-step algorithm that starts with the formulation of the trajectory matrix, denoted as X from the noisy magnetometer data.

$$X = \begin{bmatrix} x_m(1) & x_m(2) & x_m(3) & \dots & x_m(K) \\ x_m(2) & x_m(3) & x_m(5) & \dots & x_m(K+1) \\ x_m(3) & x_m(4) & x_m(6) & \dots & x_m(K+2) \\ \vdots & \vdots & \vdots & \ddots & \vdots \\ x_m(L) & x_m(L+1) & x_m(L+2) & \dots & x_m(N) \end{bmatrix} \tag{5.7}$$

In this equation, the L number of rows represent K-length lagged versions of the magnetometer signal, $x(n)$, that is of length N. The subscript, m, denotes the magnetometer. The trajectory matrix is used to define the Lag-Covariance matrix, C, such that.

$$C = \frac{1}{K} X^T X \tag{5.8}$$

The statistically significant signal components can be found from the lag-covariance matrix

through taking an eigandecomposition of C. Finley et al. (2023) adds an additional step to identify noise signals through the correlation of the signals with the difference between the magnetometer measurements. M-SSA is a computationally expensive algorithm and relies on an approximation of the magnetometer noise to distinguish geophysical signals that may not always be valid. For instance, if a stray magnetic field signal is nearly equal in magnitude at each magnetometer, it would have minimal presence in the differenced measurements, potentially leading to its misidentification as a natural signal.

5.3.1.7 Underdetermined Blind Source Separation

The UBSS algorithm is well-known in the fields of radar and acoustic signal processing. Hoffmann and Moldwin (2021) developed UBSS to separate stray magnetic field noise from natural magnetic field signals. The UBSS algorithm models the system of magnetometers and source signals with the following equation:

$$B = KS \tag{5.9}$$

Where B is a vector of m mixed magnetometer measurements, S is a vector of n source signals such that $m < n$, and K is the underdetermined mixing matrix that defines the contribution of each source signal to each magnetometer.

The UBSS algorithm implemented by Hoffmann and Moldwin (2022) is a two-step process. First, it identifies the noise signals through cluster analysis. Second, it separates the noise signals through compressive sensing. The UBSS algorithm makes no assumptions about the magnitude, location, or characteristics of the noise signals, except that they are sparse in the time-frequency domain. The use of compressive sensing makes UBSS computationally expensive, although this algorithm can be parallelized.

5.3.1.8 Wavelet-Adaptive Interference Cancellation for Underdetermined Platforms

The WAIC-UP algorithm is an extension of the algorithm by Sheinker and Moldwin (2016) to the wavelet domain. Hoffmann and Moldwin (2023) apply WAIC-UP by linearly transforming the mixed magnetometer measurements via a wavelet transform. The Sheinker and Moldwin (2016) algorithm is applied to each wavelet-scale to remove stray magnetic field noise. However, due to the shrinking cone of influence, the wavelet transform is not valid at lower frequencies, and WAIC-UP can not be applied. This makes the WAIC-UP algorithm a high-frequency noise removal algorithm. One positive aspect of WAIC-UP is that it is incredibly fast compared to UBSS and M-SSA, and has the potential for real time noise removal.

5.3.2 Benchmarks and Metrics

In this work, we evaluate the performance of algorithms in the MAGPRIME library using two benchmarks. The benchmarks are designed to facilitate the comparison of current and future noise removal algorithms. The benchmarks consist of Monte Carlo simulations of stray magnetic field noise in a 3U CubeSat (10 cm x 10 cm x 30 cm) volume. MAGPRIME is designed to work in tandem with the Magpylib library to simulate magnetic fields. Magpylib is used to create current loops that generate the stray magnetic fielda. Previous work by Boschetti et al. (2012) used a similar approach to evaluate the worst case magnetic field of the Gravity Field and Steady-State Ocean Circulation Explorer (GOCE) satellite. Additionally, Park et al. (2022) used Magpylib to evaluate the magnetic cleanliness of the Korean Pathfinder Lunar Orbiter (KPLO) satellite. In this work we simulate both AC and DC noise, but do not take any conductive materials into account.

The first benchmark, denoted Benchmark A, simulates a traditional gradiometry configuration, which is commonly used by modern spacecraft that rely on magnetometer measurements (Auster et al., 2008; Kivelson et al., 2023; Kilcommons et al., 2017; Broadfoot et al., 2022). In this benchmark, we place one virtual magnetometer at the end of a 30 cm boom, and another one at the base of the boom. The boom extends from the end of the CubeSat, making the total length 60 cm. We sample each of the virtual magnetometers at 50 Hz for 100 seconds with 64-bit float precision and

no additional intrinsic measurement noise.

In the second benchmark, denoted Benchmark B, we evaluate the performance of the magnetometers in a boomless configuration. The three virtual magnetometers are mounted on the bottom, top, and midsection of the bus of the CubeSat, sampled at 50 Hz for a 100-second window. While this boomless configuration has not been flown before, advancements in noise removal algorithms, as explored in works like Strabel et al. (2022) and Hoffmann et al. (2023), are expected to reduce the reliance on mechanical booms and lower the cost, risk, and complexity of magnetic field measurements in space. In each simulation, the noise source locations are randomized, maintaining a minimum distance of 1 cm from the bus-mounted magnetometers. An example configuration of the magnetometers, noise generators, and stray magnetic field structure for each benchmark is illustrated in Figure 5.2.

The stray magnetic field signals in our simulations are generated using four current loops. The current loops have large magnetic moments that create a field strength of approximately 40,000 nT at a distance of 1 cm from each loop. For context, this level of magnetic field strength exceeds the 7500 nT peak-to-peak stray magnetic field noise observed by the Ex Alta-1 CubeSat when its magnetometer was stowed, illustrating that our simulations operate within a realistic parameter space for bus-mounted magnetometers (Miles et al., 2016).

The four noise sources consist of real noise from the Michibiki-1 satellite, simulated reaction wheel noise with a shifting frequency, simulated arcjet noise, and a sawtooth signal with a frequency of 3 Hz that turns on and off randomly. The real stray magnetic field was a 24-hour sample of interference taken from the Michibiki-1 magnetometers on April 23rd, 2012 (Imajo et al., 2021). The interference was calculated using difference between the inboard and outboard magnetometers to remove the ambient magnetic field signal. The Michibiki-1 noise is a 1 Hz signal that was randomized by selecting a random 5000 data point slice. This method shifts the frequency of the Michibiki-1 noise, but preserves the spectral content of the original signal at a shifted frequency. The simulated arcjet noise is based of observations by Califf et al. (2020). The arcjet signal is created by randomly turning on and off a binary signal with constraints placed on the duration to make

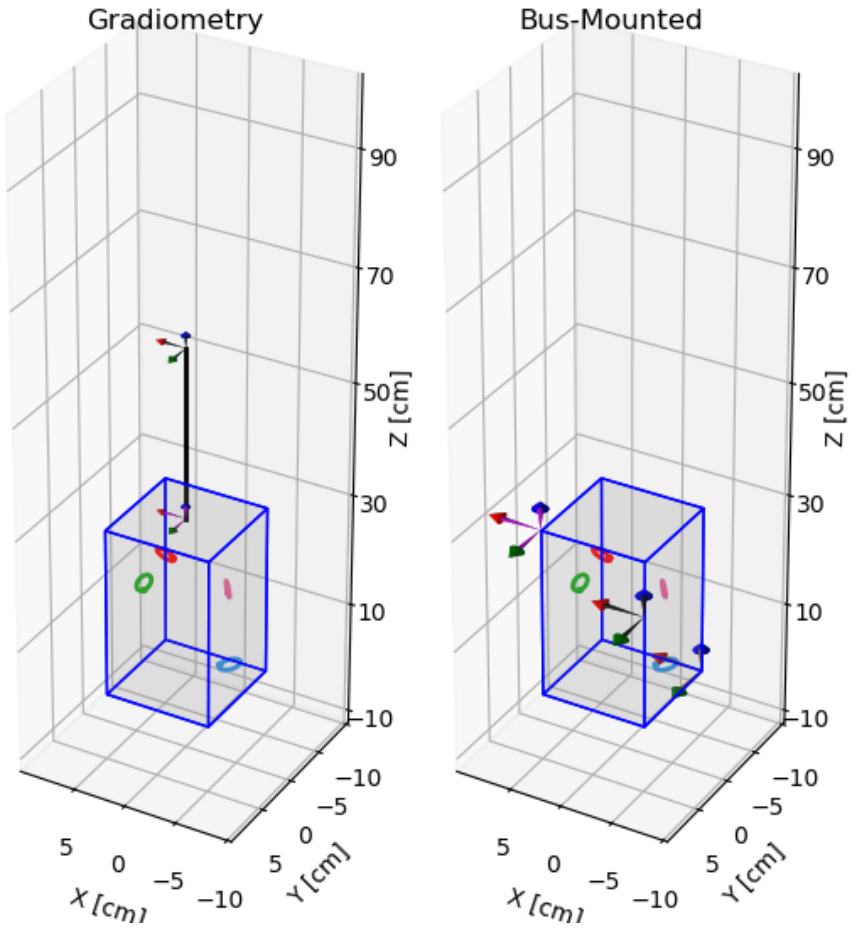

Figure 5.2: Visualization of CubeSat magnetometer configurations for magnetic field measurement benchmarks with magnetometers as tricolor vectors and dipole noise sources shown as current loops. Benchmark A, on the left, employs a traditional gradiometry setup with a 30 cm boom with virtual magnetometers sampled at 50 Hz over 100 seconds located at (0, 0, 30) cm and (0, 0, 60) cm from the CubeSat's origin at (0,0,0). Benchmark B, on the right, shows a boomless configuration with virtual magnetometers mounted directly on the CubeSat's bus at coordinates (5, 5, 30) cm, (-5, 5, 20) cm, and (-5, -5, 0) cm. All noise sources are placed at least 1 cm away from the nearest magnetometer.

it resemble a true arcjet. The reaction wheel noise consists of a sine wave that shifts down to a random frequency using a chirp signal, and returns to the same fundamental frequency (Loto'aniu et al., 2019). This resembles an attitude determination maneuver of a spacecraft where the angular momentum of the reaction wheels is used to modulate the spacecrafts orientation. These four signals represent a variety of noise sources that a spacecraft might produce. Additionally, their spectral content is incredibly broadband, so that their combination creates a very pathological case

for the application of noise removal algorithms.

Finally, the overarching goal of these benchmarks is to evaluate the ability of algorithms to separate ambient magnetic field signals from stray magnetic field noise. To simulate a realistic ambient signal, we use real-world magnetometer data from the Swarm A spacecraft (Friis-Christensen et al., 2008). Specifically, we selected a 50 Hz geomagnetic perturbation signal recorded on March 17, 2015 between 8:53 and 8:55 UTC. During this window, Swarm A was flying above Earth's southern auroral zone between the 69th and 76th southern latitude parallel. This auroral magnetometer data provides a complex natural ambient signal on top of which we can overlay the simulated spacecraft noise sources.

By benchmarking algorithms on this combined ambient and stray field data, we can quantify the ability to recover the underlying ambient signal in a realistic noise environment. Example spectra for the four randomized source signals used in this experiment and the ambient magnetic field signal from Swarm A are shown in Figure 5.3

To quantify the performance of algorithms for separating ambient and stray magnetic field signals, we employ three distinct metrics: Pearson correlation coefficient, root mean square error (RMSE), and signal-to-noise ratio (SNR).

The Pearson correlation coefficient, calculated as per Equation (5.10), measures the similarity between the cleaned signal (y_i) and the true ambient magnetic field (x_i). Correlation excels at measuring the removal of variable stray magnetic field signals because it is detrended in its calculation, where $\bar{x}$ and $\bar{y}$ are the means of true and estimated signals, and n is the number of data points.

$$\rho = \frac{\sum_{i=1}^{n}(x_i - \bar{x})(y_i - \bar{y})}{\sqrt{\sum_{i=1}^{n}(x_i - \bar{x})^2}\sqrt{\sum_{i=1}^{n}(y_i - \bar{y})^2}} \tag{5.10}$$

RMSE, defined in Equation (5.11), quantifies the absolute error between the processed signal (y_i) and the true ambient field (x_i), offering a direct measure of the algorithm's accuracy.

$$\text{RMSE (nT)} = \sqrt{\frac{\sum_{i=1}^{n}(x_i - y_i)^2}{n}} \tag{5.11}$$

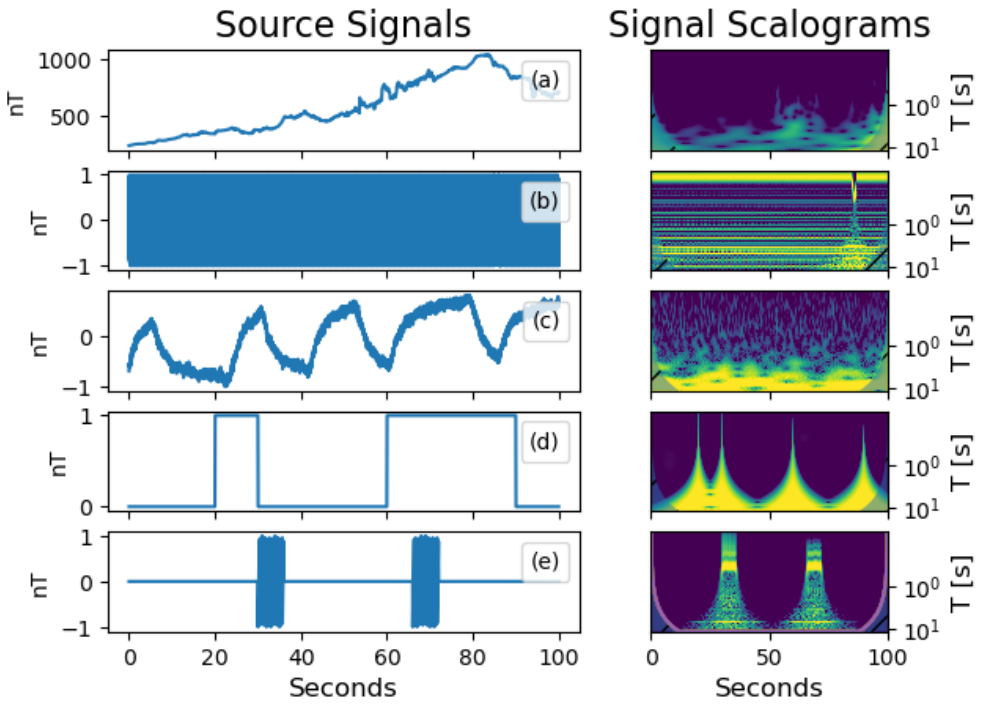

Figure 5.3: Five source signals sampled at 50 Hz. Panel (a) shows the natural magnetic field signal taken from the Swarm A Spacecraft on March 17th, 2015. Panel (b) shows the simulated reaction wheel noise with a shifting frequency. Panel (c) shows the real noise from the Michibiki-1 satellite. Panel (d) shows the simulated arcjet noise. Panel (e) shows the sawtooth signal with a frequency of 3 Hz that turns on and off randomly. Each time series signal except for the ambient magnetic field signal is normalized. The second column shows the wavelet scalogram of each source signal. The y-axis is the period of the signal in seconds. The coloring shows the normalized amplitude of the detrended signals.

Lastly, SNR, as described in Equation (5.12), compares the power of the remaining ambient signal (x_i) to the noise level in the cleaned signal, providing insight into the relative error and the efficacy of the algorithm in preserving the true signal. Here, $\bar{x}$ is the mean of the true ambient signal values, and n is the number of data points.

$$\text{SNR (dB)} = 10 \log_{10} \frac{\sum_{i=1}^{n} (x_i - \bar{x})^2}{\sum_{i=1}^{n} (x_i - y_i)^2} \tag{5.12}$$

5.4 Results

In this chapter, we rigorously assess the capabilities of eight unique algorithms from the MAG-PRIME library, targeting their performance in filtering noise from triaxial magnetometer data. Utilizing Monte Carlo simulations, we simulate two distinct magnetometer configurations, dual magnetometer gradiometry and a novel three magnetometer boomless setup, as outlined in section 5.3.2. Each configuration was subjected 100 simulations, yielding a dataset that enabled us to conduct an extensive and detailed statistical analysis of the algorithms' efficacy under diverse and challenging conditions. The simulations were randomized through randomly placing and orienting the noise soures, as well as randomizing the content of the noise signals. Several algorithms are computationally expensive, so these simulations were run on the University of Michigan's Great Lakes high performance computing cluster.

The results are structured to first present a detailed analysis of each algorithm's performance under the gradiometry setup (Benchmark A), followed by their performance in the boomless configuration (Benchmark B). Within each section, we explore the algorithms' effectiveness using metrics described in section 5.3.2. This structured presentation allows for a clear and comparative understanding of each algorithm's strengths and limitations in different scenarios. This section will delve into the specifics of these results, offering insights into the performance of each algorithm under varying conditions and their potential applicability in real-world space physics scenarios.

In the simulations, the ICA, WAIC-UP and M-SSA algorithms were detrended with a uniform filter of N=500 data points before being applied to remove stray magnetic field signals as outlined in their respective literature (Finley et al., 2023; Imajo et al., 2021; Hoffmann and Moldwin, 2023). It is important to note that the parameters of these algorithms were not individually optimized for each simulation, so randomized testing may not provide a clear understanding of their performance when manually tuned to a spacecraft. However, the coupling coefficients for the Ness et al. (1971) algorithm were precisely calculated from the simulated magnetic field, offering a potentially more accurate estimation than typical laboratory characterizations.

5.4.1 Benchmark A: Gradiometry Configuration

Benchmark A evaluates the noise removal algorithms in a 3U CubeSat context, featuring a dual-magnetometer setup with one sensor on the end of a 30 cm boom and another at the boom's base. Within the CubeSat's confines, four dipole noise sources are randomly placed, requiring a minimum distance of 1 cm from the base-mounted magnetometer. The plot in Figure 5.4 depicts the composite ambient and stray magnetic field signals recorded at the boom's base for one of the simulation runs. Each panel illustrates the respective x-axis, y-axis, and z-axis mixed signals in blue, overlayed with the true magnetic field signal in orange. The data prominently features high-frequency oscillations from reaction-wheel noise from 10 to 20 seconds, alongside a strong square wave pattern from 20 to 30 seconds and 60 to 90 seconds, which mimics the noise signature of GOES-16 arcjet firing (Carter et al., 2016; Califf et al., 2020).

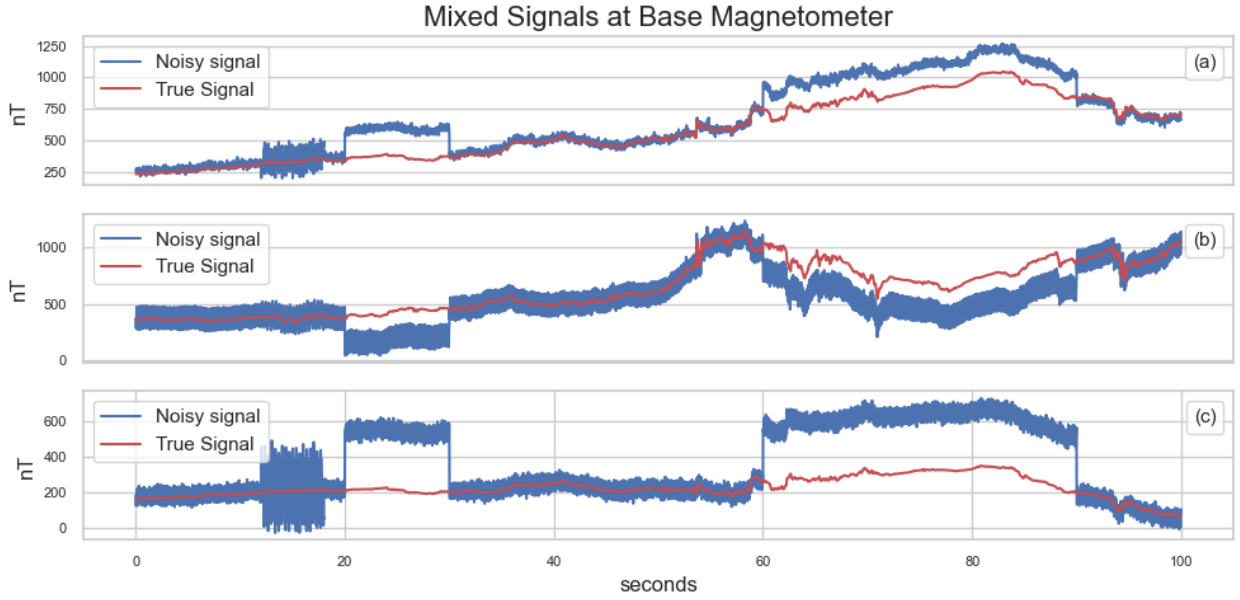

Figure 5.4: Mixed ambient and stray magnetic field signals over a 100-second interval from the magnetometer at the base of the 3U CubeSat gradiometry configuration. Panels (a), (b), and (c) represent the mixed signals for the x-axis, y-axis, and z-axis, respectively, with the noisy signals displayed in blue and the true ambient magnetic fields overlaid in orange. The limits of the y-scale in each panel is adjusted to the size of the signal.

Figure 5.5 shows the noisy magnetometer measurements from the same simulation as in Figure 5.4 as seen at the end of the boom. The magnitude of the noise sources at the end of the

boom are reduced to about 20 nT peak to peak from hundreds of nanoTeslas observed at the base. This notable attenuation of noise underscores the efficacy of the boom placement in mitigating electromagnetic interference without the use of any noise removal.

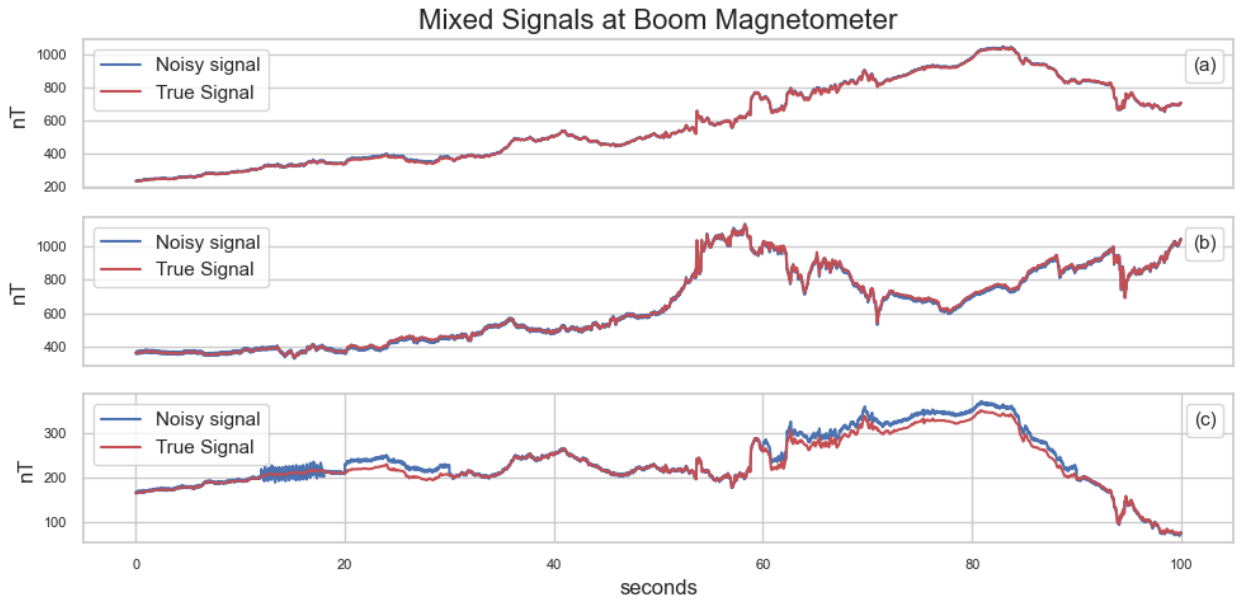

Figure 5.5: Mixed ambient and stray magnetic field signals over a 100-second interval from the magnetometer at the end of the boom in the 3U CubeSat gradiometry configuration. Panels (a), (b), and (c) represent the mixed signals for the x-axis, y-axis, and z-axis, respectively, with the noisy signals displayed in blue and the true ambient magnetic fields overlaid in orange. The limits of the y-scale in each panel is adjusted to the size of the signal.

Figure 5.6 presents the RMSE distributions from the z-axis signals processed by each MAG-PRIME algorithm, alongside the base and boom magnetometers' RMSE for a comparative baseline without any cleaning applied. Notably, the boom-mounted magnetometer exhibited exceptionally low RMSE values even in the absence of a cleaning algorithm, underscoring its inherent noise reduction capability due to its positioning. The base magnetometer's median RMSE was approximately 1400 nT while the boom's median RMSE was close to 14 nT. The UBSS and Ness algorithms surpassed the boom magnetometer's performance, each achieving a median RMSE that was nearly 11 nT.

However, since the M-SSA, ICA, and WAIC-UP detrend the signals before noise removal, metrics such as RMSE and SNR might not fully capture their capability. These algorithms excel

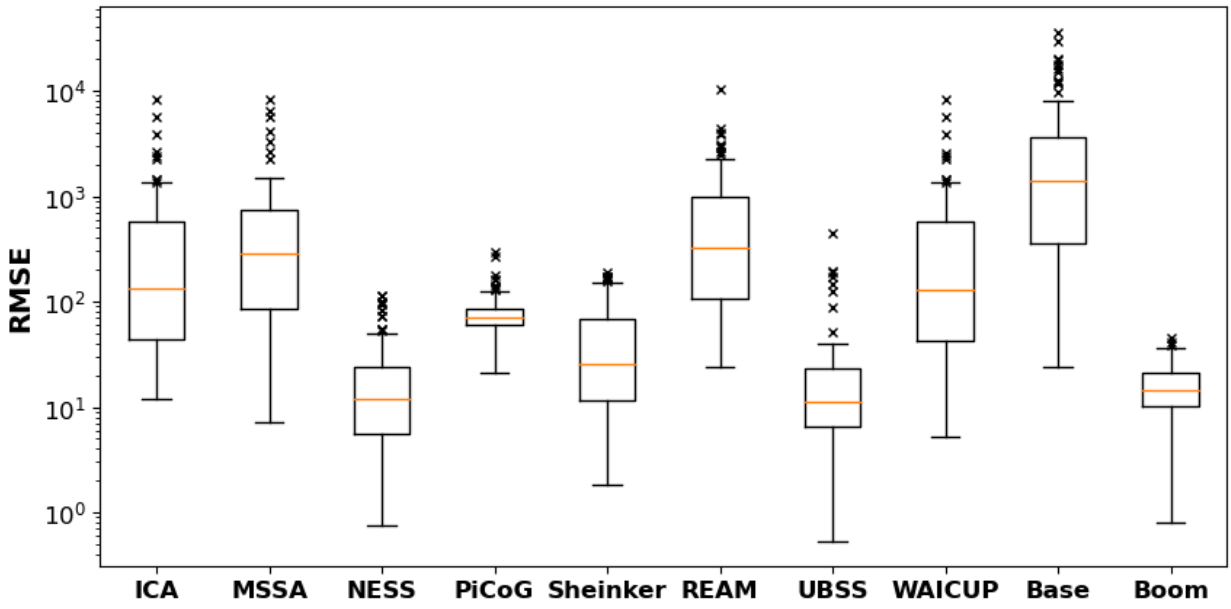

Figure 5.6: A box and whisker plot illustrating the RMSE for each MAGPRIME algorithm evaluated on the z-axis signals. The plot also includes the RMSE for the boom and base magnetometers to serve as benchmarks. The results highlight the superior noise reduction performance of the UBSS and Ness algorithms, which outperformed the naturally lower error levels of the boom-mounted magnetometer.

at mitigating higher frequency noise, however, lower frequency noise can be reintroduced after retrending the data. In this case, the correlation coefficient becomes a more accurate indicator of their performance because it removes the mean of each signal in its calculation.

The processed x-axis and y-axis signals from ICA, M-SSA, Ness, Sheinker, UBSS, and WAIC-UP exhibit median correlations exceeding 0.8. However, as shown in Figure 5.7, only the Sheinker, UBSS, and Ness algorithms acheive a correlation above 0.9 in the z-axis. This indicates that ICA, M-SSA, Sheinker, and WAIC-UP are particularly effective in reconstructing variable magnetic field signals. Notably, the unprocessed boom magnetometer data achieved an almost perfect correlation of 0.95. This level of correlation was only matched by UBSS and Ness, underscoring their superior ability to filter both DC and AC noise in gradiometry setups with broadband interference.

Next, we evaluated the full vector SNR for each algorithm's processed signal. The SNR, a critical metric that quantifies the power ratio of the ambient magnetic field signal to the stray

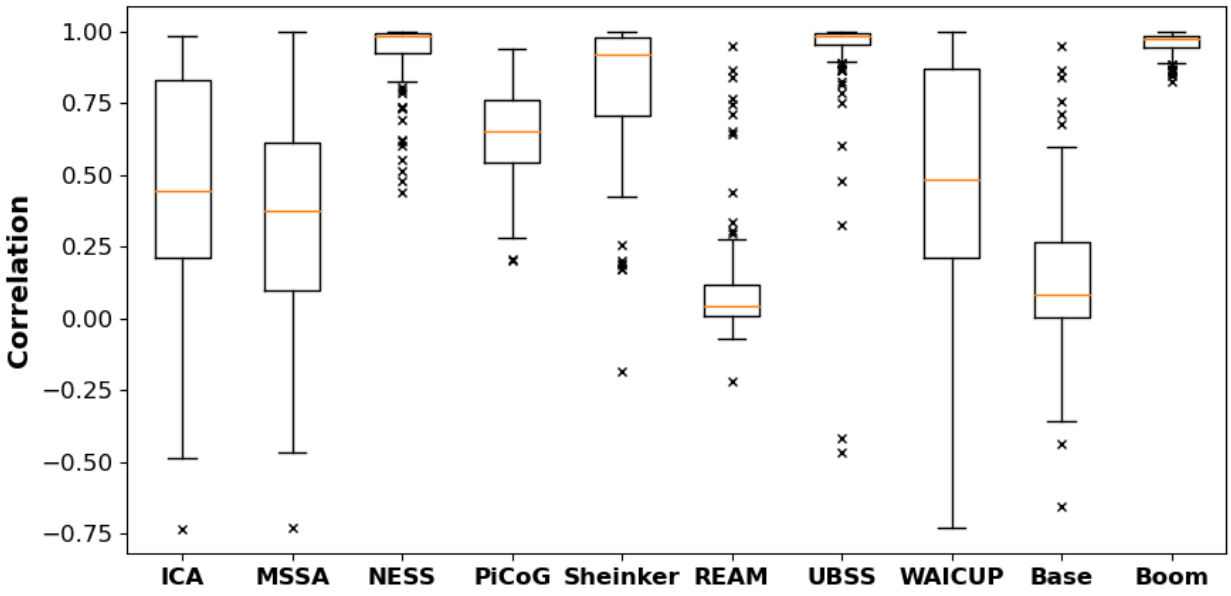

Figure 5.7: Distribution of correlation coefficients for the z-axis signals processed by MAGPRIME algorithms, compared with unprocessed signals from the boom and base magnetometers. High correlation values indicate effective noise removal, with ICA, M-SSA, Sheinker, and WAIC-UP showing strong performance. The boom magnetometer's baseline correlation is nearly perfect, with only UBSS and Ness achieving comparable results

magnetic field signal, indicates the algorithm's effectiveness in enhancing the true signal while suppressing noise. Figure 5.8 displays the SNR values' probability density functions for the x, y, and z-axis signals processed by each algorithm. This visualization allows for a comparison of each algorithm's noise reduction capabilities and their performance consistency across different axes in a gradiometry configuration.

The data illustrated in Figure 5.8 showcases the impressive performance of the boom magnetometer, which achieves median SNRs of 30.18 dB, 30.48 dB, and 12.12 dB for the x, y, and z-axes, respectively. The standard deviation for each axis is about 5 dB. While UBSS excels over the boom in median SNR on the x and z axes, it exhibits a wider standard deviation, close to 10 dB. Ness, on the other hand, slightly surpasses the boom magnetometer in terms of SNR across all axes but has marginally larger standard deviations compared to UBSS. The other algorithms assessed fall short of the boom magnetometer's SNRs. These outcomes indicate that the use of a short boom

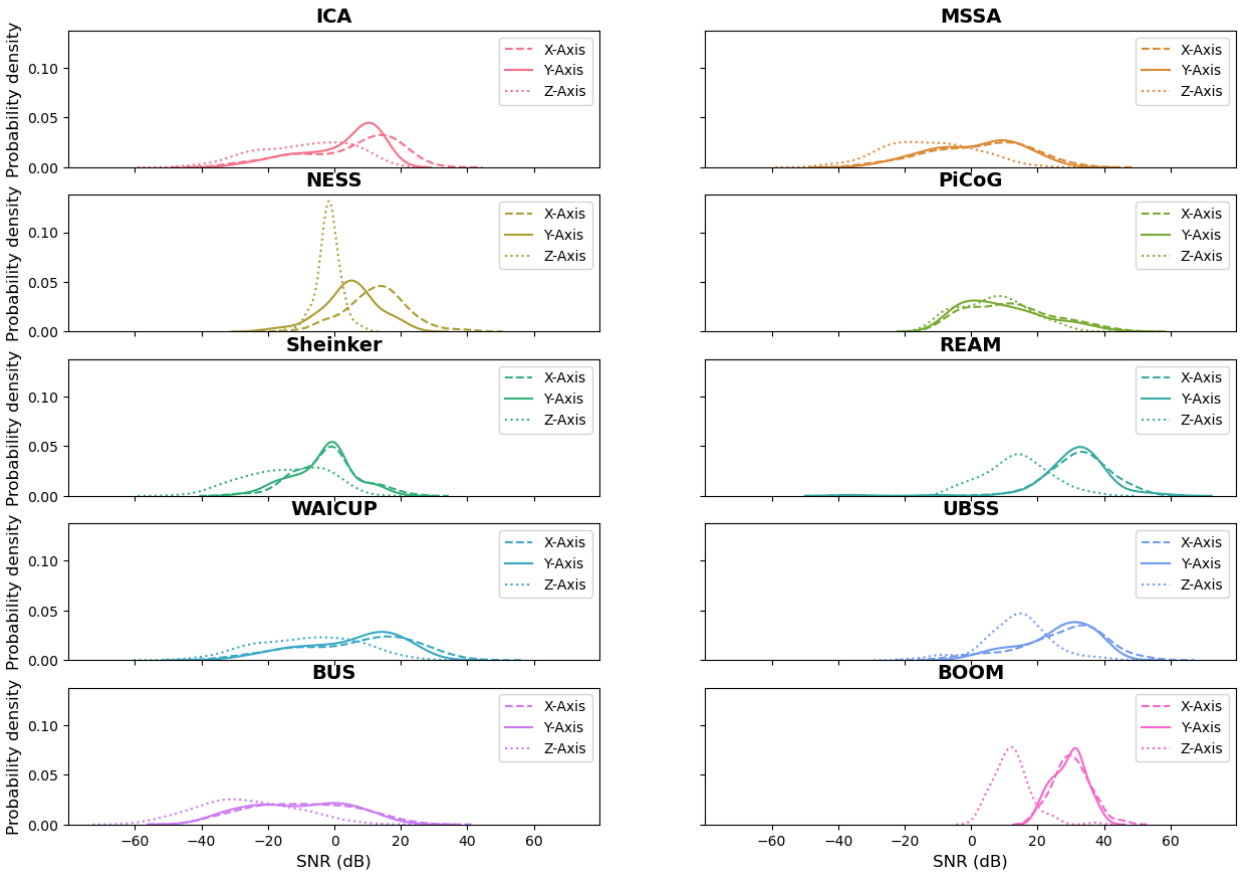

Figure 5.8: Probability density functions of the SNR values for each axis of each algorithm in the gradiometry configuration. Each subplot corresponds to a different algorithm, with the SNR distribution for the x, y, and z axes displayed in dashed, solid and dotted lines respectively.

on a 3U CubeSat can provide remarkably clean magnetometer data, assuming the CubeSat has a sufficiently minimized magnetic moment. UBSS and Ness generally outperform or match the boom magnetometer's cleaning efficacy, with the exception of the UBSS's x-axis signal, which has a slightly elevated RMSE and a lower SNR compared to the boom magnetometer. Table 5.1 presents the median tri-axial results of each metric for each algorithm, providing a comprehensive view of their performance.

Table 5.1: Median Results for Gradiometry Configuration

Metric		ICA	MSSA	NESS	Picog	Sheinker	Ream	UBSS	WAIC-UP	Base	Boom
RMSE	X	81.53	136.37	5.45	52.79	66.41	259.69	7.25	77.38	773.30	7.47
	Y	94.20	133.80	5.49	128.85	94.80	247.05	8.41	72.38	720.81	6.74
	Z	131.91	288.11	11.97	69.97	25.85	322.21	11.29	130.64	1389.38	14.42
Corr	X	0.9662	0.8909	0.9998	0.9823	0.9617	0.0988	0.9997	0.9753	0.4077	0.9996
	Y	0.9302	0.8878	0.9997	0.9048	0.9235	0.1419	0.9995	0.9664	0.4597	0.9996
	Z	0.4450	0.3769	0.9827	0.6533	0.9176	0.0416	0.9854	0.4859	0.0833	0.9738
SNR	X	9.41	4.95	32.92	13.19	11.20	-0.65	30.43	9.87	-10.13	30.18
	Y	7.57	4.52	32.25	4.85	7.51	-0.81	28.55	9.86	-10.11	30.48
	Z	-7.11	-13.89	13.74	-1.61	7.05	-14.87	14.24	-7.02	-27.56	12.12

5.4.2 Benchmark B: Boomless Configuration

In Benchmark B, we focus on evaluating noise removal algorithms in a boomless magnetometer setup for CubeSats, a potential cost-effective alternative to traditional designs (Strabel et al., 2022). This setup comprises three virtual magnetometers, M1, M2, and M3, located at the top, middle, and bottom of the CubeSat's bus. The boomless approach simplifies the CubeSat's structure and aims to reduce costs in space-based magnetic field measurements.

Figure 5.9 presents the time series signals from the M1 magnetometer at the CubeSat's top. These signals combine ambient and stray magnetic fields, providing raw data for algorithmic processing to discern the true magnetic field. The algorithms' effectiveness in this boomless context will inform the feasibility of such designs in future CubeSat missions. However, the presence of broadband and random normal noise in these signals presents a potentially more challenging environment than typical operational scenarios.

We applied each noise removal algorithm to the noisy magnetometer data shown in Figure 5.9, along with data from 99 additional randomized simulations. The resulting RMSEs for the z-axis signals in the boomless configuration are depicted in Figure 5.10 through a box and whisker plot. Algorithms such as Ness, Sheinker, Ream, and PiCoG, which are specifically designed for dual-magnetometer setups, were implemented using data from only the top (M1) and middle (M2) magnetometers.

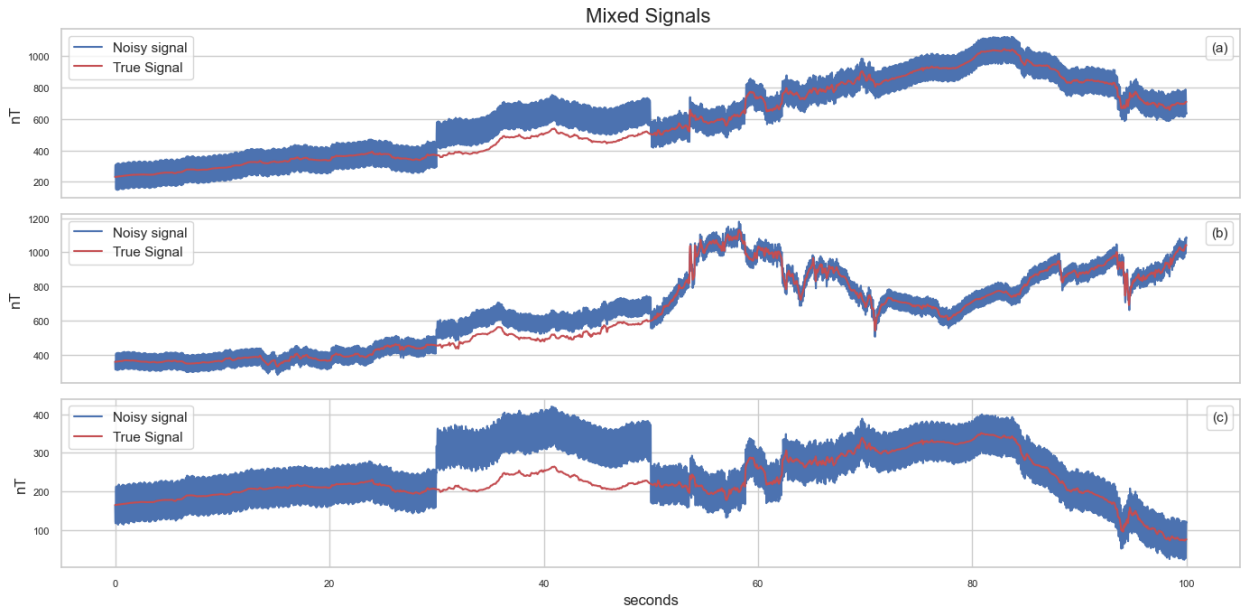

Figure 5.9: Time series representation of noisy signals captured by the virtual magnetometers in the boomless CubeSat configuration. This figure illustrates the complexity of the ambient and stray magnetic fields the algorithms are tasked to decipher. This benchmark serves as a basis for evaluating the algorithms' proficiency in a simulated worst-case noise scenario. The limits of the y-scale in each panel is adjusted to the size of the signal.

The results in Figure 5.10 show that UBSS had the greatest reduction in median RMSE down to 12 nT. UBSS leads every other algorithm with the lowest median RMSE and 25th percentile RMSE below 10 nT. WAIC-UP had the next lowest median RMSE of 17 nT followed by M-SSA. Other algorithms display higher RMSE values compared to the least noisy magnetometer (M1).

Figure 5.11 shows the correlation of each of the algorithms cleaned z-axis signal with the ambient magnetic field signal. ICA, M-SSA, and WAIC-UP each show correlation above 0.9 with a very small interquartile range. This indicates that they are very consistent at recovering the variable magnetic field signal. However, similar to Benchmark A, each of these algorithms had a high RMSE which suggests that the retrending process adds a DC offset to the cleaned signals. UBSS stands out with the highest median correlation of 0.98, and the smallest interquartile range.

Figure 5.12 presents the distribution of SNR values for each axis, measured by the algorithms in the boomless setup. ICA and WAIC-UP show particularly narrow distributions, signaling their ability to consistently achieve similar SNRs across multiple simulations. In the z-axis, UBSS and

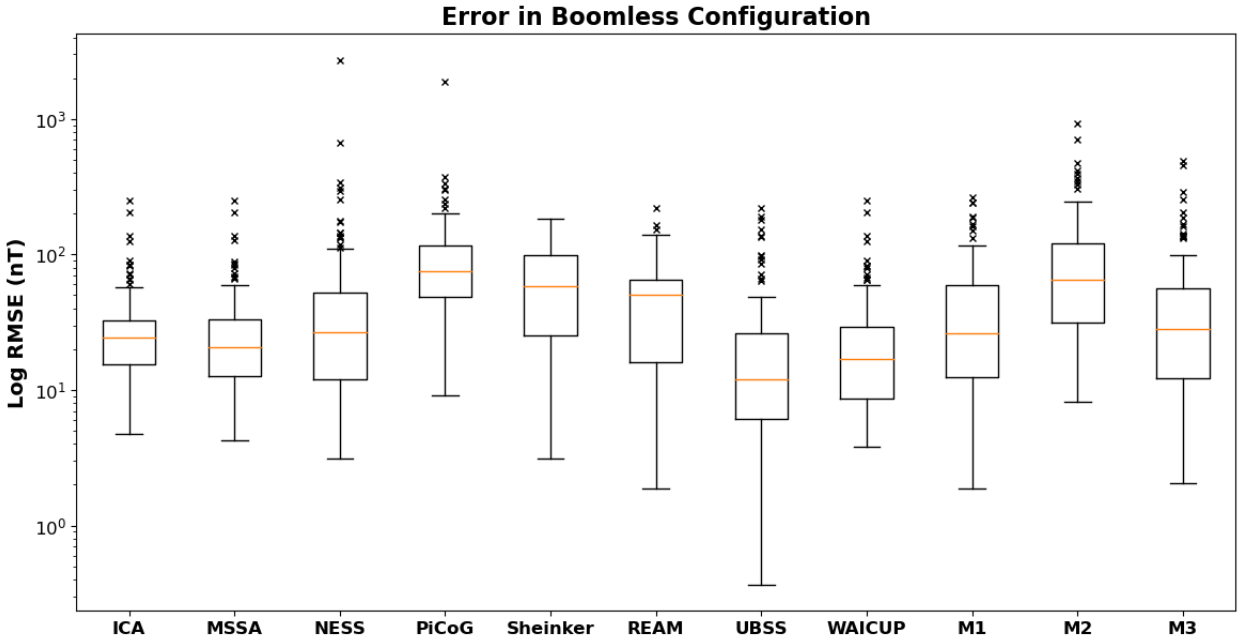

Figure 5.10: Distribution of the z-axis RMSE values for the cleaned signals from each noise removal algorithm tested in the boomless CubeSat configuration. The M1, M2, and M3 magnetometers show the raw RMSE of the top, middle, and bottom magnetometers respectively. The RMSE is shown in log scale to accentuate the difference between results.

WAIC-UP stand out achieved the highest SNRs of 13.76 dB and 10.67 dB, respectively, which markedly exceeds the SNR of uncleaned signals that range from 0 to 7 dB per axis. This superior performance of UBSS and WAIC-UP demonstrates their effectiveness in enhancing signal clarity in the boomless configuration. M-SSA also performed commendably, registering marginally higher SNRs than the least noisy magnetometer in two axes, while ICA did so in one axis. Conversely, Ness, Sheinker, and Ream algorithms exhibit distributions that align closely or fall short of the SNR levels of the least noisy magnetometer. Given that these algorithms are tailored for use with magnetometers configured in a gradiometry setup, their performance within this boomless context aligns with expectations.

Table 5.2 provides a summary of the median results of each metric for each algorithm across all three axes in the boomless configuration. The RMSE values confirm the superior performance of the UBSS algorithm, which consistently achieved the lowest median RMSE across all axes, followed closely by WAIC-UP and M-SSA. Correlation coefficients remain high for UBSS and

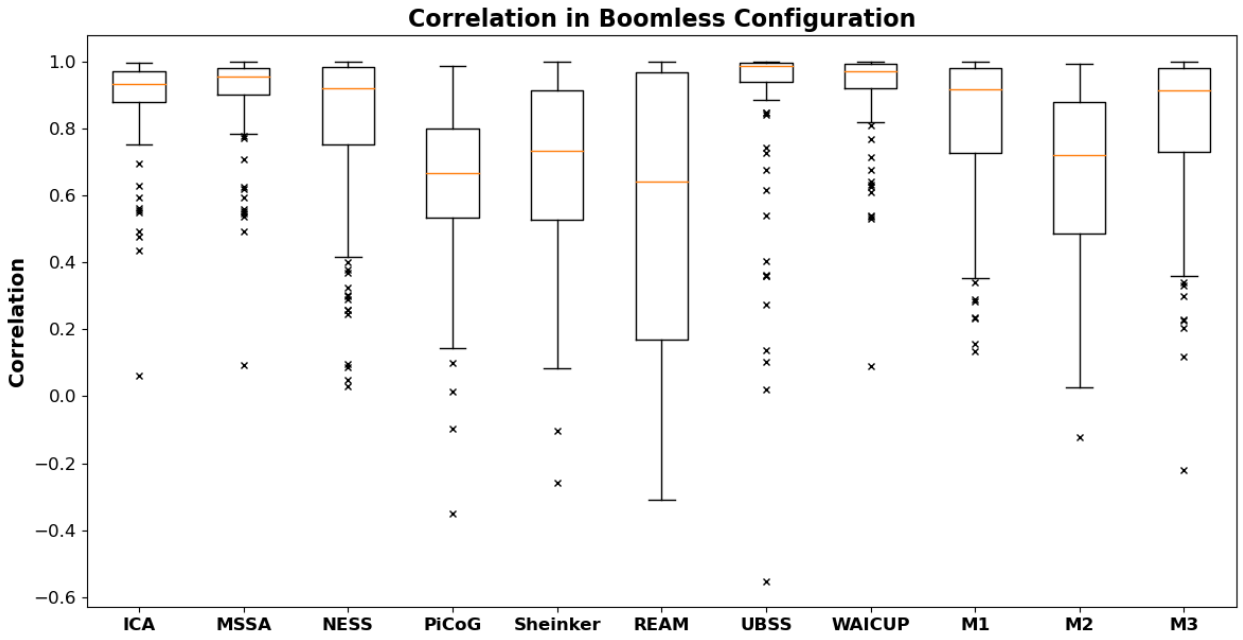

Figure 5.11: Distribution of correlation coefficients for the z-axis signals processed by MAGPRIME algorithms, compared with unprocessed signals from bus-mounted magnetometers. ICA, M-SSA, UBSS, and WAIC-UP each show high correlations and a small interquartile range.

WAIC-UP, reaffirming their effective alignment with the variable ambient field signal. SNR values further delineate the hierarchy of algorithm performance, with UBSS achieving the highest median SNR, especially on the x-axis. The consistency of UBSS across these metrics, coupled with the high correlation and SNR values, underscores its potential for practical application in space missions utilizing a boomless CubeSat design. WAIC-UP and MSSA also emerge as reliable alternatives, with their performance being significantly better than the least noisy magnetometer (M1) in multiple aspects.

5.5 Discussion and Future work

In this chapter, we introduce the MAGPRIME Python library, which consolidates various magnetic noise removal algorithms into a user-friendly platform for scientists and engineers. We have developed two benchmarks to assess the effectiveness of the algorithms within the MAGPRIME library. Benchmark A involves positioning two magnetometers collinearly at the base and tip of

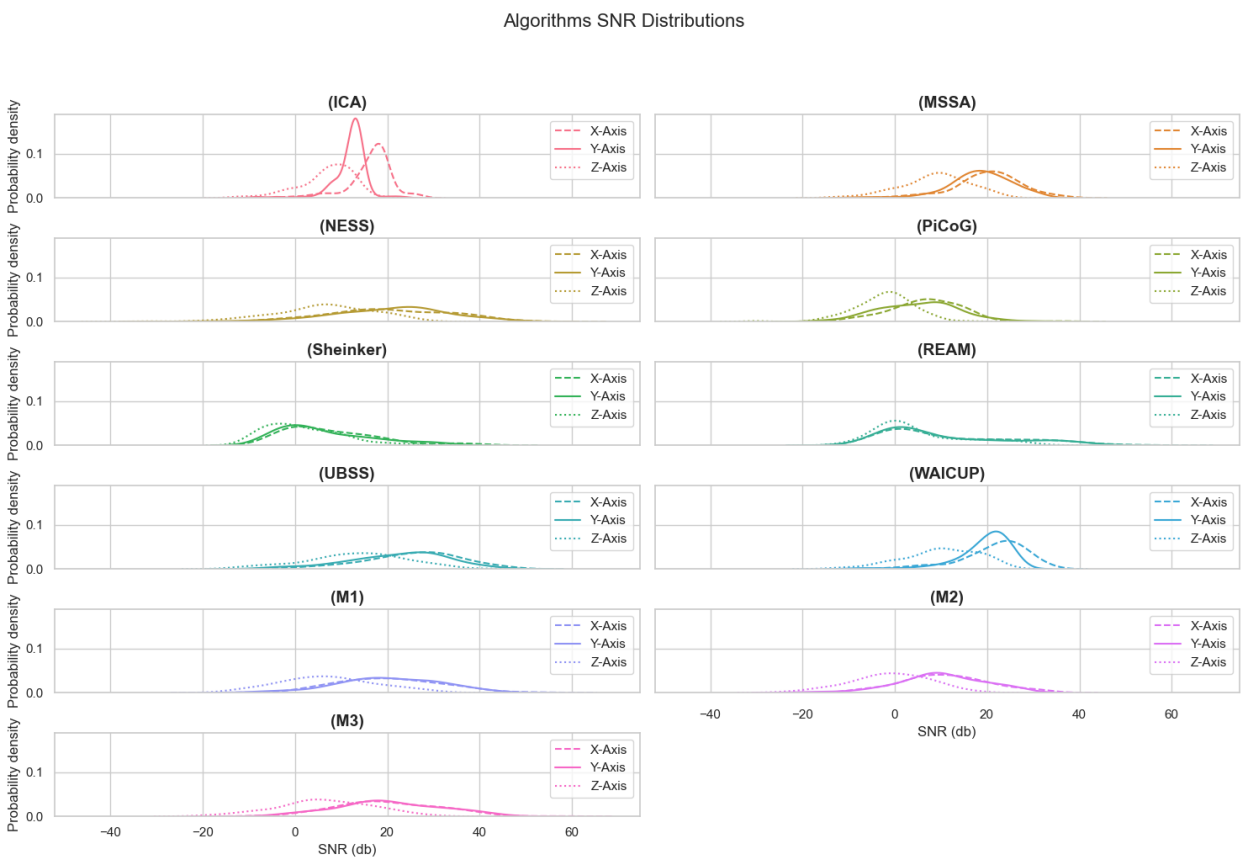

Figure 5.12: Probability density functions for SNR values of each noise removal algorithm across the x, y, and z axes in the boomless configuration. The distributions highlight the variability in performance, with some algorithms consistently achieving higher SNRs indicative of more effective noise reduction capabilities.

Table 5.2: Median Results for Boomless Configuration

Metric		ICA	MSSA	Ness	PiCoG	Sheinker	Ream	UBSS	WAICUP	M1	M2	M3
RMSE	X	31.49	21.34	24.69	108.14	135.05	119.51	10.82	16.88	23.93	72.48	25.42
	Y	51.47	25.70	16.47	121.25	155.11	145.69	14.40	20.50	22.91	72.55	24.60
	Z	24.21	20.71	26.83	74.68	58.39	50.00	11.93	17.02	26.23	65.18	28.38
Corr	X	0.9931	0.9966	0.9959	0.9321	0.9089	0.8850	0.9992	0.9984	0.9955	0.9708	0.9954
	Y	0.9751	0.9956	0.9975	0.9124	0.8357	0.7863	0.9987	0.9973	0.9961	0.9605	0.9958
	Z	0.9327	0.9542	0.9216	0.6659	0.7318	0.6412	0.9866	0.9700	0.9182	0.7192	0.9124
SNR	X	17.68	21.05	19.79	6.96	5.03	6.10	26.95	23.09	20.06	10.44	19.54
	Y	12.82	18.85	22.72	5.40	3.24	3.78	23.89	20.81	19.85	9.84	19.23
	Z	7.61	8.97	6.72	-2.17	-0.03	1.31	13.76	10.67	6.92	-0.99	6.23

a 30 cm mechanical boom attached to a 3U spacecraft, as depicted in Figure 5.2. We conducted 100 simulations with four dipolar noise sources randomly distributed within the CubeSat's vol-

ume. Each noise source simulates stray magnetic field noise from various sources, including the GOES-16 satellite and the Michibiki-1 satellite, as illustrated in Figure 5.3.

We tested the eight algorithms in the MAGPRIME library against these noise scenarios, evaluating them using metrics such as RMSE, SNR, and correlation, and compared them to the raw triaxial magnetometer signals. Our analysis showed that the unprocessed magnetometer on the boom performed remarkably well, with a median RMSE of nearly 7.47 nT for the x-axis, 6.74 nT for the y-axis, and 14.42 nT for the z-axis, significantly better than the base magnetometer's 773.30 nT for X, 720.81 nT for Y, and 1389.38 nT for Z. This finding reinforces the established understanding that using a boom is the gold standard in spacecraft magnetometry. Interestingly, both the modern UBSS algorithm and the traditional gradiometry algorithm, as described by Ness et al. (1971), either matched or surpassed the boom's performance in terms of SNR, correlation, or RMSE. This suggests that the Ness et al. (1971) algorithm is highly effective when used with a sufficiently long boom and an accurately characterized coupling matrix. In contrast, the UBSS algorithm does not require prior knowledge of the spacecraft's magnetic environment and matched the performance of the Ness et al. (1971) algorithm. This makes it a viable option when coupling coefficients are challenging to determine or subject to change, and it has significant implications for reducing the requirements for magnetic cleanliness and characterization in spacecraft design.

Some of the algorithms we tested require preprocessing to remove low-frequency trends, which could potentially skew the SNR and RMSE metrics. During our correlation analysis, which used a detrended approach, we found that the WAIC-UP, M-SSA, and ICA algorithms all achieved high correlations exceeding 0.9. Specifically, the WAIC-UP algorithm exhibited outstanding correlation scores, registering above 0.9753 for the x-axis, 0.9664 for the y-axis, and a lower 0.4859 for the z-axis. Transitioning to the UBSS and Ness algorithms revealed an even higher level of performance. Ness, in particular, showed an exceptional alignment with the true signal, achieving correlations of 0.9998 for the x-axis, 0.9997 for the y-axis, and 0.9827 for the z-axis, nearly matching the near-perfect scores of UBSS, which achieved 0.9997 for X, 0.9995 for Y, and 0.9854 for Z. The boom's correlations were similarly impressive, scoring 0.9996 on both the X and Y axes, and 0.9738 on

the Z axis. These results clearly highlighted both UBSS and Ness, alongside the use of a boom, as the top-performing solutions in our Benchmark A analysis.

In Benchmark B, we evaluated the same noise signals used in Benchmark A but within a boomless setup. This setup involved mounting magnetometers at the top, middle, and bottom of a 3U CubeSat, as depicted in Figure 5.2. While bus-mounted magnetometers offer a cost-effective alternative to boom-mounted ones, they are more susceptible to stray magnetic field interference. In our 100 randomized simulations, the unprocessed magnetometer readings showed median RMSEs between 22 and 76 nT. We ensured that no noise source was positioned close enough to a magnetometer to generate excessively high magnetic field magnitudes.

We applied algorithms designed for dual magnetometers, such as Ness, PiCoG, Sheinker, and Ream, to the top (M1) and middle (M2) magnetometers. The analysis revealed that on one axis each, Ness and ICA outperformed the least noisy magnetometer. M-SSA excelled on two axes, whereas WAIC-UP and UBSS surpassed the performance on all three axes. Notably, UBSS achieved the most substantial reduction in RMSE, bringing it down to 10-15 nT for each axis, while WAIC-UP's improvement was more modest, with RMSEs ranging from 17-21 nT per axis. The median correlation and SNR results mirrored these RMSE findings. An in-depth analysis of the SNR distribution highlighted ICA's consistency, closely followed by WAIC-UP. While neither ICA nor WAIC-UP could best UBSS in median RMSE, they consistently achieved comparable SNRs across varied experiments.

The outcomes from Benchmark B indicate that UBSS is not only the most effective noise removal algorithm in this scenario but also a strong competitor to Ness from Benchmark A. This benchmark demonstrates the viability of boomless magnetometry. Even without optimal magnetometer placement or magnetic cleanliness, using a boomless setup with UBSS can reduce stray magnetic field interference to nearly 10 nT. While this level may not be adequate for certain heliophysical studies, such as analyzing small amplitude MHD waves or planetary induction, it is acceptable for many other types of investigations. The emergence of boomless magnetometry has the potential to significantly influence space science by enabling the mass production of low-cost

space science satellites.

The two benchmarks demonstrate MAGPRIME's potential for integration into the design process of space exploration missions. When used alongside magnetic field simulation software like Magpylib, MAGPRIME enables the exploration of design trade-offs. During a spacecraft's design phase, it can determine the optimal minimum boom length and the most effective magnetometer placement. This is shown in the best case of Benchmark B where UBSS achieved sub-nanotesla accuracy. These results indicate that boomless high-fidelity magnetic field measurements can be acheived with strategic knowledge of noise source locations and optimized magnetometer placement. If specific design constraints, such as boom length, cannot be met, MAGPRIME can identify the algorithm best suited to the spacecraft's unique design. Furthermore, the MAGPRIME library can be adapted for use in a mission's data processing pipeline to analyze magnetometer data. Overall, MAGPRIME is a valuable tool that supports spacecraft missions from the research and design stages through to operational phases.

The outcomes of these experiments come with several notable limitations due to their randomized nature. First, some algorithms require detrending of magnetometer signals to effectively clean high-frequency stray magnetic interference. The signals in our study were retrended using a basic mean trend method, which likely reintroduced low-frequency noise from sources like arcjet and Michibiki noise signals into the cleaned signal. Therefore, correlation, which detrends both the estimated and true magnetic field signals in its calculation, emerges as a more accurate measure of these algorithms' efficacy. Another limitation is the tunability of algorithm-specific parameters to match the unique magnetic field signature of a spacecraft. In our benchmarks, we did not adjust these parameters for each randomized simulation, possibly underrepresenting the algorithms' true potential in real-world scenarios. Future work could involve taking the worst-case and median-case noise scenarios and running the algorithms with tuned parameters. This approach would provide a clearer understanding of how different algorithms might perform in practical applications. Finally, each algorithm has an ideal magnetometer placement within a spacecraft to maximize its effectiveness. For instance, Ness requires two magnetometers on a boom, while UBSS works best when

magnetometers are positioned to maximize orthogonality between mixing vectors in its mixing matrix (Candès, 2008). An application of MAGPRIME involves determining the optimal magnetometer placements based on a spacecraft's design. However, in our Monte Carlo simulations, the magnetometer locations were fixed and not optimized, which could have influenced the results.

The MAGPRIME library aims to facilitate the collaborative development of noise removal algorithms and simplify the design and integration of spaceflight magnetometers. By establishing two benchmarks, we assessed the effectiveness of MAGPRIME's algorithms using SNR, RMSE, and correlation metrics. These benchmarks reveal that long mechanical booms remain the standard in spaceflight magnetometer design, yet algorithms like UBSS and Ness not only enhance the benefits of a boom but can also reduce its length requirements. The second benchmark highlighted that various algorithms are effective for boomless magnetometer designs, with UBSS demonstrating superior noise reduction capabilities. Future directions for the MAGPRIME library include refining the performance of existing algorithms and incorporating additional noise removal algorithms. Moreover, MAGPRIME also enabled streamlined studies on optimal boom lengths or the number of magnetometers for boomless spacecraft designs. As a community-led initiative, we invite interested individuals to contribute to the ongoing development of MAGPRIME.

5.6 Conclusion

This chapter introduced MAGPRIME as an innovative, open-source Python library with significant potential to advance in situ space exploration missions. Its extensive suite of magnetic noise removal algorithms, rigorously evaluated through two statistical benchmarks, offers a toolset for scientists and engineers. Benchmark A underscored the effectiveness of algorithms like UBSS and gradiometry by Ness et al. (1971), which demonstrated superior noise reduction capabilities even over traditional boom-mounted magnetometers. This highlighted the potential to optimize boom length and achieve high fidelity in magnetic field measurements.

Benchmark B explored the performance of MAGPRIME's algorithms in more challenging,

boomless magnetometer configuration. The standout performance of UBSS in this benchmark, showing significant noise reduction with median RMSEs significantly lower than unprocessed signals, illustrates its utility in compact, cost-effective spacecraft designs. This finding is particularly relevant for CubeSats and constellation satellites where design and budget considerations are paramount.

MAGPRIME's benchmarks validate its current algorithms and set the stage for further advancements. The library will evolve with the development of new algorithms and the refinement of existing ones. As a community-driven project, MAGPRIME is an new and potentially useful resource in space magnetism research. It supports various phases of spacecraft missions, from design and development to operational data processing, improving the precision of magnetic field measurements.

CHAPTER 6

Conclusions

6.1 Summary of Key Findings

In this work, we addressed the issue of stray magnetic field noise in spaceborne magnetometry. We attempted to minimize the aspects of spacecraft design, testing, and mitigation that are specifically related to the requirements for managing stray magnetic field noise, such as the need for a long mechanical boom. These solutions were not foolproof and provided extra complications for small space platforms such as CubeSats. We resolved stray magnetic field interference through the development of two magnetometer noise removal algorithms. Chapter 2 and Chapter 3 present the development and validation of a noise removal algorithm called UBSS, and Chapter 4 details another algorithm called WAIC-UP. In Chapter 5, we integrated UBSS, WAIC-UP, and a suite of other noise removal algorithms into a single Python package, and compared the efficacy of these algorithms using Monte Carlo simulations on different spacecraft configurations.

In Chapter 2, we developed and validated a two-step signal processing algorithm that utilizes density-based cluster analysis to identify stray magnetic field signals and compressive sensing to separate these from the ambient magnetic field signal. This method, dubbed UBSS, is specifically designed for scenarios where the number of noise sources exceeds the number of magnetometers, and there is no prior knowledge about the location, orientation, or spectral content of the stray magnetic field signals. We validated UBSS through simulations, employing a mix of real magnetic field data and computer-generated signals. In these tests, UBSS significantly reduced the RMSE of the measured signal relative to the true signal, from over 300 nT to below 3 nT. Additionally,

in a laboratory experiment using a mock CubeSat, three PNI RM3100 magnetometers, and four copper coils to generate noise, UBSS demonstrated its efficacy by reducing the RMSE from 328 nT to 8 nT at a 50 Hz cadence. These results conclusively demonstrated that UBSS can effectively mitigate magnetometer interference in scenarios lacking a boom and where the number of noise sources is greater than the number of magnetometers.

Chapter 3 presents an integrated magnetometer and noise removal suite composed of the Quad-Mag magnetometer and a new and improved version of UBSS. The Quad-Mag is the first magnetometer designed to be used without a boom. It is composed of four smaller magnetometers in a single 10 cm x 10 cm CubeSat electronics card. The four magnetometers provide distributed measurements of the spacecraft's local magnetic field environment, and enable the use of noise removal algorithms. The improvements to UBSS included the application of SSP detection in both the cluster analysis and compressive sensing stages. This algorithm was capable of discerning whether a time-frequency bin contained energy from multiple signals, thereby improving signal identification by filtering out points with multi-source interference. Additionally, an iterative-weighting scheme was developed to preferentially separate source signals during the compressive sensing stage. The weighting scheme looked at the distribution of energy to each source signal and adjusted their weighted L1 norm to mitigate noise signals unintentionally being attributed to the ambient magnetic field signal. Several experiments were performed to validate this integrated Quad-Mag and UBSS suite. The first experiment was performed in the lab using the Quad-Mag and copper coils to generate noise. In this experiment, UBSS successfully reduced the RMSE from 120 nT at the least noisy magnetometer to 4.4 nT. Moreover, simulations of 1U, 2U, 3U, and 6U CubeSats with the Quad-Mag, and several dipolar noise sources were conducted. In each case, UBSS reduced the RMSE by nearly two orders of magnitude down to the noise floor of the instrument. These experiments collectively demonstrated that the Quad-Mag with UBSS provides an effective platform for CubeSat magnetometer measurements.

UBSS performed exceptionally well at removing stray magnetic field noise, however, it was a computationally expensive algorithm. In scenarios needing real-time data such as space weather

beacon data or attitude determination, accurate and timely magnetic field data were necessary. In Chapter 4, a noise removal algorithm called WAIC-UP was introduced. This algorithm efficiently eliminated stray magnetic field signals using multiple magnetometers, without requiring prior knowledge of the interference sources. WAIC-UP sparsified the noisy magnetometer measurements using a wavelet transform and applied an analytical method to identify noise signals in each frequency band. The method distinguished itself by its computational efficiency and its ability to handle various interference scenarios. Its effectiveness was validated through more than 1500 randomized simulations and real-world testing using the laboratory datasets from Chapter 2 and Chapter 3. WAIC-UP excelled at removing high-frequency magnetic field noise, but due to the nature of the wavelet transform, it could not remove low-frequency noise, where the wavelet's cone of influence came into play.

Finally, in Chapter 5, we collated UBSS, WAIC-UP, and several other published noise removal algorithms into the MAGPRIME library. The MAGPRIME library serves several purposes. The first is to embrace the tenets of Open Science and pave the way for community development of magnetometer noise removal algorithms. The second purpose of MAGPRIME is to benchmark the noise removal algorithms. We created two benchmarks: one to test the suite of noise removal algorithms in a traditional gradiometry configuration and another for a three-magnetometer boomless configuration. The benchmarks show that UBSS and gradiometry perform extremely well with the use of a boom, and can remove the majority of spacecraft noise. However, this result depends on several factors, such as the length of the boom and noise levels at the bus of the spacecraft. In the boomless benchmark, UBSS outperformed the other MAGPRIME algorithms. However, the results from the boomless magnetometer's benchmark had noise remaining on the order of 10 nT, while the simulations with a boom had noise near 5 nT. This shows that the inclusion of a boom depends on the science goals of the mission as well as the size and complexity of the spacecraft. For missions such as the Europa clipper which require less than 1 nT to measure the inductive response of Europa's subsurface oceans, using a longer boom is highly beneficial.

6.2 Future Work

6.2.1 Underdetermined Blind Source Separation

The UBSS algorithm is a series of algorithms that can each be improved. The first step in the UBSS algorithm is cluster analysis. In order to identify noise signals, the magnetometer data are processed through SSP detection, a low energy filter, and finally cluster analysis. The filtering steps both have parameters that require manual tuning. The relationship of these parameters could be defined with respect to the behavior of the hardware being used. In the case where a magnetometer has pink noise, the SSP and low-energy filters should be frequency dependent. In the clustering steps, stray magnetic field signals may appear with different orders of magnitude, or the noise sources could have small spatial separation that makes them appear similar at each magnetometer. HDBSCAN significantly advanced clustering analysis by employing density-based methods and considering noise in the data. Future developments might focus on implementing clustering algorithms that adapt over time, better suited for the dynamic conditions of spacecraft environments.

Compressive sensing is a complex algorithm that is an active field of research. In this work, we used the ECOS solver with an iteratively-weighted L1 norm. Additionally, the L1 norm was weighted using a novel SSP-based scheme. This scheme is ineffective when the mixing matrix is K-sparse. K-sparsity relates to the restricted isometry property. It indicates how effective CS is at separating multi-source points. The iterative weighting scheme in this work assumes that two overlapping signals in a time-frequency bin cannot be separated. However, if the corresponding mixing vectors of those signals are near orthogonal, then CS may succeed in separating them. Future work could include checking the orthogonality of the estimated signal mixing vectors and adjusting the weighting scheme based on the estimated restricted isometry property.

In both the signal identification stage and signal separation stage, a time-frequency transform of the mixed signals is taken in order to transform the data into a sparse representation. The Short Time Fourier Transform has a fixed window length that limits the time-resolution at high frequencies and frequency resolution at low frequencies. The wavelet transform has high time-

frequency resolution, but is invalid at low frequencies due to the cone of influence limiting the linearity of the transform. In this work, we used the Non-Stationary Gabor Transform. This is an invertible transform that adjusts the window length of the Fourier transform with respect to frequency. The adjustable window length makes this transform similar to the wavelet transform, but it does not have a cone of influence that limits it. The purpose of using a time-frequency transform is to represent the mixed signals in a domain that the noise is easily separable from the ambient magnetic field. Future work could include investigating other high time-frequency resolution transforms that are invertible.

6.2.2 Wavelet Adaptive Interference Cancellation for Underdetermined Platforms

WAIC-UP is a high speed algorithm that removes noise using multiple magnetometers. With a pair of magnetometers, the WAIC-UP algorithm calculates the gain of a stray magnetic field signal for each wavelet scale. With more than two magnetometers, the WAIC-UP algorithm is run on each permutation of magnetometer pairs and chooses the time-frequency points with the minimum magnitude to restore the ambient magnetic field. This algorithm is more effective with more magnetometers and can successfully remove high-frequency signals; however, it relies on a wavelet transform, which is not valid at lower frequencies. When a wavelet is cutoff due to the length of the signal, the wavelet transform is not linear and the gain of noise signals cannot be estimated. Future work for the WAIC-UP transform could be to investigate how to apply it to constant-Q transforms such as NSGT, or to characterize the exact low frequency cut-off.

WAIC-UP is currently designed to be a post-processing algorithm, but it can be adapted to be a real-time algorithm. WAIC-UP uses several operations such as convolutions, correlations, and differences, which are all streamable operations. With a platform-based redesign, the WAIC-UP algorithm can become a real-time noise removal algorithm with applications in attitude determination and live space weather products.

6.2.3 The MAGPRIME Library

The MAGPRIME Python library is designed to be a living library of magnetometer signal processing algorithms. Right now, it is specifically designed for magnetometer noise removal. MAGPRIME serves as a promising platform for the future development and benchmarking of these algorithms. However, MAGPRIME can also serve as a general-purpose library for other magnetometer processing algorithms such as ULF wave detection, polarization analysis, and analysis or calibration techniques for space-based and ground-based applications.

6.2.4 Ground Magnetometers

Ground magnetometers are used to study a large variety of magnetic phenomena from dipolarization to large scale magnetospheric currents. Accurate ground magnetometer measurements come with a host of stray magnetic field issues that are unique to their particular environment. Several simplifying assumptions can be made about the stray magnetic fields on a spacecraft that could not be made about ground magnetometers. For example, on a spacecraft all noise signals are considered local, so each noise source has a different magnitude at each magnetometer. On the other hand, a ground magnetometer may be contaminated with interference from a train or plane, which could be very distant. In that case, it is difficult to use multiple magnetometers to identify noise in the same way that is done on a spacecraft. Future work for noise removal in ground magnetometry includes researching the optimal placement of ground magnetometers to remove both near and far field noise signals. Additionally, in one of my journeys to Igloolik, Nunavut, we discovered that the wooden structure containing our ground magnetometer is frequently used as a playground. If kids jump on the ground magnetometer then that would create noise that looks very similar to geomagnetic field perturbations. This issue could be addressed in future work by synthesizing data from multiple types of sensors such as an accelerometer to remove different types of noise.

6.3 Research Implications

This dissertation details the development of two magnetometer noise removal algorithms for space-based magnetic field measurements. These algorithms have several implications for the field of magnetometry. The implications of UBSS and WAIC-UP include minimizing the need for long mechanical booms for high-fidelity magnetic field measurements. Reducing the length of booms, or eliminating them altogether, lowers the cost of access to space for magnetic field measurements. Several prominent missions such as Dawn and New Horizons did not include magnetometers due to cost and design constraints. UBSS and WAIC-UP enable easy integration of bus-mounted magnetometers into flagship spacecraft designs.

At the other end of the spectrum, CubeSats are becoming increasingly prominent vehicles in space exploration missions. Due to considerable design constraints, only a few CubeSats have managed to include magnetometers on mechanical booms, while several others have not. The advent of the Quad-Mag, coupled with UBSS or WAIC-UP, enables CubeSats to take high fidelity magnetic field measurements. The low-cost and mass-producible nature of CubeSats enables future constellations equipped with magnetometers to take magnetic field measurements of the Earth with high spatial and temporal resolution. This advancement will significantly enhance investigations into Magnetosphere-Ionosphere coupling and potentially facilitate future studies of magnetic reconnection at the electron-diffusion scale.

The development of UBSS and WAIC-UP for space missions represents a major step forward in the field of magnetometry. These technologies facilitate the inclusion of high-quality magnetic field measurement tools in a diverse range of space missions, making the process easier and more practical. Particularly in CubeSats, their use enables more detailed observations of the Earth's magnetic field. This advancement has the potential to lead to new discoveries and enhance our understanding of space phenomena, thereby transforming the methods of studying and exploring space.

BIBLIOGRAPHY

Acuña, M. H. (2002). Space-based magnetometers. *Review of Scientific Instruments*, 73(11):3717–3736.

Alizadeh, F. and Goldfarb, D. (2003). Second-order cone programming. *Mathematical Programming*, 95(1):3–51.

Anderson, B. J., Korth, H., Waters, C. L., Green, D. L., Merkin, V. G., Barnes, R. J., and Dyrud, L. P. (2014). Development of large-scale Birkeland currents determined from the Active Magnetosphere and Planetary Electrodynamics Response Experiment. *Geophysical Research Letters*, 41(9):3017–3025. _eprint: https://agupubs.onlinelibrary.wiley.com/doi/pdf/10.1002/2014GL059941.

Angelopoulos, V. (2009). The THEMIS Mission. In Burch, J. L. and Angelopoulos, V., editors, *The THEMIS Mission*, pages 5–34. Springer, New York, NY.

Angelopoulos, V. (2014). The ARTEMIS Mission. In Russell, C. and Angelopoulos, V., editors, *The ARTEMIS Mission*, pages 3–25. Springer, New York, NY.

Angelopoulos, V., Tsai, E., Bingley, L., Shaffer, C., Turner, D. L., Runov, A., Li, W., Liu, J., Artemyev, A. V., Zhang, X.-J., Strangeway, R. J., Wirz, R. E., Shprits, Y. Y., Sergeev, V. A., Caron, R. P., Chung, M., Cruce, P., Greer, W., Grimes, E., Hector, K., Lawson, M. J., Leneman, D., Masongsong, E. V., Russell, C. L., Wilkins, C., Hinkley, D., Blake, J. B., Adair, N., Allen, M., Anderson, M., Arreola-Zamora, M., Artinger, J., Asher, J., Branchevsky, D., Capitelli, M. R., Castro, R., Chao, G., Chung, N., Cliffe, M., Colton, K., Costello, C., Depe, D., Domae, B. W., Eldin, S., Fitzgibbon, L., Flemming, A., Fox, I., Frederick, D. M., Gilbert, A., Gildemeister, A., Gonzalez, A., Hesford, B., Jha, S., Kang, N., King, J., Krieger, R., Lian, K., Mao, J., McKinney, E., Miller, J. P., Norris, A., Nuesca, M., Palla, A., Park, E. S. Y., Pedersen, C. E., Qu, Z., Rozario, R., Rye, E., Seaton, R., Subramanian, A., Sundin, S. R., Tan, A., Turner, W., Villegas, A. J., Wasden, M., Wing, G., Wong, C., Xie, E., Yamamoto, S., Yap, R., Zarifian, A., and Zhang, G. Y. (2020). The ELFIN Mission. *Space Science Reviews*, 216(5):103.

Archer, M. O., Horbury, T. S., Brown, P., Eastwood, J. P., Oddy, T. M., Whiteside, B. J., and Sample, J. G. (2015). The MAGIC of CINEMA: first in-flight science results from a miniaturised anisotropic magnetoresistive magnetometer. *Annales Geophysicae*, 33(6):725–735. Publisher: Copernicus GmbH.

Aschenbrenner, H. and Goubau, G. (1936). Eine anordnung registrieung rascher magnetischer storungen. *Hochfreg Tech. Elektroakust.*, 47:178–181.

Auster, H. U., Glassmeier, K. H., Magnes, W., Aydogar, O., Baumjohann, W., Constantinescu, D., Fischer, D., Fornacon, K. H., Georgescu, E., Harvey, P., Hillenmaier, O., Kroth, R., Ludlam, M., Narita, Y., Nakamura, R., Okrafka, K., Plaschke, F., Richter, I., Schwarzl, H., Stoll, B., Valavanoglou, A., and Wiedemann, M. (2008). The THEMIS Fluxgate Magnetometer. *Space Science Reviews*, 141(1):235–264.

Bai, X., Fu, W., Zhou, C., and Liu, Y. (2021). Mixing Matrix Estimation Algorithm for Time-Varying Radar Signals in a Dynamic System Under UBSS Model. *Circuits, Systems, and Signal Processing*, 40(6):3075–3098.

Bale, S. D., Goetz, K., Harvey, P. R., Turin, P., Bonnell, J. W., Dudok de Wit, T., Ergun, R. E., MacDowall, R. J., Pulupa, M., Andre, M., Bolton, M., Bougeret, J.-L., Bowen, T. A., Burgess, D., Cattell, C. A., Chandran, B. D. G., Chaston, C. C., Chen, C. H. K., Choi, M. K., Connerney, J. E., Cranmer, S., Diaz-Aguado, M., Donakowski, W., Drake, J. F., Farrell, W. M., Fergeau, P., Fermin, J., Fischer, J., Fox, N., Glaser, D., Goldstein, M., Gordon, D., Hanson, E., Harris, S. E., Hayes, L. M., Hinze, J. J., Hollweg, J. V., Horbury, T. S., Howard, R. A., Hoxie, V., Jannet, G., Karlsson, M., Kasper, J. C., Kellogg, P. J., Kien, M., Klimchuk, J. A., Krasnoselskikh, V. V., Krucker, S., Lynch, J. J., Maksimovic, M., Malaspina, D. M., Marker, S., Martin, P., Martinez-Oliveros, J., McCauley, J., McComas, D. J., McDonald, T., Meyer-Vernet, N., Moncuquet, M., Monson, S. J., Mozer, F. S., Murphy, S. D., Odom, J., Oliverson, R., Olson, J., Parker, E. N., Pankow, D., Phan, T., Quataert, E., Quinn, T., Ruplin, S. W., Salem, C., Seitz, D., Sheppard, D. A., Siy, A., Stevens, K., Summers, D., Szabo, A., Timofeeva, M., Vaivads, A., Velli, M., Yehle, A., Werthimer, D., and Wygant, J. R. (2016). The FIELDS Instrument Suite for Solar Probe Plus. *Space Science Reviews*, 204(1):49–82.

Banfield, D., Rodriguez-Manfredi, J. A., Russell, C. T., Rowe, K. M., Leneman, D., Lai, H. R., Cruce, P. R., Means, J. D., Johnson, C. L., Mittelholz, A., Joy, S. P., Chi, P. J., Mikellides, I. G., Carpenter, S., Navarro, S., Sebastian, E., Gomez-Elvira, J., Torres, J., Mora, L., Peinado, V., Lepinette, A., Hurst, K., Lognonné, P., Smrekar, S. E., Banerdt, W. B., and The TWINS Team (2018). InSight Auxiliary Payload Sensor Suite (APSS). *Space Science Reviews*, 215(1):4.

Baraniuk, R. G. (2007). Compressive Sensing [Lecture Notes]. *IEEE Signal Processing Magazine*, 24(4):118–121. Conference Name: IEEE Signal Processing Magazine.

Beck, A. and Teboulle, M. (2009a). A fast iterative shrinkage-thresholding algorithm for linear inverse problems. *SIAM journal on imaging sciences*, 2(1):183–202.

Beck, A. and Teboulle, M. (2009b). A fast Iterative Shrinkage-Thresholding Algorithm with application to wavelet-based image deblurring. In *2009 IEEE International Conference on Acoustics, Speech and Signal Processing*, pages 693–696. ISSN: 2379-190X.

Behannon, K. W., Acuna, M. H., Burlaga, L. F., Lepping, R. P., Ness, N. F., and Neubauer, F. M. (1977). Magnetic field experiment for Voyagers 1 and 2. *Space Science Reviews*, 21(3):235–257.

Boschetti, D., Gervasio, G., and Marziali, I. (2012). Montecarlo approach for magnetic cleanliness evaluation on spacecraft. In *2012 ESA Workshop on Aerospace EMC*, pages 1–3.

Bowen, T. A., Bale, S. D., Bonnell, J. W., Dudok de Wit, T., Goetz, K., Goodrich, K., Gruesbeck, J., Harvey, P. R., Jannet, G., Koval, A., MacDowall, R. J., Malaspina, D. M., Pulupa, M., Revillet, C., Sheppard, D., and Szabo, A. (2020). A Merged Search-Coil and Fluxgate Magnetometer Data Product for Parker Solar Probe FIELDS. *Journal of Geophysical Research: Space Physics*, 125(5):e2020JA027813. _eprint: https://onlinelibrary.wiley.com/doi/pdf/10.1029/2020JA027813.

Broadfoot, R. M., Miles, D. M., Holley, W., and Howarth, A. D. (2022). In situ calibration of the Swarm-Echo magnetometers. *Geoscientific Instrumentation, Methods and Data Systems*, 11(2):323–333. Publisher: Copernicus GmbH.

Burlaga, L. F., Klein, L., Sheeley Jr., N. R., Michels, D. J., Howard, R. A., Koomen, M. J., Schwenn, R., and Rosenbauer, H. (1982). A magnetic cloud and a coronal mass ejection. *Geophysical Research Letters*, 9(12):1317–1320. _eprint: https://onlinelibrary.wiley.com/doi/pdf/10.1029/GL009i012p01317.

Cai, Y., Zhao, Y., Ding, X., and Fennelly, J. (2012). Magnetometer basics for mobile phone applications.

Califf, S., Early, D., Grotenhuis, M., Loto'aniu, T. M., and Kronenwetter, J. (2020). Correcting the Arcjet Thruster Disturbance in GOES-16 Magnetometer Data. *Space Weather*, 18(1):e2019SW002347. _eprint: https://onlinelibrary.wiley.com/doi/pdf/10.1029/2019SW002347.

Campello, R. J. G. B., Moulavi, D., and Sander, J. (2013). Density-Based Clustering Based on Hierarchical Density Estimates. In Pei, J., Tseng, V. S., Cao, L., Motoda, H., and Xu, G., editors, *Advances in Knowledge Discovery and Data Mining*, Lecture Notes in Computer Science, pages 160–172, Berlin, Heidelberg. Springer.

Candes, E. and Tao, T. (2007). The Dantzig selector: Statistical estimation when p is much larger than n. *The Annals of Statistics*, 35(6). arXiv:math/0506081.

Candès, E. J. (2008). The restricted isometry property and its implications for compressed sensing. *Comptes Rendus Mathematique*, 346(9):589–592.

Candès, E. J., Wakin, M. B., and Boyd, S. P. (2008). Enhancing Sparsity by Reweighted 1 Minimization. *Journal of Fourier Analysis and Applications*, 14(5):877–905.

Carter, D., Freesland, D., Tadikonda, S. K., Kronenwetter, J., Todirita, M., Dahya, M., and Chu, D. (2016). Correcting GOES-R magnetometer data for stray fields. In *2016 ESA Workshop on Aerospace EMC (Aerospace EMC)*, pages 1–6, Valencia, Spain. IEEE.

Cerman, A., Kuna, A., Ripka, P., and Merayo, J. M. G. (2005). Digitalization of highly precise fluxgate magnetometers. *Sensors and Actuators A: Physical*, 121(2):421–429.

Chandran, B. D. G., Li, B., Rogers, B. N., Quataert, E., and Germaschewski, K. (2010). PERPENDICULAR ION HEATING BY LOW-FREQUENCY ALFVÉN-WAVE TURBULENCE IN THE SOLAR WIND. *The Astrophysical Journal*, 720(1):503. Publisher: The American Astronomical Society.

Clagett, C., Santos, L., Azimi, B., Cudmore, A., Marshall, J., Starin, S., Sheikh, S., Zesta, E., Paschalidis, N., Johnson, M., Kepko, L., Berry, D., Bonalsky, T., Chai, D., Colvin, M., Evans, A., Hesh, S., Jones, S., Peterson, Z., Rodriquez, J., and Rodriquez, M. (2017). Dellingr: NASA Goddard Space Flight Center's First 6U Spacecraft. *Small Satellite Conference*.

Coillot, C., Moutoussamy, J., Lebourgeois, R., Ruocco, S., and Chanteur, G. (2010). Principle and Performance of a Dual-Band Search Coil Magnetometer: A New Instrument to Investigate Fluctuating Magnetic Fields in Space. *IEEE Sensors Journal*, 10(2):255–260.

Coleman Jr., P. J. (1966). Variations in the interplanetary magnetic field: Mariner 2: 1. Observed properties. *Journal of Geophysical Research (1896-1977)*, 71(23):5509–5531. _eprint: https://onlinelibrary.wiley.com/doi/pdf/10.1029/JZ071i023p05509.

Coleman Jr., P. J., Sonett, C. P., Judge, D. L., and Smith, E. J. (1960). Some preliminary results of the Pioneer V magnetometer experiment. *Journal of Geophysical Research (1896-1977)*, 65(6):1856–1857. _eprint: https://onlinelibrary.wiley.com/doi/pdf/10.1029/JZ065i006p01856.

Constantinescu, O. D., Auster, H.-U., Delva, M., Hillenmaier, O., Magnes, W., and Plaschke, F. (2020). Maximum-variance gradiometer technique for removal of spacecraft-generated disturbances from magnetic field data. *Geoscientific Instrumentation, Methods and Data Systems*, 9(2):451–469. Publisher: Copernicus GmbH.

Crescentini, M., Syeda, S. F., and Gibiino, G. P. (2022). Hall-Effect Current Sensors: Principles of Operation and Implementation Techniques. *IEEE Sensors Journal*, 22(11):10137–10151. Conference Name: IEEE Sensors Journal.

Deshmukh, A. A., Sharma, S., Cutler, J. W., Moldwin, M., and Scott, C. (2020). Simple Regret Minimization for Contextual Bandits. *arXiv:1810.07371 [cs, stat]*. arXiv: 1810.07371.

Diamond, S. and Boyd, S. (2016). CVXPY: A Python-embedded modeling language for convex optimization. *Journal of Machine Learning Research*, 17(83):1–5.

Dolginov, S. S., Zhuzgov, L. N., and Seliutin, V. A. (1961). Magnetometric Equipment of the Third Soviet Artificial Earth Satellite. *ARS Journal*, 31(9):1329–1341.

Domahidi, A., Chu, E., and Boyd, S. (2013). ECOS: An SOCP solver for embedded systems. In *2013 European Control Conference (ECC)*, pages 3071–3076, Zurich. IEEE.

Du, A. M., Zhang, Y., Li, H. Y., Qiao, D. H., Yi, Z., Zhang, T. L., Meng, L. F., Ge, Y. S., Luo, H., Zhao, L., Sun, S. Q., Ou, J. M., Li, Z., Feng, X., and Dai, J. L. (2020). The Chinese Mars ROVER Fluxgate Magnetometers. *Space Science Reviews*, 216(8):135.

Eastwood, J. P., Hietala, H., Toth, G., Phan, T. D., and Fujimoto, M. (2015). What Controls the Structure and Dynamics of Earth's Magnetosphere? *Space Science Reviews*, 188(1):251–286.

Ester, M., Kriegel, H.-P., and Xu, X. (1996). A Density-Based Algorithm for Discovering Clusters in Large Spatial Databases with Noise. page 6.

Finley, M. G., Broadfoot, R. M., Shekhar, S., and Miles, D. M. (2023). Identification and Removal of Reaction Wheel Interference From In-Situ Magnetic Field Data Using Multichannel Singular Spectrum Analysis. *Journal of Geophysical Research: Space Physics*, 128(2):e2022JA031020. _eprint: https://onlinelibrary.wiley.com/doi/pdf/10.1029/2022JA031020.

Fratter, I., Léger, J.-M., Bertrand, F., Jager, T., Hulot, G., Brocco, L., and Vigneron, P. (2016). Swarm Absolute Scalar Magnetometers first in-orbit results. *Acta Astronautica*, 121:76–87.

Friis-Christensen, E., Lühr, H., Knudsen, D., and Haagmans, R. (2008). Swarm – An Earth Observation Mission investigating Geospace. *Advances in Space Research*, 41(1):210–216.

Ganushkina, N. Y., Liemohn, M. W., and Dubyagin, S. (2018). Current Systems in the Earth's Magnetosphere. *Reviews of Geophysics*, 56(2):309–332. _eprint: https://onlinelibrary.wiley.com/doi/pdf/10.1002/2017RG000590.

Gauss, K. F. (1833). Intensitas vis magneticæ terrestris ad mensuram absolutam revocata. *Abstracts of the Papers Printed in the Philosophical Transactions of the Royal Society of London*, 3:166–174. Publisher: Royal Society.

Gonzalez, W. D., Tsurutani, B. T., Gonzalez, A. L. C., Smith, E. J., Tang, F., and Akasofu, S.-I. (1989). Solar wind-magnetosphere coupling during intense magnetic storms (1978-1979). *Journal of Geophysical Research: Space Physics*, 94(A7):8835–8851. _eprint: https://onlinelibrary.wiley.com/doi/pdf/10.1029/JA094iA07p08835.

Gosling, J. T., Skoug, R. M., McComas, D. J., and Smith, C. W. (2005). Direct evidence for magnetic reconnection in the solar wind near 1 AU. *Journal of Geophysical Research: Space Physics*, 110(A1). _eprint: https://onlinelibrary.wiley.com/doi/pdf/10.1029/2004JA010809.

Greene, K., Hansen, C. T., and Miles, D. M. (2023). On the impact of thermal gradients across fluxgate sensors on in situ magnetic field measurements. *Journal of Geophysical Research: Space Physics*, 128(6):e2023JA031369. e2023JA031369 2023JA031369.

Guarnieri, F. L., Tsurutani, B. T., Gonzalez, W. D., Echer, E., Gonzalez, A. L. C., and Soraas, F. (2006). ICME and CIR storms with particular emphasis on HILDCAA events. page 7.

Guo, Q., Ruan, G., and Nan, P. (2017). Underdetermined Mixing Matrix Estimation Algorithm Based on Single Source Points. *Circuits, Systems, and Signal Processing*, 36(11):4453–4467.

Gustetic, J. L., Crusan, J., Rader, S., and Ortega, S. (2015). Outcome-driven open innovation at NASA. *Space Policy*, 34:11–17.

Hartinger, M. D., Turner, D. L., Plaschke, F., Angelopoulos, V., and Singer, H. (2013). The role of transient ion foreshock phenomena in driving Pc5 ULF wave activity. *Journal of Geophysical Research: Space Physics*, 118(1):299–312. _eprint: https://onlinelibrary.wiley.com/doi/pdf/10.1029/2012JA018349.

He, X.-s., He, F., and Xu, L. (2021). Underdetermined mixing matrix estimation based on joint density-based clustering algorithms. *Multimedia Tools and Applications*, 80(6):8281–8308.

Heppner, J. P., Ness, N. F., Scearce, C. S., and Skillman, T. L. (1963). Explorer 10 magnetic field measurements. *Journal of Geophysical Research (1896-1977)*, 68(1):1–46. _eprint: https://onlinelibrary.wiley.com/doi/pdf/10.1029/JZ068i001p00001.

Hoffmann, A. P. (2022). Adaptive cancellation of magnetic noise data set. *University of Michigan - Deep Blue Data*. https://doi.org/10.7302/bz6v-6q52.

Hoffmann, A. P. (2023). Data set for underdetermined blind source separation of cubesat quad-mag magnetometer data. *University of Michigan - Deep Blue Data*. https://doi.org/10.7302/rtr3-rs48.

Hoffmann, A. P. and Moldwin, M. B. (2022). Separation of Spacecraft Noise From Geomagnetic Field Observations Through Density-Based Cluster Analysis and Compressive Sensing. *Journal of Geophysical Research: Space Physics*, 127(9):e2022JA030757. _eprint: https://onlinelibrary.wiley.com/doi/pdf/10.1029/2022JA030757.

Hoffmann, A. P. and Moldwin, M. B. (2023). Wavelet-adaptive interference cancellation for underdetermined platforms: Enhancing boomless magnetic field measurements on compact spacecraft. *IEEE Transactions on Aerospace and Electronic Systems*, pages 1–10.

Hoffmann, A. P., Moldwin, M. B., Strabel, B. P., and Ojeda, L. V. (2023). Enabling boomless cubesat magnetic field measurements with the quad-mag magnetometer and an improved underdetermined blind source separation algorithm. *Journal of Geophysical Research: Space Physics*, 128(9):e2023JA031662. e2023JA031662 2023JA031662.

Holighaus, N., Dorfler, M., Velasco, G. A., and Grill, T. (2013). A Framework for Invertible, Real-Time Constant-Q Transforms. *IEEE Transactions on Audio, Speech, and Language Processing*, 21(4):775–785.

Holzman, D. (1958). Shen kua and his meng-ch'i pi-t'an. *T'oung Pao*, 46(3/5):260–292.

Hyvärinen, A. and Oja, E. (2000). Independent component analysis: algorithms and applications. *Neural Networks*, 13(4):411–430.

Imajo, S., Nosé, M., Aida, M., Matsumoto, H., Higashio, N., Tokunaga, T., and Matsuoka, A. (2021). Signal and Noise Separation From Satellite Magnetic Field Data Through Independent Component Analysis: Prospect of Magnetic Measurements Without Boom and Noise Source Information. *Journal of Geophysical Research: Space Physics*, 126(5).

Jacobs, J. A., Kato, Y., Matsushita, S., and Troitskaya, V. A. (1964). Classification of geomagnetic micropulsations. *Journal of Geophysical Research (1896-1977)*, 69(1):180–181. _eprint: https://onlinelibrary.wiley.com/doi/pdf/10.1029/JZ069i001p00180.

Jo, W., Jin, H., Park, H., Jang, Y., Lee, S., Kim, K.-H., Garrick-Bethell, I., Shin, J., Baek, S.-M., Lee, J., Son, D., and Kim, E. (2023). Korea Pathfinder Lunar Orbiter Magnetometer Instrument and Initial Data Processing. *Journal of Astronomy and Space Sciences*, 40(4):199–215. Publisher: The Korean Space Science Society.

Johnson, C. L., Mittelholz, A., Langlais, B., Russell, C. T., Ansan, V., Banfield, D., Chi, P. J., Fillingim, M. O., Forget, F., Haviland, H. F., Golombek, M., Joy, S., Lognonné, P., Liu, X., Michaut, C., Pan, L., Quantin-Nataf, C., Spiga, A., Stanley, S., Thorne, S. N., Wieczorek, M. A., Yu, Y., Smrekar, S. E., and Banerdt, W. B. (2020). Crustal and time-varying magnetic fields at the InSight landing site on Mars. *Nature Geoscience*, 13(3):199–204. Number: 3 Publisher: Nature Publishing Group.

Jovanovic, N., Riwanto, B., Niemelä, P., Mughal, M. R., and Praks, J. (2021). Design of Magnetorquer-Based Attitude Control Subsystem for FORESAIL-1 Satellite. *IEEE Journal on Miniaturization for Air and Space Systems*, 2(4):220–235. Conference Name: IEEE Journal on Miniaturization for Air and Space Systems.

Judge, D. L., McLeod, M. G., and Sims, A. R. (1960). The Pioneer I, Explorer VI and Pioneer V High-Sensitivity Transistorized Search Coil Magnetometer. *IRE Transactions on Space Electronics and Telemetry*, SET-6(3/4):114–121. Conference Name: IRE Transactions on Space Electronics and Telemetry.

Kasper, J., Klein, K., Lichko, E., Huang, J., Chen, C., Badman, S., Bonnell, J., Whittlesey, P., Livi, R., Larson, D., Pulupa, M., Rahmati, A., Stansby, D., Korreck, K., Stevens, M., Case, A., Bale, S., Maksimovic, M., Moncuquet, M., Goetz, K., Halekas, J., Malaspina, D., Raouafi, N. E., Szabo, A., MacDowall, R., Velli, M., Dudok de Wit, T., and Zank, G. (2021). Parker Solar Probe Enters the Magnetically Dominated Solar Corona. *Physical Review Letters*, 127(25):255101. Publisher: American Physical Society.

Kepko, L., Clagett, C., Santos, L., Azimi, B., Berry, D., Bonalsky, T., Chai, D., Cudmore, A., Evans, A., Hesh, S., Jones, S., Marshall, J., Paschalidis, N., Rodriquez, J., Rodriquez, M., Sheikh, S., Starin, S., and Zesta, E. (2017). Dellingr: NASA Goddard Space Flight Center's First 6U Spacecraft. page 12.

Kilcommons, L. M., Redmon, R. J., and Knipp, D. J. (2017). A new DMSP magnetometer and auroral boundary data set and estimates of field-aligned currents in dynamic auroral boundary coordinates. *Journal of Geophysical Research: Space Physics*, 122(8):9068–9079. _eprint: https://onlinelibrary.wiley.com/doi/pdf/10.1002/2016JA023342.

Kivelson, M. G., Jia, X., Lee, K. A., Raymond, C. A., Khurana, K. K., Perley, M. O., Biersteker, J. B., Blacksberg, J., Caron, R., Cochrane, C. J., Dawson, O. R., Harris, C. D. K., Jones, J. E., Joy, S., Korth, H., Liu, J., Maghsoudi, E., Murphy, N., Parsley, D., Pierce, D. R., Racho, C., Richter, I., Russell, C. T., Sherman, S., Strangeway, R. J., Villarreal, M., Weiss, B. P., and Wigglesworth, L. (2023). The Europa Clipper Magnetometer. *Space Science Reviews*, 219(6):48.

Kivelson, M. G. and Russell, C. T. (1995). *Introduction to Space Physics*. Cambridge University Press. Google-Books-ID: qWHSqXGfsfQC.

Kominis, I. K., Kornack, T. W., Allred, J. C., and Romalis, M. V. (2003). A subfemtotesla multichannel atomic magnetometer. *Nature*, 422(6932):596–599. Number: 6932 Publisher: Nature Publishing Group.

Korde-Patel, A., Barry, R. K., and Mohsenin, T. (2022). Compressive Sensing Based Space Flight Instrument Constellation for Measuring Gravitational Microlensing Parallax. *Signals*, 3(3):559–576. Number: 3 Publisher: Multidisciplinary Digital Publishing Institute.

Lanzerotti, L. J. (2001). Space Weather Effects on Technologies. In *Space Weather*, pages 11–22. American Geophysical Union (AGU). _eprint: https://onlinelibrary.wiley.com/doi/pdf/10.1029/GM125p0011.

Lassakeur, A., Underwood, C., Taylor, B., and Duke, R. (2020). Magnetic Cleanliness Program on CubeSats and Nanosatellites for Improved Attitude Stability. *Journal of Aeronautics and Space Technologies*, 13(1):25–41. Number: 1.

Lee, J., Jin, H., Kim, K.-H., Park, H., Jo, W., Jang, Y., Kang, H., Kim, E., and Choi, Y.-J. (2023). Correction of Spacecraft Magnetic Field Noise: Initial Korean Pathfinder Lunar Orbiter MAGnetometer Observation in Solar Wind. *Sensors*, 23(23):9428. Number: 23 Publisher: Multidisciplinary Digital Publishing Institute.

Lenz, J. (1990). A review of magnetic sensors. *Proceedings of the IEEE*, 78(6):973–989. Conference Name: Proceedings of the IEEE.

Leuzinger, A. and Taylor, A. (2010). Magneto-inductive technology overview.

Le Contel, O., Leroy, P., Roux, A., Coillot, C., Alison, D., Bouabdellah, A., Mirioni, L., Meslier, L., Galic, A., Vassal, M. C., Torbert, R. B., Needell, J., Rau, D., Dors, I., Ergun, R. E., Westfall, J., Summers, D., Wallace, J., Magnes, W., Valavanoglou, A., Olsson, G., Chutter, M., Macri, J., Myers, S., Turco, S., Nolin, J., Bodet, D., Rowe, K., Tanguy, M., and de la Porte, B. (2016). The Search-Coil Magnetometer for MMS. *Space Science Reviews*, 199(1):257–282.

Lillis, R. J., Curry, S. M., Russell, C. T., Curtis, D., Taylor, E., Parker, J., Luhmann, J. G., Barjatya, A., Larson, D., Livi, R., Whittlesey, P., Ma, Y., Modolo, R., Harada, Y., Fowler, C. M., Xu, S., Brain, D. A., and Withers, P. (2020). ESCAPADE: COORDINATED MULTI-POINT OBSERVATIONS OF ION AND SPUTTERED ESCAPE FROM MARS.

Liu, Y., Dang, B., Li, Y., Lin, H., and Ma, H. (2016). Applications of Savitzky-Golay Filter for Seismic Random Noise Reduction. *Acta Geophysica*, 64(1):101–124.

Loto'aniu, T. M., Redmon, R. J., Califf, S., Singer, H. J., Rowland, W., Macintyre, S., Chastain, C., Dence, R., Bailey, R., Shoemaker, E., Rich, F. J., Chu, D., Early, D., Kronenwetter, J., and Todirita, M. (2019). The GOES-16 Spacecraft Science Magnetometer. *Space Science Reviews*, 215(4):32.

Ludlam, M., Angelopoulos, V., Taylor, E., Snare, R. C., Means, J. D., Ge, Y. S., Narvaez, P., Auster, H. U., Le Contel, O., Larson, D., and Moreau, T. (2009). The THEMIS Magnetic Cleanliness Program. In Burch, J. L. and Angelopoulos, V., editors, *The THEMIS Mission*, pages 171–184. Springer, New York, NY.

McInnes, L. and Healy, J. (2017). Accelerated hierarchical density based clustering. In *2017 IEEE International Conference on Data Mining Workshops (ICDMW)*, page 33–42. IEEE.

McMahon, P., Jung, H.-J., and Edwards, J. (2013). Swarm Deployable Boom Assembly (DBA) Development of a Deployable Magnetometer Boom for the Swarm Spacecraft. 718:13. Conference Name: 15th European Space Mechanisms and Tribology Symposium ADS Bibcode: 2013ESASP.718E..13M.

Merayo, J. M. G., Jørgensen, J. L., Friis-Christensen, E., Brauer, P., Primdahl, F., Jørgensen, P. S., Allin, T. H., and Denver, T. (2008). The Swarm Magnetometry Package. In Sandau, R., Röser, H.-P., and Valenzuela, A., editors, *Small Satellites for Earth Observation*, pages 143–151. Springer Netherlands, Dordrecht.

Milan, S. E., Provan, G., and Hubert, B. (2007). Magnetic flux transport in the Dungey cycle: A survey of dayside and nightside reconnection rates. *Journal of Geophysical Research: Space Physics*, 112(A1). _eprint: https://onlinelibrary.wiley.com/doi/pdf/10.1029/2006JA011642.

Miles, D. M. (2017). Advances in Fluxgate Magnetometry for Space Physics.

Miles, D. M., Dvorsky, R., Greene, K., Hansen, C. T., Narod, B. B., and Webb, M. D. (2022). Contributors to fluxgate magnetic noise in permalloy foils including a potential new copper alloy regime. *Geoscientific Instrumentation, Methods and Data Systems*, 11(1):111–126. Publisher: Copernicus GmbH.

Miles, D. M., Howarth, A. D., and Enno, G. A. (2019). In situ calibration of offsetting magnetometer feedback transients on the Cassiope spacecraft. *Geoscientific Instrumentation, Methods and Data Systems*, 8(2):187–195. Publisher: Copernicus GmbH.

Miles, D. M., Mann, I. R., Ciurzynski, M., Barona, D., Narod, B. B., Bennest, J. R., Pakhotin, I. P., Kale, A., Bruner, B., Nokes, C. D. A., Cupido, C., Haluza-DeLay, T., Elliott, D. G., and Milling, D. K. (2016). A miniature, low-power scientific fluxgate magnetometer: A stepping-stone to cube-satellite constellation missions. *Journal of Geophysical Research: Space Physics*, 121(12):11,839–11,860. _eprint: https://onlinelibrary.wiley.com/doi/pdf/10.1002/2016JA023147.

Moldwin, M. (2022). *An Introduction to Space Weather, 2nd Ed.* Cambridge University Press. Google-Books-ID: 1hOUEAAAQBAJ.

Moldwin, M. B., Wilcox, E., Zesta, E., and Bonalsky, T. M. (2022). Single-event effect testing of the PNI RM3100 magnetometer for space applications. *Geoscientific Instrumentation, Methods and Data Systems*, 11(1):219–222. Publisher: Copernicus GmbH.

Naik, G. and Kumar, D. (2009). Determining Number of Independent Sources in Undercomplete Mixture. *EURASIP J. Adv. Sig. Proc.*, 2009.

Ness, N. F., Behannon, K. W., Lepping, R. P., and Schatten, K. H. (1971). Use of two magnetometers for magnetic field measurements on a spacecraft. *Journal of Geophysical Research (1896-1977)*, 76(16):3564–3573. _eprint: https://agupubs.onlinelibrary.wiley.com/doi/pdf/10.1029/JA076i016p03564.

Nhalil, H., Givon, T., Das, P. T., Hasidim, N., Mor, V., Schultz, M., Amrusi, S., Klein, L., and Grosz, A. (2019). Planar Hall Effect Magnetometer With 5 pT Resolution. *IEEE Sensors Letters*, 3(12):1–4. Conference Name: IEEE Sensors Letters.

Nikolopoulos, C. D., Baklezos, A. T., and Capsalis, C. N. (2020). On Achieving Spacecraft Level Magnetic Cleanliness With Proper Equipment Ordinance of DC and ELF Magnetic Sources. *IEEE Transactions on Electromagnetic Compatibility*, 62(6):2714–2724. Conference Name: IEEE Transactions on Electromagnetic Compatibility.

Nishida, A. (1994). The Geotail Mission. *Geophysical Research Letters*, 21(25):2871–2873. _eprint: https://onlinelibrary.wiley.com/doi/pdf/10.1029/94GL01223.

Nuclear Weapon Archive (2003). Operation Plumbbob.

Ortner, M. and Coliado Bandeira, L. G. (2020). Magpylib: A free Python package for magnetic field computation. *SoftwareX*, 11:100466.

Park, H. H., Jin, H., Kim, T. Y., Kim, K. H., Lee, H. J., Shin, J. H., Jang, Y. H., and Jo, W. H. (2022). Analysis of the KPLO magnetic cleanliness for the KMAG instrument. *Advances in Space Research*, 69(2):1198–1204.

Parker, E. N. (1958). Dynamics of the interplanetary gas and magnetic fields. *Astrophysical Journal, vol. 128, p. 664*, 128:664.

Parry, H. (2022). Monitoring and Assessment of Geomagnetically Induced Currents in Alberta's High Voltage Network. *ERA*.

Pope, S. A., Zhang, T. L., Balikhin, M. A., Delva, M., Hvizdos, L., Kudela, K., and Dimmock, A. P. (2011). Exploring planetary magnetic environments using magnetically unclean spacecraft: a systems approach to VEX MAG data analysis. *Annales Geophysicae*, 29(4):639–647.

Pulkkinen, A., Bernabeu, E., Eichner, J., Beggan, C., and Thomson, A. W. P. (2012). Generation of 100-year geomagnetically induced current scenarios. *Space Weather*, 10(4). _eprint: https://onlinelibrary.wiley.com/doi/pdf/10.1029/2011SW000750.

Pulkkinen, T. (2007). Space Weather: Terrestrial Perspective. *Living Reviews in Solar Physics*, 4(1):1.

Rani, M., Dhok, S. B., and Deshmukh, R. B. (2018). A Systematic Review of Compressive Sensing: Concepts, Implementations and Applications. *IEEE Access*, 6:4875–4894. Conference Name: IEEE Access.

Ream, J. B., Weiss, B. P., Oran, R., Raymond, C. A., Polanskey, C. A., Wenkert, D. D., Elkins-Tanton, L. T., Hart, R. A., Russell, C. T., and Merayo, J. M. G. (2021). Magnetic gradiometry using frequency-domain filtering. *Measurement Science and Technology*, 33(1):015104. Publisher: IOP Publishing.

Regoli, L., Moldwin, M., Thoma, J., Pellioni, M., and Bronner, B. (2018a). Four-Magnetometer Board for CubeSat Applications. *Small Satellite Conference*.

Regoli, L. H., Moldwin, M. B., Pellioni, M., Bronner, B., Hite, K., Sheinker, A., and Ponder, B. M. (2018b). Investigation of a low-cost magneto-inductive magnetometer for space science applications. *Geoscientific Instrumentation, Methods and Data Systems*, 7(1):129–142. Publisher: Copernicus GmbH.

Regoli, L. H., Moldwin, M. B., Raines, C., Nordheim, T. A., Miller, C. A., Carts, M., and Pozzi, S. A. (2020). Radiation tolerance of the PNI RM3100 magnetometer for a Europa lander mission. *Geoscientific Instrumentation, Methods and Data Systems*, 9(2):499–507. Publisher: Copernicus GmbH.

Reju, V. G., Koh, S. N., and Soon, I. Y. (2009). An algorithm for mixing matrix estimation in instantaneous blind source separation. *Signal Processing*, 89(9):1762–1773.

Richardson, I. G. (2018). Solar wind stream interaction regions throughout the heliosphere. *Living Reviews in Solar Physics*, 15(1):1.

Ripka, P. (1992). Review of fluxgate sensors. *Sensors and Actuators A: Physical*, 33(3):129–141.

Roux, A., Le Contel, O., Coillot, C., Bouabdellah, A., de la Porte, B., Alison, D., Ruocco, S., and Vassal, M. C. (2008). The Search Coil Magnetometer for THEMIS. *Space Science Reviews*, 141(1):265–275.

Russell, C. T., editor (2004). *The Cassini-Huygens Mission: Orbiter In Situ Investigations Volume 2*. Springer Netherlands, Dordrecht.

Russell, C. T., Anderson, B. J., Baumjohann, W., Bromund, K. R., Dearborn, D., Fischer, D., Le, G., Leinweber, H. K., Leneman, D., Magnes, W., Means, J. D., Moldwin, M. B., Nakamura, R., Pierce, D., Plaschke, F., Rowe, K. M., Slavin, J. A., Strangeway, R. J., Torbert, R., Hagen, C., Jernej, I., Valavanoglou, A., and Richter, I. (2016). The Magnetospheric Multiscale Magnetometers. *Space Science Reviews*, 199(1):189–256.

Sandilya, M. and Nirmala, S. R. (2017). Compressed sensing trends in magnetic resonance imaging. *Engineering Science and Technology, an International Journal*, 20(4):1342–1352.

Schmid, M., Rath, D., and Diebold, U. (2022). Why and How Savitzky–Golay Filters Should Be Replaced. *ACS Measurement Science Au*, 2(2):185–196. Publisher: American Chemical Society.

Sheinker, A. and Moldwin, M. B. (2016). Adaptive interference cancelation using a pair of magnetometers. *IEEE Transactions on Aerospace and Electronic Systems*, 52(1):307–318. Conference Name: IEEE Transactions on Aerospace and Electronic Systems.

Shepherd, S. G. and Kress, B. T. (2007). Störmer theory applied to magnetic spacecraft shielding. *Space Weather*, 5(4). _eprint: https://onlinelibrary.wiley.com/doi/pdf/10.1029/2006SW000273.

Slavin, J. A., Le, G., Strangeway, R. J., Wang, Y., Boardsen, S. A., Moldwin, M. B., and Spence, H. E. (2008). Space Technology 5 multi-point measurements of near-Earth magnetic fields: Initial results. *Geophysical Research Letters*, 35(2). _eprint: https://onlinelibrary.wiley.com/doi/pdf/10.1029/2007GL031728.

Smith, C. W., L'Heureux, J., Ness, N. F., Acuña, M. H., Burlaga, L. F., and Scheifele, J. (1998). The Ace Magnetic Fields Experiment. In Russell, C. T., Mewaldt, R. A., and Von Rosenvinge, T. T., editors, *The Advanced Composition Explorer Mission*, pages 613–632. Springer Netherlands, Dordrecht.

Smith, E. J., Coleman, P. J., Judge, D. L., and Sonett, C. P. (1960). Characteristics of the extraterrestrial current system: Explorer VI and Pioneer V. *Journal of Geophysical Research (1896-1977)*, 65(6):1858–1861. _eprint: https://onlinelibrary.wiley.com/doi/pdf/10.1029/JZ065i006p01858.

Smith, E. J., Davis Jr., L., Coleman Jr., P. J., and Sonett, C. P. (1965). Magnetic measurements near Venus. *Journal of Geophysical Research (1896-1977)*, 70(7):1571–1586. _eprint: https://onlinelibrary.wiley.com/doi/pdf/10.1029/JZ070i007p01571.

Sonett, C. P. (1968). Multirate Sampling and Generalized Alias as a Source of Errors in Magnetometer Experiments. *IEEE Transactions on Geoscience Electronics*, 6(3):126–131. Conference Name: IEEE Transactions on Geoscience Electronics.

Spann, J., Swenson, C., Durao, O., Loures, L., Heelis, R., Bishop, R., Le, G., Abdu, M., Krause, L., Fry, C. G., Casas, J., Nash-Stevenson, S., Eberly, E., Denardini, C., Muralikrishana, P., Costa, J., Padua, M. d., Wrasse, C., Shibuya, L., and Mesmer, B. (2017). The Scintillation Prediction Observations Research Task (SPORT): An International Science Mission using a CubeSat. *Small Satellite Conference*.

Strabel, B. P., Regoli, L. H., Moldwin, M. B., Ojeda, L. V., Shi, Y., Thoma, J. D., Narrett, I. S., Bronner, B., and Pellioni, M. (2022). Quad-Mag board for CubeSat applications. *Geoscientific Instrumentation, Methods and Data Systems*, 11(2):375–388. Publisher: Copernicus GmbH.

Sun, J., Li, Y., Wen, J., and Yan, S. (2016). Novel mixing matrix estimation approach in underdetermined blind source separation. *Neurocomputing*, 173:623–632.

Torrence, C. and Compo, G. P. (1998). A Practical Guide to Wavelet Analysis. *Bulletin of the American Meteorological Society*, 79(1):61–78.

Tumanski, S. (2007). Induction coil sensors—a review. *Measurement Science and Technology*, 18(3):R31–R46.

Wallis, D. D., Miles, D. M., Narod, B. B., Bennest, J. R., Murphy, K. R., Mann, I. R., and Yau, A. W. (2015). The CASSIOPE/e-POP Magnetic Field Instrument (MGF). *Space Science Reviews*, 189(1):27–39.

Wang, H., Lühr, H., Ridley, A., Ritter, P., and Yu, Y. (2008). Storm time dynamics of auroral electrojets: CHAMP observation and the Space Weather Modeling Framework comparison. *Annales Geophysicae*, 26(3):555–570. Publisher: Copernicus GmbH.

Yao, H., Shearer, P. M., and Gerstoft, P. (2013). Compressive sensing of frequency-dependent seismic radiation from subduction zone megathrust ruptures. *Proceedings of the National Academy of Sciences*, 110(12):4512–4517. Publisher: Proceedings of the National Academy of Sciences.

Yu, M., Ma, W., Xin, J., and Osher, S. (2010). *Convexity and fast speech extraction by split bregman method*. Pages: 401.

Zonoobi, D. and Kassim, A. A. (2014). On ECG reconstruction using weighted-compressive sensing. *Healthcare Technology Letters*, 1(2):68–73.

Zou, S., Ren, J., Wang, Z., Sun, H., and Chen, Y. (2021). Impact of Storm-Enhanced Density (SED) on Ion Upflow Fluxes During Geomagnetic Storm. *Frontiers in Astronomy and Space Sciences*, 8.